uc3m | Universidad Carlos III de Madrid

TESIS DOCTORAL:

Modeling of Physical Processes in Radio-frequency Plasma Thrusters

Autor:
Bin Tian

Director:
Eduardo Ahedo Galilea

Co-director and Tutor:
Mario Merino Martinez

DEPARTAMENTO DE BIOINGENIERÍA E INGENIERÍA AEROESPACIAL

Leganés, Madrid, July 7, 2017

TESIS DOCTORAL

Modeling of Physical Processes in Radio-frequency Plasma Thrusters

Autor: Bin Tian

Director: Eduardo Ahedo Galilea
Co-director y Tutor: Mario Merino Martinez

Nombre y firma del Tribunal Calificador:

Presidente: _____

Vocal: _____

Secretario: _____

Calificación:

Leganés, de de 2017

Abstract

This Thesis presents an investigation of the plasma-wave interaction in Helicon Plasma Thrusters (HPT). The HPT is a new concept of electric space propulsion, which generates plasmas with RF heating and provides thrust by the electrodeless acceleration of plasmas in a magnetic nozzle. An in-depth and extensive literature review of the state of the art of the models and experiments of plasma-wave interaction in helicon plasma sources and thrusters is carried out. Then, a theoretical and numerical study of plasma-wave interaction is presented. Models for homogeneous (0D), radially inhomogeneous (1D) and axisymmetric (2D) plasma columns are derived and implemented into numerical codes. A parametric analysis of all the relevant design and operational variables in the HPT is performed with the 1D code, showing the influence of the plasma density, magnetic field strength, wave frequency, antenna shape and geometry of the problem. The 2D analysis focuses on the importance of plasma non-homogeneities and, in particular, the influence of the plasma plume expanding to the downstream of the source on the electromagnetic wave propagation and absorption. Results of this Thesis are expected to help guiding the design of future optimal HPT devices.

Resumen

Esta Tesis presenta una investigación sobre la interacción onda-plasma en motores de plasma de tipo helicón (HPT, por sus siglas en inglés). El HPT es un nuevo concepto de propulsión espacial eléctrica, que genera un plasma por calentamiento RF y proporciona empuje por acceleración sin electrodos en una tobera magnética. Se desarrolla en primer lugar un profundo y extenso análisis de la literatura existente con el estado del arte en modelado y experimentos sobre fuentes y motores helicón. Seguidamente, se presenta un estudio teórico y numérico de la interación onda-plasma. Se derivan la relación de dispersión 0D, un modelo radial 1D de ondas, y un modelo 2D de ondas, los cuales han sido implementados en sendos códigos numéricos. Se desarrolla un análisis paramétrico en todos las variables relevantes de diseño y operación con el código 1D, mostrando la influencia de la densidad del plasma, la intensidad del campo magnético, la frecuencia de la onda, la forma de la antena y la geometría del problema. El análisis 2D se centra en la importancia de las variaciones en las propiedades del plasma y, en particular, en el efecto que tiene la presencia de un chorro de plasma aguas abajo de la fuente en la propagación y absorción de la onda electromagnética. Se espera que los resultados de esta Tesis ayuden a guiar el diseño de futuros dispositivos HPT óptimos.

Acknowledgements

I would first like to express my sincere appreciation to my advisor, Professor Eduardo Ahedo, for providing me the opportunity to come to Spain and carry out my PhD Thesis in his group. I appreciate his great help since I knew very little about plasma physics and had no experience in electric propulsions when I started. He taught me from the very beginning with great patience. He is chariness and knowledgeable. I learn a lot in each discussion and guidance from him. I am very grateful for him to teach me to be a real researcher.

I also would like to deeply thank my co-advisor, Professor Mario Merino, who is intelligent and patient for directing me in the research. It is a great pleasure to work with him for always having wise advices and ideas. The enlightening discussions and suggestions he offered me have made the research more meaningful and fruitful. My sincere thanks go to him for numerous helpful suggestions and comments on the Thesis.

I am indebted to my colleague Jaume Navarro for the productive discussions on the plasma-wave problems and providing me the 1D plasma-wave interaction code as a direct support for my Thesis. I also appreciate Vitor Gomez from Sener for his contribution to the 2D plasma-wave interaction code.

My appreciation also goes to all the rest of members of the EP2 (Equipo de Propulsion Espacial por Plasmas) group. We share a pleasant working and learning environment to make the research and life colourful during my PhD. The useful arguments on the research improve us and help solving problems. I am deeply grateful to all my colleagues in the department of Bioengineering and Aerospace Engineering in UC3M. The Christmas dinner of the department is one of the happiest things in every year although it is always arranged in summer. It has been a pleasure for me to play football and watch football games with them.

Furthermore, my special thanks give to my Chinese friends in Spain. Their generous help and encouragement make me adapt to living abroad easily and quickly. We share useful information and enjoy delicious Chinese food even if we are not in China.

Last and foremost, I would like to express the most gratitude to my family, especially to my parents, for their unconditional support and never-ending love. Thanks to my mom for encouraging me to pursue my dream all the time. Thanks to my dad for reminding me to make efforts and never give up.

This Thesis was supported by the Spanish R&D National Plan (ESP2013-41052-P) and the scholarship from the Chinese Scholarship Council (CSC).

Contents

List of Figures

List of Tables

Chapter 1

Introduction

The meaning of propulsion originates from two Latin words: **pro** meaning before or forwards and **pellere** meaning to drive [1], describes driving an object movement by means of producing force. A space propulsion system is a device that produces thrust to push and accelerate a spacecraft. Unlike pushing objects on earth, the propulsion in space is no solid or fluid available and also nearly no friction. Therefore, the thrust can be produced most possibly by releasing part of mass from the spacecraft at a specific speed in terms of the Newton's third law of motion [1, 2]. This process can be described as a scalar form [3]

$$F = \dot{m} v_e \tag{1.1}$$

where F is the thrust, $\dot{m}$ is the mass flow of propellant and v_e is the effective exhaust velocity, which already takes into account any pressure contribution. The ratio of the thrust F to the mass flow rate $\dot{m}$ is known as the specific impulse I_{sp}, and constitutes an important figure of merit of the system, which denotes how well the propellant is used to produce thrust. A high value of I_{sp} allows completing a propulsive mission with a lower amount of propellant. Customarily, I_{sp} is defined in seconds, after dividing by the gravity acceleration at sea level g_0 [2],

$$I_{sp} = \frac{F}{\dot{m} g_0} \equiv \frac{v_e}{g_0} \tag{1.2}$$

The propulsive cost of any space mission can be expressed as the required increment of spacecraft velocity that the propulsion system must provide, Δv. This cost is related to the I_{sp} and the propellant mass M_p by the 'Rocket' equation [4]

$$\Delta v = I_{sp} g_0 \ln \left(\frac{M_p + M_f}{M_f} \right) \tag{1.3}$$

where M_f is the spacecraft mass at the completion of the acceleration period. The Eq. 1.3 shows that the increment of velocity Δv is proportional to the specific impulse and to the natural logarithm of the mass ratio. It implies that the total mass of spacecraft can be reduced by increasing the specific impulse I_{sp} for a given mission with a specified Δv and final delivered mass [4]. It can largely reduce the size and cost of spacecraft. Hence, the I_{sp} can be seen as the first figure of merit of a space engine [3].

Space propulsion systems can be broadly classified into chemical and electric propulsion systems. The first type applies a chemical reaction (usually combustion) to produce a hot, high pressure that expands in a nozzle to transform from the chemical energy to the kinetic energy [1]. Rocket launchers and hydrazine reaction control systems on board of spacecraft use this method. The second type employs electric power to accelerate the propellant by electrical and/or magnetic means. Fig. 1.1 shows the typical chemical and electric engines.

(a) Chemical engine (BE-4)

(b) Electric thruster (PPS-1350E)

FIGURE 1.1: The chemical engine and electric engine [5, 6].

To compare these two types of propulsion, the advantage of chemical propulsion is that a very large range of thrust levels from more than 1000 kN to less than 1 N can be achieved. However, the chemical propulsion systems store all their energy in the propellant chemical bonds, and has a fixed amount of energy per unit mass, which leads to the energy limitation for providing higher exhaust velocity or specific impulse [2]. To the contrary, the electric propulsion systems are not limited by the energy in the propellant but by the power installed in the spacecraft platform, such as solar panels or nuclear power [7]. Most of the existing electric propulsion technologies work by first ionizing the propellant into a plasma, and then applying electric and magnetic fields to accelerate it to much higher exhaust velocities than chemical one. Consequently, the I_{sp}

in electric propulsion system is typically much larger than chemical engines and much less propellant is required for a given mission [4].

Notwithstanding this, electric propulsion typically delivers a lower thrust levels in the order of μN to hundreds of mN. This results in new types of maneuvers known as low thrust, compared to the impulsive ones produced by chemical propulsion. Tab. 1.1 compares the typical chemical and electric propulsion engines.

	Chemical		Electric
	Small monopropellant thruster (RCS)	Fregat Main Engine (S5.92M)	SMART-1 Hall Effect Thruster (PPS-1350)
Propellant	Hydrazine	Nitrogen tetroxide / Unsymmetrical dimethyl hydrazine	Xenon
Specific Impulse(s)	200	320	1640
Thrust(N)	1	1.96×10^4	6.80×10^{-2}
Thrust time(h)	46	0.24	5000
Propellant consumed(kg)	52	5350	80
Total Impulse(Ns)	1.1×10^5	1.72×10^7	1.2×10^6

TABLE 1.1: Comparison of propulsion technologies [8].

1.1. Electric propulsion

Electric propulsion has been developed for nearly one century since the concept was proposed in the early 20th century [7]. It is now a mature and widely used technology on spacecraft. Numerous countries and researchers have made large contributions to it from the concept to the application in space. Many types of thrusters in this family such as ion thruster, hall effect thruster and resistojet has been applied in space missions [4]. New concepts of electric thruster are however being proposed or tested in the laboratory in the present, which promise improved performances over the existing ones.

The early history of electric propulsion up to 1950s has been introduced in details by Choueiri [9]. This concept was first supported to apply in space propulsion by Robert Goddard [10] in 1906 and the Russian scientist Tsiolkovskiy proposed similar concept independently in 1911 [9]. The Germany Hermann Oberth in 1929 and British Shepherd and Cleaver in 1949 also introduced the possibility of application of electric propulsion in space [4]. In addition, the first systematic introduction of electric propulsion was

proposed by Stuhlinger in 1950s [11]. After the 1950s, electric propulsion developed rapidly and several prototypes were tested and applied in space missions due to the rapid acceleration of space ambitions of the US and the USSR. The first experimental ion thrusters were launched into orbit in the early 1960s by the U.S [4]. The extensive applications of Hall effect thrusters were attributed to the efforts of Soviets. The first Hall effect thruster used in the Meteor satellite for station keeping was launched in 1971 [4]. Since then, more than 200 Hall effect thrusters have been utilized in all kinds of satellites and missions. The other type of electric thrusters are also widely used. With the development of technology, it can be predicted that the full electric propulsion in satellites would be the trends of future.

Due to the acceleration mechanism of thrust, the electric propulsion systems are typically classified into three categories: electrothermal, electrostatic and electromagnetic. Three groups are described in the following.

The Electrothermal propulsion is the method that the propellant is electrically heated in a chamber and then expanded through a suitable nozzle [7]. The typical representatives are the resistojet and the arcjet. A resistojet provides thrusts by heating non-reactive propellants via the chamber wall or heater coils. It can achieve the I_{sp} less than 500 s due to the limit of thermal heating of the propellant [4]. The first application of resistojet thrusters are installed on the military Vela satellites launched by the United States in 1965. However, the commercial applications were achieved in the INTELSAT-V program until 1980s [7]. Comparing with resistojets, the arcjet is the thruster which heats propellants by a high electric current arc. Tens or hundreds of currents are passed through the gas flow and higher temperatures of propellants are obtained than resistojets so that higher I_{sp} up to 700 s can be achieved. In 1993, hydrazine arcjets was first applied in the Telstar-4 series of GEO communication satellites [7]. Its good performance attracts more attention to become a viable option of propulsion.

The second group of electric propulsion family is the electrostatic propulsion. The most outstanding members in this group are the ion gridded thruster and its variants. A beam of ions is accelerated by a suitable electric field via biased grids and subsequently neutralized by a flux of free electrons [4, 7]. A very large specific impulse I_{sp} from 2000 s to over 10000 s and very high thruster efficiency from 60% to over 80% can be achieved by this thruster. Moreover, the lifetime can be up to 30000 hours. The typical disadvantage of ion thrusters are that it is more cumbersome than other EP devices and the grid erosion due to the particle impacting limits the performance. The first experimental tests for ion thrusters are very early in 1960s by the U.S and Soviets. However, it is rarely used in commercial application until 1990s. In 1995, the first operational use of

ion thrusters occured on the communications satellite ETS-6 for north–south station keeping [4].

Electromagnetic propulsion is the third group in the EP family. It generates the ion beam via the interaction of plasmas and applied or induced electromagnetic fields [7]. A major example in this class is the Hall effect thruster(HET). Unlike ion gridded thrusters, a cross-field discharge that results in an azimuthal electron current is used. The ion beam is accelarated under the electrostatic field impressed by the negative cathode. The electrons emitted by the cathode are used to ionize the neutral gas and neutralize the ion beam. Generally, the efficiency and specific impulse of Hall effect thruster are lower than ion thrusters achieved. The thrust efficiency is about $35\% - 60\%$ and the I_{sp} is in the range 1500–2000 s [4]. Another archetypal thruster in this group is the Pulsed plasma thruster (PPT). A pulsed discharge is utilized to ionize a fraction of solid propellant which generates the plasma arc. With the electromagnetic effects in the pulse, the plasma is accelerated. The normal efficiency and I_{sp} of PPT are $7\% - 13\%$ and 850-1200 s [4]. Due to the simple structure of PPT, in 1964 the first PPT application is achieved by the Soviets in Zond-2 spacecraft. After four years, four PPTs for east-west station keeping is used in LES-6 satellite by the United States. Other thruster concepts in this group are still being studied and tested in Lab and no practical application in space. The typical types are Magnetoplasmadynamic Thruster (MPDT), Electron Cyclotron Resonance Thruster (ECRT) and Helicon Plasma Thruster (HPT). The MPDT generates plasmas with very high electric current arc and plasmas are accelerated by the Lorenz force in the electromagnetic field [4, 12]. The capability of MPDT is the I_{sp} in the range of 1500-8000 s with thrust efficiencies exceeding 40%. The high efficiency (above 30%) requires very high power lever, larger than 100 kW [7]. Therefore, the MPDT tends to be regarded as a high power propulsion option in order to generate sufficient force for high specific impulse operation.

The ECRT and HPT are new concepts of EP thrusters. They are electrodeless, which means there is no anode or cathode in the thruster, so the erosion of electrodes is avoided and this improves lifetime. Because of the self-neutralization, the neutralizer for ECRT and HPT is not necessary. The Electron cyclotron resonance thruster, as its name implies, is ionized and heated gas by the electron cyclotron resonance which depends on the background magnetic field. The RF waves of the frequency in the microwave range (GHz) are emitted by the antenna and the quasineutral beam is accelerated by the magnetic nozzle. The Thrust efficiency of ECRT now is still low, less than 20% and the I_{sp} can reach to 1000 s [13]. Similarly, the HPT utilizes helicon waves in the MHz range to generate and heat plasmas and accelerate beams by the magnetic nozzle. The performance of the ECRT and HPT is currently lower than conventional thrusters, as

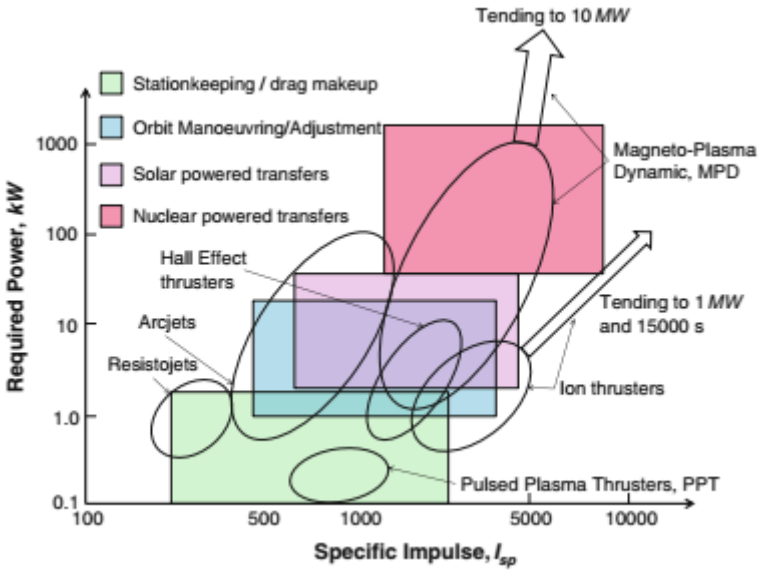

FIGURE 1.2: Approximate map of power and specific impulse available with different electric thrusters [1].

these systems are still under development. As the object of study of this Thesis, the HPT is discussed in more detail in next section.

To conclude this section, Fig. 1.2 shows the comparison of some main thrusters.

1.2. Helicon Plasma Thruster

The Helicon Plasma Thruster (HPT) is a new concept of electric propulsion, which generates thrust by electrodeless acceleration of plasma [14]. A HPT consists of a cylindrical (helicon) source, where the plasma is generated and heated by helicon waves, and a magnetic nozzle, where the plasma beam is accelerated supersonically [15]. Compared with best known types of thrusters, such as ion thrusters and Hall effect thrusters, this technology is expected to yield improvements on lifetime, simplicity of design, throttleability, capability of using different propellants, and compactness [3, 14, 16, 17].

Fig. 1.3 shows the main parts of the HPT. The helicon source system is made up of a dielectric cylindrical vessel, where the plasma is produced, an external RF antenna wrapped around the column and a set of external coils to produce the applied magnetic field [15]. The cylinder chamber is made of a dielectric material, such as quartz. A gas feed system is set up at one end of the chamber. The antenna emits electromagnetic radiation of frequency ω, of the order 1-100 MHz [18]. The plasma is confined radially by the applied axial magnetic field B_0, created by the external coils [15, 19]. In addition, An external divergent magnetic nozzle is formed by the external coils to accelerate the

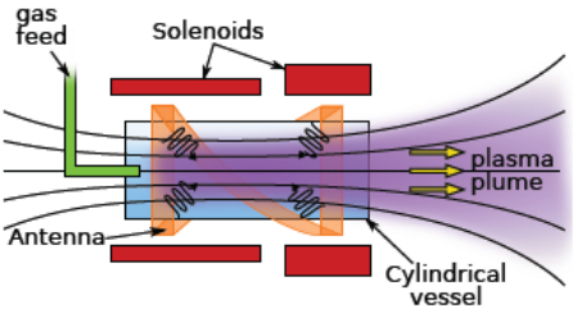

FIGURE 1.3: Sketch of the physical structure of a HPT

plasma beam outside of the source, in a similar fashion to the way a solid nozzle operates with a neutral gas [20].

Consequently, four physical processes dominate in the HPT. The plasma-wave interaction takes place inside the source leading to the deposition of wave energy into the plasma. Multiple transport phenomena govern the plasma dynamics there. Two other distinguished processes take place in the magnetic nozzle (MN): the supersonic plasma acceleration and its magnetic interaction with the thruster, and the detachment from the magnetic nozzle further downstream [21]. The four processes are coupled and influence each other. To understand theses four processes and the influence of each other is the main task to improve the performance of HPT.

Several prototypes of HPT have been developed by different groups in the world in order to understand the physical processes and improve performance. Here, three of the most prominent devices are introduced. A detailed review of existing prototypes and experiments with HPTs can be found in Navarro's PhD Thesis [22]. The first prototype is the Helicon Double Layer Thruster (HDLT), which is built by Charles and Boswell [23] in the Australian National University (ANU). In the test of this thruster, the power range 200-800 W is applied and the radio frequency is set to 13.56 MHz for double loop antenna. The magnetic field is in the range of 100-200 G. In these conditions, the maximum thrust can reach to 6 mN and the I_{sp} is 800 s [24]. However, the thrust efficiency is quite low, less than 3%. It may be due to the poor vacuum conditions far from the space condition.

The other HPT prototype named the mini Helicon Thruster Experiment (mHTX) was established and tested at the Space Propulsion Laboratory of MIT from 2005 to 2009 [25]. The experiments for mHTX use the power range 700–1100 W and the same frequency with HDLT for the half-turn helical antenna. The magnetic field 1500-1800 G is applied in the experiment, much higher than in the HDLT. It obtained maximum thrust up to 20 mN. The specific impulse for argon gas can reach to 2000 s and up to 4000 s for

nitrogen gas. The thrust efficiency is also higher than HDLT, 20% for argon and 18% for nitrogen [22, 25].

The third device selected as an example is the High Power Helicon Thruster (HPHT) built by Winglee group in the University of Washington [26]. To the contrary with HDLT and mHTX, this experiment uses very high powers, up to 20-50 kW, and low frequency near 0.5-1 MHz. The antenna is half helical and the magnetic field is about 150 G. Due to the high input power, the obtained thrust is quite high in the range of 1-2 N and the I_{sp} can be achieved in the range 2000-5000 s for different gases. The maximum reported thrust efficiency is about 50%. Notwithstanding this, independent confirmation of these figures is still needed.

1.3. Objectives and Thesis outline

The goal of this thesis is to further the understanding of the plasma-wave interaction in helicon plasma thrusters, which constitutes one of the key processes in the operation of these devices. This is first approached with an in-depth literature review of the start of the art, and second, with 0D, 1D and 2D models of the plasma-wave propagation in the frequency domain. The thesis investigates the influence of the relevant parameters on the wave propagation and power absorption through numerical simulation, integrating the models with the finite differences method. Several geometries are analyzed, from a simplified 1D helicon plasma source to a more relevant helicon thruster inside a vacuum chamber, including the plasma plume region.

Following these objectives, the structure of the rest of the Thesis is organized as follows.

Chapter 2 contains a literature review of the plasma-wave interaction in the HPT in past decades. The history, progress and current study in this area are critically discussed. The theoretical, experimental and numerical investigations in this problem are introduced in detail. This review constitutes a first element of guidance to understand the difficulties of the HPT plasma-wave interaction in the rest of the Thesis

Chapter 3 describes the general model of plasma-wave interaction in the HPT. From the general wave equations, the 0D dispersion relation of helicon waves, the 1D and 2D cylindrical plasma-wave model are derived in terms of appropriate assumptions.

Chapter 4 demonstrates the 1D cylindrical plasma-wave interaction model in detail and the corresponding computational code is developed. The truncation of azimuthal and axial modes in terms of Fourier transform is discussed in this part.

Chapter 5 contains the full parametric investigation of plasma-wave interaction for uniform plasmas in a HPT based on the 1D model derived in Chapter 4. It studies the influence of each parameter on the wave propagation and the power deposition in different frequency regimes. According to the variation of the plasma resistance, a general scaling law to guide the design of helicon source is proposed.

Chapter 6 describes the 2D plasma-wave interaction model and the numerical scheme of the 2D wave code in order to deal with the nonuniformity of plasma density and magnetic field. The wave propagation and power deposition in the near regime of plasma plume also include in the study. The quantitative analysis of power density and antenna impedance show the trends of power deposition.

Chapter 7 summarizes the main conclusion of this thesis and proposes the future lines of reseach.

Chapter 2

Plasma-wave Interaction in Helicon Sources: Literature Review

2.1. The early history

Helicon discharges have been known since the last decades to produce nearly fully ionized plasmas of over 10^{19} m^{-3} density with the appropriate power supply [27]. Due to this remarkable property, they have been used as plasma sources in diverse areas, from material processing to space propulsion [18]. The high efficiency of helicon sources is attributed to the distinctive characteristics of helicon waves. The first researcher using helicon waves to produce and maintain a plasma discharge was Boswell [28]. In 1970, Boswell made a small helicon discharge with a new type of antenna (named Boswell antenna) [29]. In the experiment, a very high plasma density up to 3×10^{19} m^{-3} was measured, showing a bright blue column in the center of the plasma [30].

Helicon waves are right-hand polarized waves that propagate in the presence of a magnetic field for wave frequencies between the ion and electron cyclotron frequencies, $\omega_{ci} < \omega < \omega_{ce}$ [18]. This special electromagnetic wave propagating in magnetized plasmas was first named 'helicon' in 1960 by Aigrain, who studied these waves in semiconductors [31]. The word describes the spiral nature of their waveforms due to the circular polarization, which means the the electric field rotates as the wave propagates along the magnetic field line tracing out a helix [18, 32]. The early theoretical studies on helicon waves in plasmas were due to Legendy [33, 34], Klozenberg et al [35] and Bleven [36–38]. The Klozenberg paper had the largest influence in the early stage because it derived the theory of plasma wave propagation in an insulated cylinder for a uniform

plasma profile [35]. In the experimental area, helicons were first observed in the atomic energy laboratory at Harwell, UK, by Lehane and Thonemann, who implemented an experiment to test the theoretical predictions of the Klozenberg paper [39]. The experiment was carried out in a glass tube of 10 cm diameter and 100 cm long. The background magnetic field B_0 was about 500 G, the pressure of xenon gas was $10-70$ mTorr, and a 3-kW RF generator was used, operating at about 15 MHz. This experiment confirmed the theory in Klozenberg paper and covered all important features of the waves, their dispersion, attenuation, and field structure [39].

After the 1970s, large number of studies and experiments on helicon waves have been carried out [18, 27]. The first extensive paper which describes the helicon wave propagation near the lower-hybrid frequency was written by Boswell [29] and the basic theory of the wave propagation in uniform and non-uniform plasmas was well developed by Chen [40, 41]. Then, the dispersion relation, antenna types, and the mechanisms of power absorption have been investigated extensively during the last two decades. Many researchers and groups in different countries have been engaged in this area to solve the open problems of helicon sources.

2.2. The dispersion relation

For a typical cylindrical RF discharge, the helicon wave coupling with the plasma needs to satisfy some conditions. The experimental results obtained by Degeling [42] and Ellingboe [43] in the large helicon source device WOMBAT show that the helicon plasma source can operate in three distinct modes: capacitive mode, inductive mode and helicon mode. The mode transition can be observed with increasing power or magnetic field, and a density jump occurs from one mode to another [43]. Therefore, it is necessary to establish the dispersion relation to describe the plasma-wave interaction in helicon sources.

Helicon waves are low frequency whistler waves confined to a cylinder with a coaxial magnetic field B_0. For the simplest case, the dispersion relation in a uniform bounded plasma has been derived by Chen [40]. Considering the wave is confined to a long cylinder of radius r_p, the linear relation for a specific mode is [18, 40]

$$\frac{3.83}{r_p} \approx \frac{\omega n_0 e \mu_0}{k_{\parallel} B_0} \propto \frac{\omega n_0}{k_{\parallel} B_0} \tag{2.1}$$

where n_0 is the plasma density, $k_{\parallel}$ is the parallel wavenumber, and e and μ_0 represent the electron charge and the magnetic permeability in vacuum, respectively. This relation shows that the magnetic field scales proportionally to the plasma density and frequency

for a given mode. Considering a finite cylinder, it also involves the length of the cylinder L in this linear relation because it is related to the parallel wavenumber $k_{\|}$ [44]. In addition, a similar dispersion relation was obtained by Boswell using the generalized Ohm's law in unbounded plasmas [45]. The right-hand polarized waves propagate in different regimes in general, giving rise to Compressional Alfven waves ($\omega < \omega_{ci}$), Helicon waves ($\omega_{ci} \ll \omega \ll \omega_{ce}$) and Electron-Cyclotron Waves ($\omega \sim \omega_{ce}$) [45].

The linear relation of Eq. 2.1 is obtained in a simple situation, with the non-uniformity of plasma density, the electron inertia and ion motion not taken into account [40]. However, this linear relation, especially the magnetic field proportionality to the plasma density, has been proved correct in more complex arrangements. The linear relationship between n and B_0 at high magnetic fields has been proved in experiments in 1992 [46]. At low magnetic fields, the plasma density scaling does not vary monotonically with B_0. Instead a density peak at low field of the order 50G has been observed. This phenomenon attracted the attention of many researchers. A number of authors investigated it experimentally and numerically [47–51]. In the recent experiments by Lafleur [51], it was found that the peak density still follows the linear relationship with magnetic fields for different conditions of RF power ($50\,\mathrm{W} < P_0 < 400\,\mathrm{W}$) and gas pressures ($0.04\,\mathrm{Pa} < p_0 < 0.4\,\mathrm{Pa}$). Also, the linear dependence of plasma density on the magnetic field is both experimentally and numerically found to be valid when the applied magnetic field is near but lower than the magnetic field corresponding to the lower hybrid frequency [52–54].

In addition, that linear relation is satisfied by the plasma resistance in uniform plasmas [55]. The contour plots of the plasma resistance versus the magnetic field and plasma density from numerical simulations show the linear dependence clearly [55–57]. And the evidence in experiments was also obtained by Lafleur [51]. The measurements within the matching network/antenna device show local peaks of the plasma resistance, satisfying the linear relation between n and B_0. The local peaks of resistance are well consistent with the observed density peaks, indicating the high efficiency of power transfer between the antenna and plasma.

2.2.1. The Trivelpiece-Gould mode

As we mentioned in the previous section, the electron inertia is neglected in the dispersion relation when $\omega \ll \omega_{ce}$. For frequencies as low as $0.1\omega_{ce}$, the electron inertia has to be taken into account [58] i.e. the electron mass is taken as nonzero. Therefore, a second branch of waves is excited along with the helicon branch. It is an electrostatic wave highly damped in a narrow layer near the plasma boundary [18, 59]. Klozenberg [35]

and Boswell [60] first predicted that this wave would exist in helicon plasmas and it is now called the Trivelpiece-Gould (TG) mode [61].

The dispersion relation and the characteristics of TG modes have been investigated theoretically and experimentally [18]. A biquadratic equation for the wavenumber considering the electron mass has been obtained to describe the dispersion relation of helicon plasmas [58, 62, 63]. The two pairs of solutions of this equation represent the two branches of waves, helicon mode and TG mode [62]. The TG mode has a larger perpendicular wavenumber $k_\perp$ than the helicon mode and hence shorter wavelength. In addition, it is stated that the TG mode only can be excited in bounded plasmas, although whistlers can propagate in unbounded plasmas [58]. That is because the helicon mode and TG mode are considered as eigenmodes of a plasma column caused by the boundary condition.

The characteristics of TG modes have been treated theoretically in detail by Shamrai and Taranov [55, 62, 64, 65]. Three wave propagation regimes to waves), the HELICON LAND (helicon mode and TG mode, coupled together) and the TG-LAND (opaque to helicon mode) [62]. To analyze a simple energy transfer model, it is concluded that the TG mode is the main channel of energy absorption [62, 66]. That is because the TG mode keeps almost all the energy in the electron motion and so it is strongly absorbed via collisions [66]. In addition, the concepts of resonance and anti-resonance are used in the wave propagation by Shamrai [64]. It is considered to be an intrinsic property for a bounded plasma. It explains how the waves influence the power deposition and lead to the oscillation of the plasma resistance, when varied with the magnetic field or plasma density [66]. Furthermore, the mode conversion between the helicon mode and TG mode is found to be an important power absorption mechanism to explain the high efficiency of the helicon discharge [65].

The study of Borg [58] reveals that the antenna-wave coupling cannot be improved significantly by the finite electron mass effects when $\omega/\omega_{ce} < 0.5$ and the cavity resonance of the TG mode could be difficult to excite in experiments. In the previous part, the linear relation based on a simple model has been discussed. It is mentioned that the linear relation is satisfied in practice even if the electron inertia is not taken into account. Computations by Chen [63] show that the radial profile of the helicon mode is not affected by the presence of the TG mode since this is highly damped in the bulk region of plasmas and its rapid radial variations is difficult to detect. Therefore, measurements of the wave fields away from the surface is expected to reveal the helicon mode. This may explain why the early theory can predict the helicon wave with small errors [63].

As we said, the experimental investigation of TG mode is difficult. The TG mode has not been measured directly because this mode tends to be localized in a very narrow

layer near the plasma boundary. Hence, large efforts have been made to find it in the laboratory. Blackwell et al. [67] provide evidence of the existence of TG mode via measuring the current density $J(r)$ in the plasma. Analyzing the wave equations, it is found that the current density is more sensitive to the TG mode. Hence, the TG mode can be verified by measuring the variation of current density. The radial profile of $J(r)$ is measured by the B-dot probe in experiments and the 'TG wing' near the boundary has been detected, thus proving the existence of the TG mode [67]. Another experimental studies of TG modes were carried out by Shinohara [68]. They give evidence that the TG waves generated by the mode conversion of helicon waves in a highly collisional plasma induces a strong plasma current near the plasma edge and the skin effect arises due to strongly damped TG modes.

2.2.2. Non-uniform plasma density

The non-uniformity of plasma density in helicon discharges is a central aspect that influences the wave propagation and power deposition [41]. In the early stages, the first experiment on helicon waves by Lehane and Thonemann [39] recognized that the non-uniformity may be the reason to cause the difference between the early theory and experimental results. Blevin and Christiansen [36, 38] treated it briefly theoretically. The dispersion relation for non-uniform plasmas was discussed [36]. In the 1990s, Chen and his colleagues [41, 69, 70] investigated this problem in more detail. The numerical results showed that there is a marked difference between $m = +1$ and $m = -1$ azimuthal modes in a non-uniform plasma due to a difference in sign of the electron drift along the density gradient [41]. The radial inhomogeneity of the plasma density results in the suppression of the $m = -1$ mode [71, 72]. The density radial profiles varying from constant to near-Gaussian were studied to examine the influence on the wave propagation. A steady progression of increasing and narrowing of the short axial wavelength peak and reduction of the long wavelength peak was found for different $n(r)$ [70]. Considering the effect of the TG mode for the high field, non-uniform plasmas show that TG waves dominate the power absorption [56, 70].

Another exploration of non-uniformity of plasma density in helicon discharges led to a new type of excited mode. Breizman and Arefiev [73] developed the theoretical analysis of helicon waves for inhomogeneous plasmas and discovered the radially localized helicon waves (RLH) propagating in helicon plasmas due to the plasma gradient. In a plasma column, the potential well formed due to the radial density gradient and allowed radially localized solutions in low frequency ranges. Hence, it caused the RLH excited mode. The theoretical and experimental evidences of RLH mode were presented by Guangye et al [74]. It confirmed that the RLH waves can play a major role in helicon plasma

sources. The power deposition of RLH modes gives a larger contribution than TG mode [74]. In addition, Lee [75] and Chang [76] also give the evidence of the existence of RLH modes. Moreover, they found that the ion-accoustic-instability may be the reason to explain that only using larger collision frequency in numerical simulations, these agree well with experimental results [75, 76].

2.2.3. The lower hybrid frequency range

The helicon wave propagating near the lower hybrid frequency in plasmas has been much studied since the 1970s [77, 78]. It plays an important role in space plasmas and fusion research due to the close relation to the ion heating and the lower-hybrid drift instability [79]. In the 1980s, the investigation of the influence of the lower hybrid frequency in helicon plasmas was studied by Boswell and Zhu [29, 80]. They found that a very dense plasma can be produced near the lower hybrid frequency with helicon waves. After that, the extensive studies on the lower hybrid frequency was carried out by many researchers [52, 81–83].

The lower hybrid frequency ω_{lh} is a resonant frequency between the electron cyclotron frequency ω_{ce} and the ion cyclotron frequency ω_{ci} and has the form of [61]

$$\omega_{lh} = \left[\frac{1}{\omega_{ci}\omega_{ce}} + \frac{1}{\omega_{pi}^2 + \omega_{ci}^2}\right]^{-1/2} \approx \sqrt{\omega_{ci}\omega_{ce}} \tag{2.2}$$

where ω_{pi} represents the ion plasma frequency. Near the lower hybrid frequency, the effect of ion motion cannot be neglected. The general dispersion relation shows that the wavenumber become infinite when the frequency is near ω_{lh} and the resonance occurs [53]. It is expected to be beneficial for the power deposition. The experimental results confirmed this prediction. The experiments by Yun [52, 84] tested the frequency dependence of helicon plasmas for different magnetic fields and various gases. It is shown that the optimum frequency yielding the highest plasma density is near the lower hybrid frequency and it suggested that the lower hybrid resonance heating may be important in helicon sources [52]. However, the optimum frequency is not exactly equal to ω_{lh} but slightly lower. It may be explained by the Doppler shift effect [52].

In order to study the role of the lower hybrid frequency in helicon discharges, Cho investigated the dispersion relation in detail and gave the self-consistent results coupling the wave equations to the global balance equations [53]. He found that there are many eigenmodes when the operation frequency is higher than ω_{lh}, but there are a few isolated eigenmodes for frequencies lower than ω_{lh}. Furthermore, there is always an eigenmode near the lower hybrid frequency. This behavior leads to the variation of the resistance

with the frequency. Specifically, the resistance usually has a large peak near the lower hybrid frequency depending on the plasma density [53]. The self-consistent results show that the abrupt density jump occurs near the lower hybrid frequency. In addition, it is confirmed that the linear relation between the density and the magnetic field is valid when $\omega > \omega_{lh}$. This rule is not valid for $\omega < \omega_{lh}$ probably due to the sharp decrease of the resistance in this region. These conclusions are also confirmed in the experiments by Kwak et al [54].

Additional experimental results obtained by Balkey [82] indicate that the maximum electron density is measured when the rf frequency is near the lower hybrid frequency. It is consistent with the previous results by others. However, the maximum ion temperature is measured when $\omega < 0.7\omega_{lh}$. It is suggested that the mechanism of power deposition for ions and electrons in helicon sources is distinct. It is not necessary for helicon sources to maximize the electron density and the ion temperature simultaneously [82]. And when studying very light ion mass gases such as hydrogen, Mori found that the optimal frequency can be away from ω_{lh} in a non-uniform magnetic field as long as the RF power is large enough [83].

2.3. The power absorption mechanisms

The mechanisms of power deposition has been considered as a huge challenge in understanding helicon plasmas by all the researchers. They have been discussed for many years since the high efficient ionization of helicon discharge was discovered and it is still not clear in the present. The mechanism of wave dissipation mainly has two channels including the collisional damping (particle-particle interaction) and non-collisional damping (wave-particle interaction) [66]. Both these two damping ways can be linear or nonlinear. The collisional damping was expected to mainly heat electrons. However, the experiments by Boswell [29] in 1984 indicated that the collisional damping was too weak to explain the overall power deposition in the helicon source. The applied collision frequency should be 1000 times larger than the Coulomb collision frequency in order to get the consistency between the calculated wave field and the experimental results [29]. Therefore, the Landau damping as the wave-particle interaction channel was proposed to explain this phenomenon by Chen [40]. He established the theoretical model to demonstrate that the Landau damping could play an important role in the power deposition of helicon plasmas. It was considered to increase the effective collision frequency because the Landau damping could heat the tail of the electron population where the electron thermal velocity was close to the phase velocity of the helicon wave. This hypothesis was accepted by numerous authors [85, 86] and was supported by the experiments of

Ellingboe et al [87] which measured the fast electrons. However, the phase velocity of helicon waves varied in a wide range of magnitudes in different size of helicon sources. Hence, it is difficult for the Landau damping to be an universal mechanism of power deposition [66]. Then, experiments using a gridded energy analyzer have been carried out by Chen and Blackwell [88]. They found that Landau-accelerated electrons are too sparse to explain the high ionization efficiency and they concluded that the hypothesis of Landau damping as the main mechanism of power deposition was incorrect [88]. In addition, the antenna loading and plasma ionization was found to be the evidence for the mechanism of TG mode coupling near the plasma boundary.

Although the hypothesis of Landau damping has now been rejected by Chen, the influence of wave-particle interaction on the power deposition cannot be fully ruled out. The nonlinear mechanism called wave-particle trapping was proposed by Ellingboe and Boswell [87]. The experimental results implied that the electrons would be trapped in the longitudinal electric field provided that the electrons move in synchronism with an intense helicon wave [87]. Thus, the wave energy is transferred to the electrons and leads to the high ionization [66]. A further study on the wave-particle trapping was carried out by Degeling et al [42]. A simple model was established to estimate the electron thermal velocity which is most likely to ionize in a Maxwellian distribution. It is found that this estimated electron velocity is consistent with the helicon wave phase velocity measured in the experiments [42]. This strong correlation suggests that electrons are trapped by the helicon wave when the thermal velocity in the Maxwellian distribution are slightly smaller than the wave phase velocity and then accelerated by the helicon wave to join in the population with the velocity slightly faster than the wave [42]. However, this simple model was not complete. The applied magnetic field was not taken into account and only the longitudinal component of electric field E_z was considered in the model.

Therefore, the above mechanisms of wave damping are still not convincing as the reason of high efficiency of helicon sources. With the discussion of the second branch of Waves called the TG mode, the mechanism of mode conversion of helicon mode to the TG mode was considered as the main mechanism of plasma wave interaction by Shamrai [65, 66]. As it was mentioned in the previous section, the TG wave has very short wavelength. It was strongly localized near the plasma edge and rapidly damped in the bulk region [55]. To the contrary, the helicon mode has long wavelength and is weakly damped in plasmas. Consequently, the conversion of helicon wave power to TG power is thought to occur [62]. According to the theory by Shamrai, the surface mode conversion is the most universal mechanism for rf power absorption. It arises near the plasma edge with the insulating wall and can be valid at any magnetic field [65]. The bulk mode conversion occurs in the bulk plasma when the wavelengths of helicon and TG waves are close in magnitude. The absorption due to this conversion is high only at low magnetic field,

because the required plasma density is too high to obtain it in the high magnetic field range [65]. Although the theory of mode conversion has been developed completely by Shamrai, it is difficult to confirm it in the laboratory, because the TG mode is not easy to detect in the experiments and only can be measured indirectly [67]. Another proposal such as the radially localized helicon wave (RLH) due to the gradient of plasma density is given by Breizman and Guangye [73, 74], as already mentioned. They found that the RLH dominates the contribution of power deposition in their experimental and numerical results [74].

In summary, the above studies of the mechanisms of power deposition in helicon sources explain some partial phenomena or situations happening in practice. However, the general principle of power deposition and plasma-wave interaction is still not confirmed. It need more developments in theory and in the technology of experiments in the future.

2.4. Antenna types

The antenna which is used to provide the rf power for ionizing and heating plasmas plays a significant role in helicon discharges [89]. The different antenna types in helicon discharges have been much discussed theoretically [66, 70, 89] and experimentally [46, 90]. In order to improve the efficiency of the helicon discharge, the principle of plasma-wave coupling for different antenna types and the optimization of antenna design are main issues for researchers [89]. The most commonly used antenna types in the helicon plasma system include the Nagoya III antenna [46, 52], the double saddle coil [29], the helical antenna [90, 91] and the single loop antenna [92, 93].

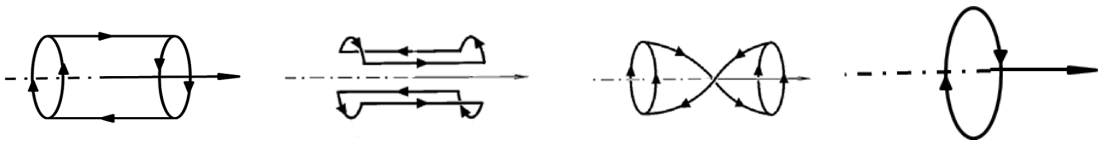

(a) Nagoya III (b) Double saddle (c) Half-turn helical (d) $m = 0$ loop

FIGURE 2.1: Different types of antennas [70, 89, 94].

The Nagoya III antenna shown in Fig. 2.1(a) is especially effective in the plasma-wave interaction. It consists of two circular loops on either side connected by straight wires. Due to this sturcture, it was found to excite large rf fields in the plasma by Watari [95] in 1978, which studied the rf plugging of mirror machines [18]. The large field induced by Nagoya III antenna in the plasma- wave coupling has been explained by Chen [46]. It is due to the amplification of the rf field when creating the electrostatic fields by Nagoya III antenna [46].

The double saddle coil antenna in Fig. 2.1(b), also called Boswell antenna, is a modified Nagoya III antenna [46]. The circle loop in each side is split into two semicircles. It was first used by Boswell [29] in helicon plasmas to produce dense plasmas. The advantage of this antenna is that the antenna can be easily split around a cylindrical discharge tube without breaking the vacuum [18].

The helical antenna shown in Fig. 2.1(c) is another modified Nagoya III antenna and was first proposed by Shoji [91, 96]. Here the straight wires of the Nagoya III antenna are twisted into helices. Because of the direction of the helix, the right-hand and left-hand helical antenna are defined naturally. The helical antenna is attractive because it is directional. The wave energy propagates mainly in one direction along the magnetic field [89].

The $m = 0$ loop antenna in Fig. 2.1(d) is a simple loop structure. It is an azimuthally symmetric antenna and only the $m = 0$ mode can be excited in practice. On the contrary, all mentioned antennas above are azimuthally anti-symmetric, and so they excite the waves with odd azimuthal numbers, primarily the $m = \pm 1$ modes [66].

Each type of antenna has been investigated experimentally and numerically. It is concluded that for all anti-symmetric antennas the $m = +1$ mode is better preferred than the $m = -1$ mode [90, 97]. And it suggests that the $m = +1$ mode has greater contribution to the power absorption in helicon plasmas [98]. This conclusion is confirmed by numerical studies [70, 89]. The $m = +1$ mode provides larger resistance than other modes in most non-uniform density cases. And for helical antennas, the right-hand helical antenna is more effective than the left-hand one and can obtain higher plasma densities [90]. The reason is not clear yet [18]. Moreover, the half-wavelength antenna being better than a full-wavelength antenna in experiments opposes the expectation of researchers [99]. This is also still not well understood.

In addition, the parametric investigation and comparison has been discussed in detail [70, 89, 94, 100, 101]. The antenna impedance, especially the real part or resistance, is considered as the main parameter to evaluate the antenna performance [89]. To summarize the conclusions, the general agreements for these four antenna types are that the $m = 0$ loop antenna has quite different behaviors [66, 101] and much poorer performances [89, 94] than others. The rest three types are comparable and depend on specific situations [89] although more evidence is provided to support helical antennas. In summary, the parametric analysis and the understanding of the operation of helicon plasma sources is, at present, still incomplete. In order to obtain the precise conclusion, the fully parametric investigation is necessary to carry out and discuss the relation among them. This is one of the objectives of the present Thesis.

2.5. Simulation tools

Simulation tools based on the plasma-wave interaction model in helicon plasmas have been widely developed by numerous authors [18]. Most efforts approach the problem by solving Maxwell wave equations with the (linear) plasma dielectric tensor and suitable boundary conditions. The Fourier transform both in time and space can be applied to simplify the wave equations. In helicon plasmas, the Fourier transform in time is commonly used. Hence, all quantities in the plasma are converted to time harmonics as $\sim \exp(i\omega t)$ [102]. Application of the Fourier transform in space depends on the dimensionality of the spatial configuration. Both 1D and 2D plasma-wave models are used in the studies. In addition, the different forms of Fourier expansion are considered for finite or infinite cylinder geometry [103].

In the early stage of this field, a simple plasma-wave model was introduced by Klozenberg [35] using the basic dispersion relation of cylindrically uniform plasmas. It has been checked to have a good agreement with experimental results in specific situations [39]. Then, Boswell [29] and Chen [40] further developed that theory. The helicon wave propagating in uniformly bounded plasmas was considered and the wave pattern of a single mode was described in more detail by Chen [40]. However, these early theories are incomplete and insufficient to analyze the problem precisely. The electron inertia, the plasma non-uniformity and the ion motion were not taken into account [40].

The 1D radial plasma-wave model in finite cylindrical helicon sources for uniform plasmas was introduced by Fischer et al [104] and Shamrai et al [55]. The ideal conducting boundary condition was considered and yields the wave eigenmodes [55]. Then, an analytical solution can be obtained for uniform plasma density and magnetic fields. This model considers the effect of electron mass so the TG mode is included. Furthermore, the ion motion can be included in the model by adding the ion component in dielectric tensor. Then, Cho also worked with that model [59] and improved it with a numerical integration method to deal with the radially non-uniform density profile [71, 105]. A similar code named HELIC has been implemented by Arnush and Chen [18, 70]. In early years, this code was used to deal with the infinite cylinder case. Then HELIC was improved to be more fuctional (and a friendly user interface) [18]. It can be applied to radially uniform or nonuniform cases for any cylinder length. Besides that, a simulation code, which was an advanced version of the original ANTENA code [106], was introduced by Mouzouris and Scharer [94]. They found that the electron heating was strongly influenced by the density profiles [94]. Melazzi et al [107] developed a new 1D electromagnetic solver SPIREs using the finite difference method. It has high efficiency and accuracy, demonstrated through numerous tests.

All 1D codes we mentioned above are based on a vital assumption, the 'zero- thickness antenna approximation' [107]. It assumes that the antenna wire is very thin and thus the thickness of antenna wire can be neglected. This assumption, very widely used, introduces singular lines inside the physical domain, so it is only beneficial in certain configurations, as we will see in the Thesis. An important issue we will find of the zero-thickness antenna is that some components of the wave fields are divergent in the location of the antenna and the antenna reactance cannot be obtained correctly [66, 108]. In order to solve this problem, some approaches were proposed. A 1D plasma kinetic code named UFEM, which used the finite element discretization of RF fields, was developed by Kamenski and Borg [103]. The thickness of antenna is considered in this code although the radial component of current density is still imposed rather than computed. It provides a reasonable antenna reactance. Another Code ADAMANT proposed by Melazzi and Lancellotti [109] introduces a full-wave approach which is based on a system of coupled surface (SIE) and volume integral equations (VIE) for the computation of the current distribution on the antenna conductors. Therefore, the exact current density and reactance of antenna can be obtained [101, 109].

In 1D plasma-wave model, only radial non-uniformities can be taken into account. However, the axial effects are very important and strongly influence the helicon discharge. Hence, developing more general models became necessary. The 2D plasma-wave model has been considered by several researchers. Takechi and Shinohara [110] presented the results on the study of 2D convergent and divergent magnetic fields in helicon plasmas with using the Transport Analyzing System for tokamaK/Wave analysis (TASK/WA) code developed by Fukuyama. The 2D non-uniformity including density and magnetic fields was taken into account in this code. The computational results were compared with the experimental data and obtained the consistency. Mouzouris and Scharer [111] developed a 2D wave code MAXEB which includes not only the collisional damping but Landau damping to simulate the inhomogeneous plasmas. Both uniform and non-uniform plasma density and magnetic field can be treated in this code. It is found that the collisional damping is the dominant heating mechanism for moderate pressures ($p > 2$ mTorr) and higher densities ($n_e > 2 \times 10^{18}$ m^{-3}) [111]. In comparison, the Landau damping becomes important at low pressure ($p < 2$ mTorr) and heats the electrons mainly at the surface where the resonant electrons have velocities near the wave phase velocity [111]. Kinder and Kushner [112, 113] developed a two-dimensional Hybrid plasma Equiqment Model (HPEM) to study the power absorption and plasma transport in helicon sources. The Electromagnetics module in this self-consistent model can deal with the 2D applied magnetic fields. However, this model mainly focus on the pure helicon mode and neglect the influence of TG mode [114]. They involve the influence of TG mode in a later paper [112]. The electrostatic term is only approximated by a damping

factor. Similarly, the other self-consistent model which can deal with 2D non-uniform properties and involve the influence of TG mode are introduced by Bose et al [115]. It is concluded that the propagation of waves is enhanced in the downstream with increasing the electromagnet coil current ratio (CCR) and this is accompanied by a increase of power absorption in the downstream. In addition, Guangye et al [74] have implemented another 2D plasma-wave code using finite difference discretization. Four staggered grids from Yee' s scheme [116] are applied to discretize the EM field. This code has a good agreement with experimental results and has been used to study the radially localized helicon wave (RLH) [74–76].

2.6. Typical experimental devices

Helicon discharges have been developed for several decades and a number of helicon sources were established by numerous groups and researchers. An in-depth review of helicon source and helicon thruster experiments was recently presented in Navarro's PhD Thesis [22]. Next, some relevant experimental devices for helicon plasmas are introduced briefly.

As the earliest group of studying helicon discharges, the Plasma Research Laboratory of the Australia National University, led by Boswell, has established some typical helicon plasma devices. The **BASIL** machine is the one built in the early stage [117]. It is 4.5 cm in diameter and 160 cm long. The external magnetic field can be up to 1600 G and RF power up to 5 kW at 7 MHz [18]. Then, the vacuum chamber called **WOMBAT** was built to study the helicon plasma [29]. This large chamber is 90 cm in diameter and 200 cm long. It can be used to test not only helicon sources but also space thrusters. The third machine **MAGPIE** shown in Fig. 2.2 is a linear plasma-material interaction machine, which was designed for studying basic plasma phenomena [76].

In UCLA (University of California, Los Angeles), Chen and his colleagues developed different sizes of helicon sources. A linear device with 5cm diameter and 170cm length was the first helicon device in UCLA [18]. The early experiments of Chen's group were carried out in this machine [119]. Then, a larger device with 10 cm diameter and 108 cm long was built by Blackwell [120]. The evidence of the existence of the TG mode was obtained in this large device [67].

In West Virginia University, the interesting results are mostly obtained in a machine called **HELIX**. It consists of a Pyrex tube as a helicon source with 157 cm long and 10 cm diameter, a small metal chamber with 15 cm diameter and a large chamber as expansion region, with 450 cm length and 200 cm as inner diameter. In the experiments

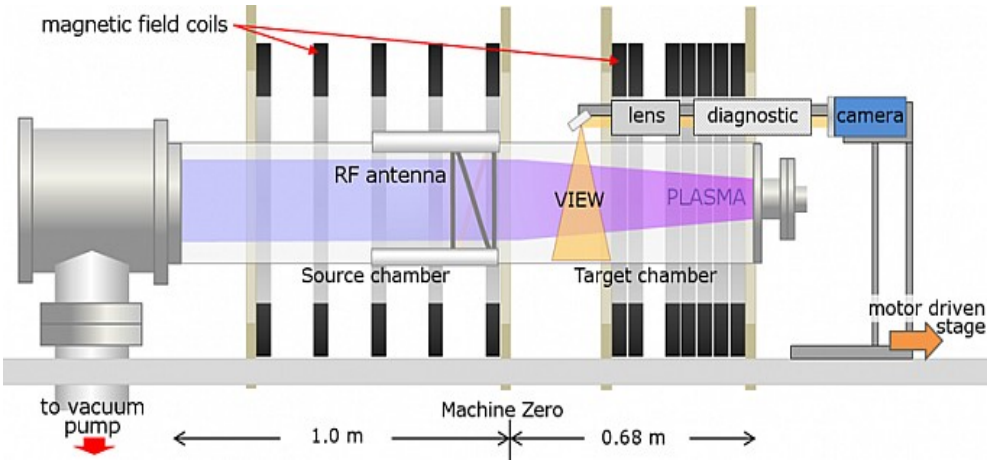

FIGURE 2.2: The schematic of MAGPIE [118].

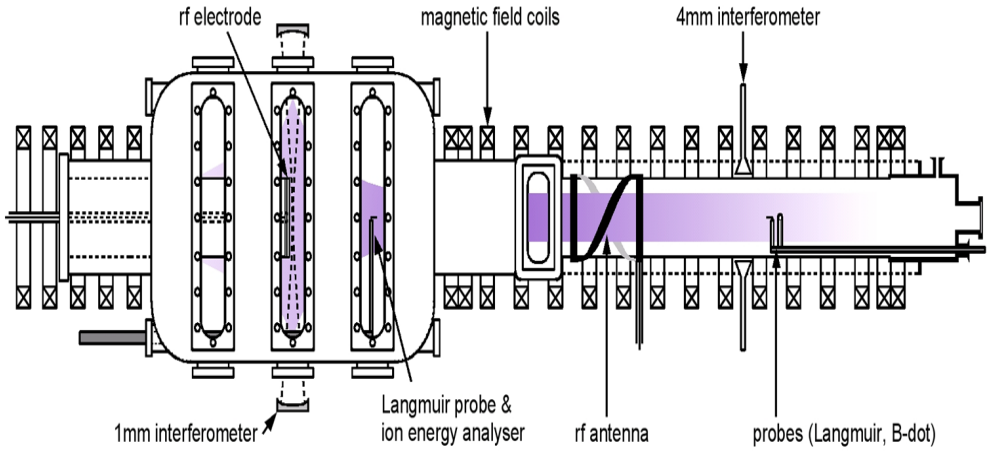

FIGURE 2.3: The schematic of HE-L [123]

by Balkey et al [82], the perpendicular ion temperature was measured by a laser induced fluorescence (LIF) system in this device. It was found that the mechanisms of power absorption for ions and electrons are distinct [82]. Another helicon device called **Mad-HeX** was built by Scharer's group in Wisconsin University–Madison [121]. It is 10 cm diameter and about 220 cm long. To compare the experimental results from this device with the numerical results, the properties of helicon plasmas in non-uniform magnetic fields were investigated [121]. In the University of Texas-Austin, a helicon source was built to study the plasma- wave interaction [122]. It consists of a Pyrex tube, with 6 cm in diameter and 30 cm in length, and a cylindrical stainless vacuum chamber with an internal diameter of 9.5 cm and a total length of 90 cm [74]. The results on the study of RLH waves were obtained in this machine. It is shown that the RLH wave plays an significant role in the power absorption of helicon plasmas [74, 75].

In Germany, a typical helicon device **HE-L** shown in Fig. 2.3 was built by Kraemer's group [98] in Ruhr University Bochum. The helicon section consists of a quartz tube with 14.6 cm diameter and 110 cm long surrounded by a set of magnetic field coils. The

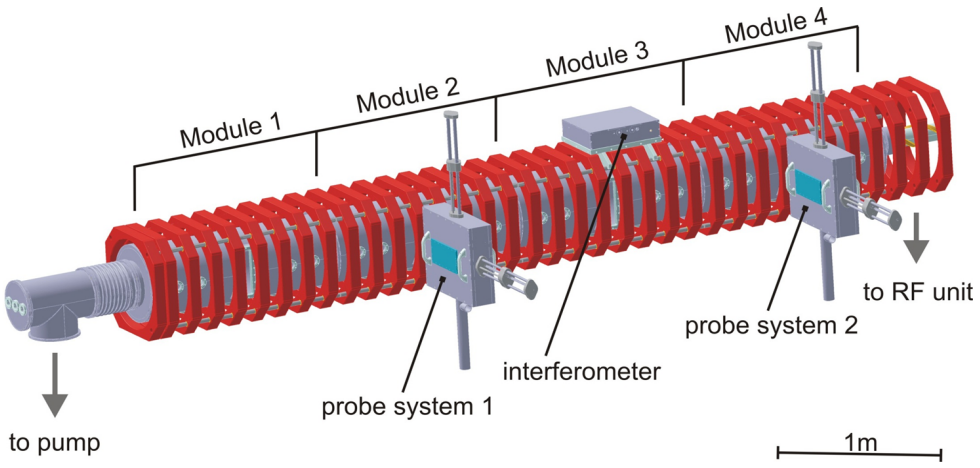

FIGURE 2.4: The schematic of VINETA [126]

plasma produced by the source is ejected into an aluminum cylinder chamber with a diameter of 24 cm and a length of 100 cm. The experiments on power absorption and parametric instability of helicon waves are carried out in this machine [98, 124]. It is concluded that the positive azimuthal modes $m = +1, +2$ have predominant contribution to the power absorption of rf power [98]. And they first evidenced the close relationship between the electrostatic fluctuations excited by parametric instability and the helicon wave absorption [124]. In addition, another large helicon machine called **VINETA** in Fig. 2.4 was built in the Max Planck Institute for Plasma Physics at Greifswald [125]. It consists of four modules, and each module has a length of about 100 cm. It allows to create a linear plasma column with overall length of 400 cm and a diameter larger than 20 cm.

Lastly, two large helicon machines were developed in Japan. The first one called **LDD** is built at Kyushu University [127]. It is 40 cm diameter and more than 126 cm long. The second machine **LHPD** is located at the Institute of Space and Astronautical Science (ISAS) [128]. The inner vessel diameter and axial length are 74 cm and 486 cm, respectively. The comparable experiments in these two devices are carried out by Shinohara et al [127]. They found that the standing wave-like patterns of the excited EM field would be manifested by reducing the ratio of the diameter to the axial length of helicon source [127]. In South Korea, a device was built at Korea Advanced Institute of Science and Technology (KAIST). The discharge tube is 25 cm in diameter, 60 cm in length and the stainless steel chamber is 30 cm in diameter, 40 cm in length. The study of the influence of lower hybrid frequency on the helicon discharge was carried out by Yun et al [52, 84]. It was found that the optimal frequency which can produce the highest plasma density is near the lower hybrid frequency and proportional to the external magnetic field and inversely proportional to the gas mass [52].

Chapter 3

General Plasma-wave Interaction Model

In the present Chapter, a general wave model in cold magnetized plasmas introduced by many researchers [102, 129] is described to give a general framework to analyze the Helicon and companion waves [102, 130], discussing the different parametric regimes for wave propagation and characterization. Based on this discussion, the two- dimensional(2D) wave model and one-dimensional(1D) wave model suitable for practical HPT configurations are derived with reasonable assumptions and boundary conditions.

We begin in section 3.1 giving the general Maxwell equations for linear waves. Then, the 0D dispersion relation in uniform plasmas and wave propagation regimes are discussed in section 3.2. The 2D and 1D plasma-wave interaction model are established in section 3.3 and 3.4, respectively. In addition, the power deposition and antenna impedance is investigated in section 3.5.

3.1. Maxwell equations and dielectric tensor

To understand the wave properties, we limit the study to linear waves, of single frequency ω propagating into a plasma where a stationary magnetic field $\boldsymbol{B}_0$ is applied. The time-varying electric field $\boldsymbol{E}$ and magnetic field $\boldsymbol{B}$ satisfy the Maxwell equations

$$\nabla \times \boldsymbol{E} = -\frac{\partial \boldsymbol{B}}{\partial t} \tag{3.1}$$

$$\nabla \times \boldsymbol{B} = \mu_0 \left(\epsilon_0 \frac{\partial \boldsymbol{E}}{\partial t} + \boldsymbol{j} + \boldsymbol{j}_a \right) \tag{3.2}$$

where μ_0 and ϵ_0 represent the permeability and permittivity in the vacuum, respectively, $\boldsymbol{j}_a$ is the external current density and $\boldsymbol{j}$ is the current density of the plasma,

$$\boldsymbol{j} = \sum_{k=i,e} n_k q_k \boldsymbol{u}_k \tag{3.3}$$

where the sum is over each plasma species k. We will assume that the plasma is constituted of electrons and single-charged ions. The density, velocity and charge of species are represented by n_k, $\boldsymbol{u}_k$ and q_k, respectively.

Then, the linearized momentum equation for cold ions and electrons at rest, under the assumption of small oscillations, is given by [102]

$$m_k \frac{\partial \boldsymbol{u}_k}{\partial t} = q_k \left(\boldsymbol{E} + \boldsymbol{u}_k \times \boldsymbol{B}_0\right) - \nu_k m_k \boldsymbol{u}_k, \tag{3.4}$$

where $\boldsymbol{B}_0$ is the static magnetic field, ν_k is an effective collision frequency and m_k is the species mass.

Next, plasma magnitudes are assumed to vary with time as $\exp(-i\omega t)$. Hence, the Fourier temporal transformation can be written as

$$\frac{\partial}{\partial t} \rightarrow -i\omega$$

Using this relation, Eq. 3.4 can be expanded in each component of Cartesian coordinates

$$-i\omega u_{xk} = \frac{q_k}{m_k} E_x + \omega_{ck} u_{yk} - \nu_k u_{xk} \tag{3.5}$$

$$-i\omega u_{yk} = \frac{q_k}{m_k} E_y - \omega_{ck} u_{xk} - \nu_k u_{yk} \tag{3.6}$$

$$-i\omega u_{zk} = \frac{q_k}{m_k} E_z - \nu_k u_{zk} \tag{3.7}$$

Therefore, the velocity is Related algebraically to the electric field. Substituting into 3.3, the tensorial Ohm's law relating the plasma current to electric field is established as [129],

$$\boldsymbol{j} = \bar{\bar{\sigma}} \boldsymbol{E} \tag{3.8}$$

where $\bar{\bar{\sigma}}$ is the conductivity tensor and has the form

$$\bar{\bar{\sigma}} = \begin{bmatrix} \sigma_1 & \sigma_2 & 0 \\ -\sigma_2 & \sigma_1 & 0 \\ 0 & 0 & \sigma_3 \end{bmatrix} \tag{3.9}$$

and each component of $\bar{\bar{\sigma}}$ can be given as

$$\sigma_1 = \sum_{k=i,e} \frac{q_k^2 n_k}{m_k} \frac{\nu_k - i\omega}{\left[(\nu_k - i\omega)^2 + \omega_{ck}^2\right]}, \tag{3.10}$$

$$\sigma_2 = \sum_{k=i,e} \frac{q_k^2 n_k}{m_k} \frac{\omega_{ck}}{\left[(\nu_k - i\omega)^2 + \omega_{ck}^2\right]}, \tag{3.11}$$

$$\sigma_3 = \sum_{k=i,e} \frac{q_k^2 n_k}{m_k} \frac{1}{\nu_k - i\omega} \tag{3.12}$$

Then, Maxwell equations become

$$\nabla \times \boldsymbol{E} = i\omega \boldsymbol{B} \tag{3.13}$$

$$\nabla \times \boldsymbol{B} = \mu_0(-i\omega \boldsymbol{D} + \boldsymbol{j}_a) \tag{3.14}$$

where the electric displacement field $\boldsymbol{D}$ satisfies

$$\boldsymbol{D} = \epsilon_0 \boldsymbol{E} + i\frac{\boldsymbol{j}}{\omega} \equiv \bar{\bar{\epsilon}} \boldsymbol{E} \tag{3.15}$$

and the permittivity tensor, bearing all plasma properties, satisfies [131]

$$\bar{\bar{\epsilon}} \equiv \epsilon_0 \bar{\bar{\kappa}}, \qquad \bar{\bar{\kappa}} = \bar{\bar{I}} + i\frac{\bar{\bar{\sigma}}}{\epsilon_0 \omega} \tag{3.16}$$

where $\bar{\bar{\kappa}}$ is the dielectric tensor and the identity matrix $\bar{\bar{I}}$ is the contribution of the displacement current; the plasma response to the waves is described by the conductivity tensor $\bar{\bar{\sigma}}$.

Assuming provisionally that $\boldsymbol{B}_0$ is parallel to $\mathbf{1}_z$ everywhere, the normalized dielectric tensor takes the form [102, 129]

$$\bar{\bar{\kappa}} = \begin{bmatrix} \kappa_1 & i\kappa_2 & 0 \\ -i\kappa_2 & \kappa_1 & 0 \\ 0 & 0 & \kappa_3 \end{bmatrix} \tag{3.17}$$

where each component can be written as

$$\kappa_1 = 1 - \sum_{k=i,e} \frac{\omega_{pk}^2 \left(\omega + i\nu_k\right)}{\omega \left[\left(\omega + i\nu_k\right)^2 - \omega_{ck}^2\right]}, \tag{3.18}$$

$$\kappa_2 = - \sum_{k=i,e} \frac{s_k \omega_{ck} \omega_{pk}^2}{\omega \left[\left(\omega + i\nu_k\right)^2 - \omega_{ck}^2\right]}, \tag{3.19}$$

$$\kappa_3 = 1 - \sum_{k=i,e} \frac{\omega_{pk}^2}{\omega \left(\omega + i\nu_k\right)} \tag{3.20}$$

where s_k is the sign of the electric charge and

$$\omega_{ck} = \frac{q_k B_0}{m_k}, \qquad \omega_{pk} = \sqrt{\frac{q_k^2 n_k}{\epsilon_0 m_k}} \tag{3.21}$$

are the cyclotron and electrostatic frequencies (of species $k = i, e$), respectively, which depend on the applied magnetic field and the plasma density.

3.2. The (0D) dispersion relation for a uniform plasma

After deriving Maxwell equations and dielectric tensor, the dispersion relation is discussed here. The dispersion relation is the equation relating the wavenumber k (or alternatively the wavelength λ) and the frequency ω. In a magnetized plasma the general dispersion relation can be very complicated. Hence, we consider first a simple case that the RF wave propagates in a uniform plasma with an applied steady magnetic field. These assumptions cause the dielectric tensor $\overline{\overline{\kappa}}$ to be constant.

Considering the Fourier spatial transformation, all quantities are expressed varying as $\exp[i(\boldsymbol{k} \cdot \boldsymbol{r} - \omega t)]$. The differential operator can be expressed as

$$\nabla \rightarrow i\boldsymbol{k}$$

where $\boldsymbol{k}$ is the wavenumber. Hence, Maxwell equations reduce to the homogeneous wave equation

$$\boldsymbol{k} \times (\boldsymbol{k} \times \boldsymbol{E}) + k_0^2 \overline{\overline{\kappa}} \cdot \boldsymbol{E} = 0 \tag{3.22}$$

where $k_0 = \omega/c$ is the vacuum wavenumber and $c = (\mu_0 \epsilon_0)^{-1/2}$ is the speed of light in vacuum. Here, the condition that the external forcing current (antenna) is outside the plasma has been applied. We now choose the wavenumber $\boldsymbol{k}$ to lie in the x-z plane, so

that Eq. 3.22 can be written in the matrix form

$$\begin{bmatrix} N^2\cos^2\theta-\kappa_1 & -i\kappa_2 & -N^2\cos\theta\sin\theta \\ i\kappa_2 & N^2-\kappa_1 & 0 \\ -N^2\cos\theta\sin\theta & 0 & N^2\sin^2\theta-\kappa_3 \end{bmatrix} \begin{bmatrix} E_x \\ E_y \\ E_z \end{bmatrix} = 0 \tag{3.23}$$

where θ is the angle between the wavenumber $\boldsymbol{k}$ and the magnetic field B_0 and $N = kc/\omega$. Thus, non-trivial solutions of the wave equation exist only for those pairs $(\omega, \boldsymbol{k})$ that make the matrix singular,

$$\det \begin{bmatrix} N^2\cos^2\theta-\kappa_1 & -i\kappa_2 & -N^2\cos\theta\sin\theta \\ i\kappa_2 & N^2-\kappa_1 & 0 \\ -N^2\cos\theta\sin\theta & 0 & N^2\sin^2\theta-\kappa_3 \end{bmatrix} = 0 \tag{3.24}$$

This determinant is a 2nd-order polynomial for N^2 [102, 129]

$$a_4 N^4 + a_2 N^2 + a_0 = 0 \tag{3.25}$$

where

$$\begin{aligned} a_4 &= \kappa_1 \sin^2\theta + \kappa_3 \cos^2\theta, \\ a_2 &= \left(\kappa_2^2 - \kappa_1^2\right)\sin^2\theta - \kappa_1\kappa_3(1+\cos^2\theta), \\ a_0 &= \left(\kappa_1^2 - \kappa_2^2\right)\kappa_3, \end{aligned} \tag{3.26}$$

For each wavenumber angle, there are two different solutions for N^2, corresponding to two pairs of waves and two different polarizations (left- and right-handed) [102, 129]. The helicon wave belongs to the right-hand polarized waves [18].

In order to discuss the parametric regime easily, an alternative equivalent way of expressing the dispersion relation is taken into account [108]

$$\hat{a}_4 \hat{N}^4 + \hat{a}_2 \hat{N}^2 + \hat{a}_0 = 0 \tag{3.27}$$

where $\hat{N} = kd_e$ and $d_e = c/\omega_{pe}$ is the skin depth of electrons. Here, the coefficients are

$$\begin{aligned} \hat{a}_4 &= \hat{\kappa}_1 \sin^2\theta + \hat{\kappa}_3 \cos^2\theta, \\ \hat{a}_2 &= \left(\hat{\kappa}_2^2 - \hat{\kappa}_1^2\right)\sin^2\theta - \hat{\kappa}_1\hat{\kappa}_3(1+\cos^2\theta), \\ \hat{a}_0 &= \left(\hat{\kappa}_1^2 - \hat{\kappa}_2^2\right)\hat{\kappa}_3, \end{aligned} \tag{3.28}$$

Also, we have the relation

$$\hat{\kappa}_j = \kappa_j \frac{\omega^2}{\omega_{pe}^2}$$

Next, we will discuss the parametric regime of wave propagations based on the dispersion relation.

3.2.1. The helicon conventional frequency regime

The most conventional parametric regime for helicon wave propagation corresponds to [40, 45]

$$\nu_e, \omega_{lh} \ll \omega < \omega_{ce} \ll \omega_{pe}, \tag{3.29}$$

where $\omega_{lh} = eB_0/\sqrt{m_e m_i}$ is the lower-hybrid frequency. In this regime, the components of the dielectric tensor reduce to

$$\hat{\kappa}_1 = -\frac{\omega(\omega + i\nu_e)}{(\omega + i\nu_e)^2 - \omega_{ce}^2}, \qquad \hat{\kappa}_2 = \frac{\omega_{ce}\omega}{(\omega + i\nu_e)^2 - \omega_{ce}^2}, \qquad \hat{\kappa_3} = -\frac{\omega}{\omega + i\nu_e} \tag{3.30}$$

which point out that the wave frequency ω is too low to take into account the displacement current and too high to include the effects of the ion oscillations. Then the solution of Eq. 3.27 is [45, 132]

$$\hat{N} \equiv k^2 d_e^2 = \frac{\omega}{\pm\omega_{ce}\,|\cos\theta| - (\omega + i\nu_e)} \tag{3.31}$$

Hence, waves propagate only for the + sign in the denominator, for the θ angles where the refractive index is dominantly real. It is customary to denote the low-θ waves (long wavelength) as helicon mode and the high θ waves (short wavelength) as Trievelpiece-Gould (TG) modes [27, 63].

We can decompose k into the parallel and perpendicular wavenumbers $k_\parallel = k\cos\theta$ and $k_\perp = k|\sin\theta|$. When plotting this relation in the form of $k_\perp\left(k_\parallel\right)$, Fig. 3.1 shows the variation of the perpendicular wavenumber $k_\perp de$ with changing the parallel wavenumber $k_\parallel de$ for different ω_{ce}/ω. The two solution of $k_\perp de$ for a specific value of $k_\parallel de$ means the propagation of two branch of waves, TG mode and helicon mode. With a larger value of $\omega_c e/\omega$, the regime which can propagate two waves become wider. Therefore, it is necessary to show the full picture of wave propagation for different frequency ratios. With finding the boundary of solution of perpendicular wavenumber, three regimes are distinguished[44] in Fig. 3.2(a), for a wider frequency range than that expressed by Eq. (3.29):

1. Inductive regime(ICR), when $\omega_{ce}/\omega < 1$ for all $k_\parallel d_e$, $1 \le \omega_{ce}/\omega \le 2$ for $k_\parallel d_e < \sqrt{1/\left(\omega_{ce}/\omega - 1\right)}$ or $\omega_{ce}/\omega > 2$ for $k_\parallel d_e < 2\omega_{ce}/\omega$. There is no real solution for $k_\perp$, which means that no wave propagates. RF emission is evanescent in the plasma, penetrates only into a skin depth of the plasma column and/or is reflected.

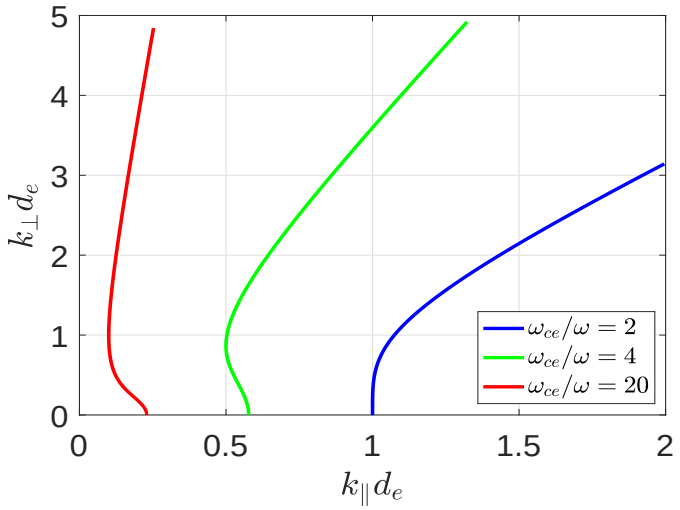

FIGURE 3.1: The relation between perpendicular wavenumber and parallel wavenumber for different frequency ratio.

2. Surface wave regime(SWR), when $k_\parallel d_e > \sqrt{1/\left(\omega_{ce}/\omega - 1\right)}$. Only the TG wave propagates. This is quickly damped for $\nu_e \neq 0$.

3. Double wave regime(DWR), when $2\omega/\omega_{ce} < k_\parallel d_e < \sqrt{1/\left(\omega_{ce}/\omega - 1\right)}$. Both helicon and TG waves propagate. The helicon wave is weakly damped and propagates the whole radius of the plasma column [62].

3.2.2. The helicon extended frequency regime

As the wave frequency decreases, ion oscillations are more likely to influence the plasma response. Taking into account that

$$\omega_{pi} = \sqrt{\frac{m_e}{m_i}}\omega_{pe}, \quad \omega_{lh} = \sqrt{\frac{m_e}{m_i}}\omega_{ce}, \quad \omega_{ci} = \frac{m_e}{m_i}\omega_{ce}, \tag{3.32}$$

a straightforward comparison of the electron and ion contributions to the dielectric components in Eq. 3.18-3.20 shows that the ion contribution becomes significant: when $\omega \sim \omega_{lh}$ for $\hat{\kappa}_1$, when $\omega \sim \omega_{ci}$ for $\hat{\kappa}_2$, and never for $\hat{\kappa}_3$. Therefore, for $\omega \gg \omega_{ci}$, the ion contribution needs to be included only in $\hat{\kappa}_1$. The generalized expression is

$$\hat{\kappa}_1 = -\omega\left[\frac{\omega + i\nu_e}{(\omega + i\nu_e)^2 - \omega_{ce}^2} + \frac{m_e}{m_i}\frac{\omega + i\nu_i}{(\omega + i\nu_i)^2 - \omega_{ci}^2}\right], \tag{3.33}$$

Solving now dispersion relation Eq. 3.27 in the collisionless limit, the wave propagation regimes for argon are plotted in Fig. 3.2(b). The solid straight line is the separatrix corresponding to the lower hybrid frequency. The electromagnetic waves show different

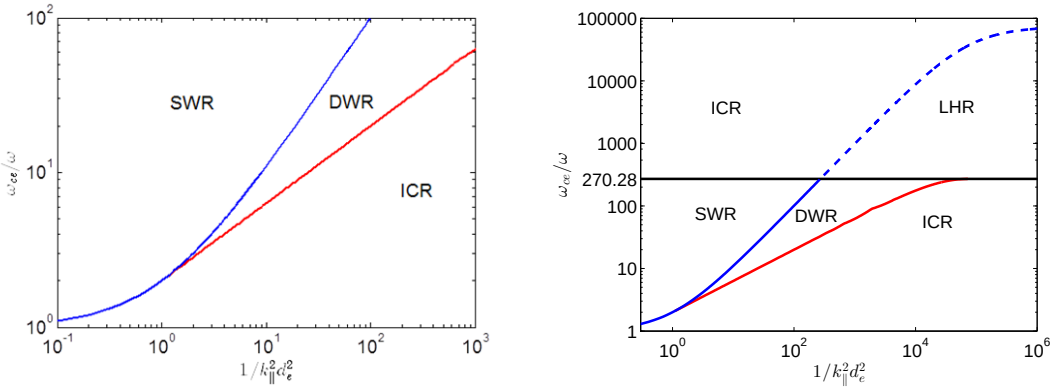

(a) The high frequency regime

(b) The extended frequency regime

FIGURE 3.2: Wave propagation regimes for high frequencies

behaviours in the different regimes. The three regimes below the straight line have been presented in previous section. Here, we focus on the regimes above the line. Two regimes are distinguished:

1. Inductive regime(ICR). There is no real solution for $k_\perp$. Thus, no wave propagates, RF emission penetrates only into a skin depth of the plasma column.

2. Low frequency helicon wave regime(LHR). Only helicon waves propagates.

In order to have a general view of wave propagations with variation of frequency, the relation between ω_{ce}/ω and $k_\perp$ is plotted in Fig. 3.3. It shows the perpendicular wavenumber as a function of the ratio ω_{ce}/ω at a fixed plasma density. Two different parallel wavenumbers are selected to compare, $k_\parallel = 17.1$ and $34.2\ m^{-1}$. Therefore, the corresponding dimensionless parameter $k_\parallel d_e$ are 0.0384 and 0.0768, respectively. The Collisional and collisionless cases are also compared. Only two axial modes are shown in order to illustrate the wave propagation in the different regimes. In the collisionless case, there are two roots for $k_\perp$, representing the helicon wave and the TG wave [27]. At low values of ω_{ce}/ω, in the ICR, there is no real solution for $k_\perp$. With ω_{ce}/ω increasing, two kinds of waves propagate in the DWR. As the ratio ω_{ce}/ω increases, the perpendicular wavenumber for the slow wave (TG wave) tend to infinite when $\omega = \omega_{lh}$. The perpendicular wavenumber of the fast wave (HE wave) becomes very small. In $k_\parallel = 17.1$ case, it will not go through the TG regime, therefore the $k_\perp$ of HE wave are not zero near the lower hybrid frequency. In comparison, the $k_\perp$ of HE wave when $k_\parallel = 34.2$ is zero in this regime. When $\omega < \omega_{lh}$, the real part of $k_\perp$ of TG wave tends to be zero and become purely imaginary. For HE waves, $k_\parallel = 17.1$ will be in the LHR, the real and imaginary part of HE wave both become small. And it goes to zero when entering the ICR. $k_\parallel = 34.2$ enters in the ICR directly, so the blue lines are still zero.

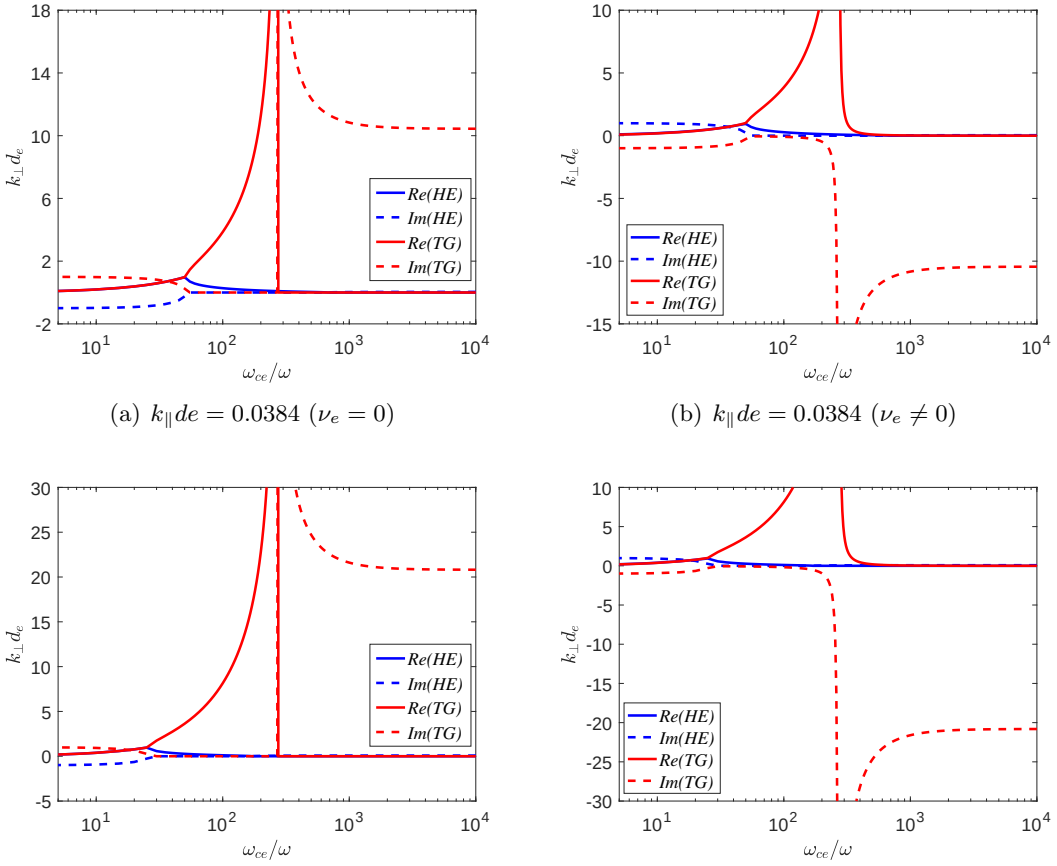

(a) $k_\parallel de = 0.0384$ ($\nu_e = 0$)

(b) $k_\parallel de = 0.0384$ ($\nu_e \neq 0$)

(c) $k_\parallel de = 0.0768$ ($\nu_e = 0$)

(d) $k_\parallel de = 0.0768$ ($\nu_e \neq 0$)

FIGURE 3.3: The perpendicular wavenumber $k_\perp$ is given as functions of the ratio ω_{ce}/ω. The plasma density is 5.6×10^{18} m^{-3}; the parallel wavenumbers $k_\parallel$, are 17.1 m^{-1} and 34.2 m^{-1}. The corresponding dimensionless parameter $k_\parallel de$ are 0.0384 and 0.0768, respectively. In the collisional case, the electron collision frequency is 3.26MHz. The blue lines represent the helicon wave and the red lines is the TG wave. The solid and the dashed line represent the real and imaginary parts, respectively. The magnitude of TG wavenumber is too large to display in the figure with the given scale near the region where $\omega \sim \omega_{lh}$.

For the collisional case, there are some changes caused by ν_e. The sign of imaginary part is changed. In addition, there is a knee in the profile of TG mode near the lower hybrid frequency, and there is no big difference between the LHR and the ICR. The purely imaginary part of TG mode is quite large and the real part of HE and TG waves are very small. The evanescent behaviour dominates the wave propagation.

3.3. The axisymmetric 2D model

The discussion of the dispersion relation for an infinite, uniform plasma has shown us the general features and regimes for the propagation of the helicon-type waves and their companions, the short-wavelength TG waves. With this general frame in mind we begin

to study the helicon wave propagation in a real helicon source immersed in a vacuum chamber.

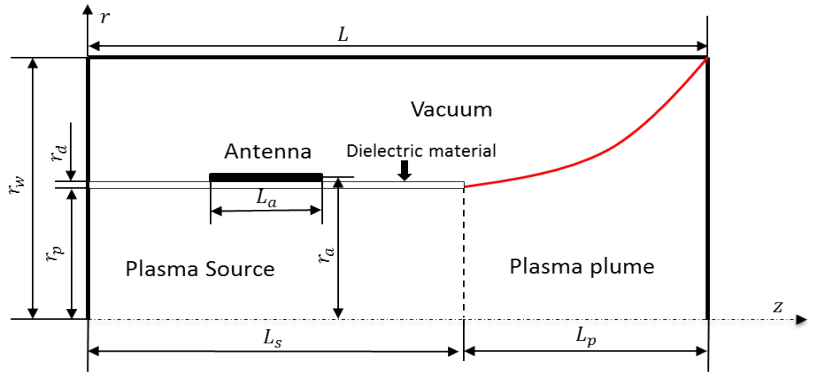

FIGURE 3.4: Geometric structure of 2D model.

The helicon source system is made up of a dielectric cylindrical vessel, where the plasma is produced, an external RF antenna wrapped around the chamber and a set of external coils to produce the applied magnetic field [15]. The cylinder chamber is made of a dielectric material, such as quartz. A gas feed system is set up at one end of the chamber. The antenna emits electromagnetic radiation of frequency ω in the range 1–100 MHz [18]. The plasma is confined radially by the applied axial magnetic field B_0, created by the external coils (which are assumed to have no effects on the plasma-wave interaction) [15, 19].

Figure 3.4 sketches the typical arrangement we will model and analyze. Cylindrical coordinates are used. There is a conducting cavity (simulating the walls of a vacuum chamber) of length L and radius r_w where the helicon source is immersed. This source is made of a cylindrically dielectric tube that confines the plasma, which is then emitted as a divergent beam. The thickness of the dielectric tube is r_d. Therefore, the plasma will be considered as a column of varying radius $r_p(z)$ whose density $n(r, z)$ is assumed to be known for present purposes. A set of coils creates the stationary axisymmetric magnetic field

$$\boldsymbol{B}_0(r, z) = B_0(r, z)(\mathbf{1}_r \sin\alpha + \mathbf{1}_z \cos\alpha) \tag{3.34}$$

where $\alpha(r, z)$ is the local magnetic angle with the axial direction $\mathbf{1}_z$. The rf antenna is constituted by a thin conducting wire wrapped, at a distance r_a, with different 3D geometric forms (Nagoya type, helical type, etc.) around the helicon source.

Except for very few cases (like a single loop), the 3D geometric form of the antenna makes the problem 3D in space. Using cylindrical coordinates and time-transformed Maxwell equations, Eq. 3.13-3.14 can be expanded to the set of six scalar equations for

EM fields

$$\frac{1}{r}\frac{\partial E_z}{\partial \theta} - \frac{\partial E_\theta}{\partial z} - i\omega B_r = 0, \tag{3.35}$$

$$\frac{\partial E_r}{\partial z} - \frac{\partial E_z}{\partial r} - i\omega B_\theta = 0, \tag{3.36}$$

$$\frac{1}{r}\frac{\partial}{\partial r}(rE_\theta) - \frac{1}{r}\frac{\partial E_r}{\partial \theta} - i\omega B_z = 0, \tag{3.37}$$

$$\frac{1}{r}\frac{\partial B_z}{\partial \theta} - \frac{\partial B_\theta}{\partial z} + i\omega\mu_0 D_r = \mu_0 j_{ra}, \tag{3.38}$$

$$\frac{\partial B_r}{\partial z} - \frac{\partial B_z}{\partial r} + i\omega\mu_0 D_\theta = \mu_0 j_{\theta a}, \tag{3.39}$$

$$\frac{1}{r}\frac{\partial}{\partial r}(rB_\theta) - \frac{1}{r}\frac{\partial B_r}{\partial \theta} + i\omega\mu_0 D_z = \mu_0 j_{za} \tag{3.40}$$

where $\boldsymbol{j}_a = (j_{ra}, j_{\theta a}, j_{za})$ is the 3D contribution of the antenna, and the dielectric tensor must be written in the cylindrical coordinate system, i.e. satisfying

$$(D_r, D_\theta, D_z)^T = \epsilon_0 \bar{\bar{\kappa}}(r,z) \cdot (E_r, E_\theta, E_z)^T, \tag{3.41}$$

Making the appropriate rotation of the system of reference, from the $\boldsymbol{B}_0$-aligned one to the cylindrical one, the normalized dielectric tensor takes the form [130, 133]

$$\bar{\bar{\kappa}}(r,z) = \begin{pmatrix} \kappa_1(\cos\alpha)^2 + \kappa_3(\sin\alpha)^2 & i\kappa_2\cos\alpha & \frac{\kappa_3-\kappa_1}{2}\sin 2\alpha \\ -i\kappa_2\cos\alpha & \kappa_1 & i\kappa_2\sin\alpha \\ \frac{\kappa_3-\kappa_1}{2}\sin 2\alpha & -i\kappa_2\sin\alpha & \kappa_3(\cos\alpha)^2 + \kappa_1(\sin\alpha)^2 \end{pmatrix} \tag{3.42}$$

Since $\bar{\bar{\kappa}}(r,z)$ and the domain is axysimmetric, the three-dimensionality comes only from the antenna wire geometry. If the antenna and near-field around it need to be analyzed, it could be modelled similarly to the plasma, as a metallic material with conductivity $\bar{\bar{\sigma}}_a(r,\theta,z)$, and Ohm's law

$$\boldsymbol{j}_a = \bar{\bar{\sigma}}_a \boldsymbol{E}, \tag{3.43}$$

and this equation must be implemented in the RHS of Eq. 3.14. This approach is not going to be followed here because the influence of the antenna conductivity on the power absorption in the bulk of the plasma is expected to be small. Taking into account that the typical rf wavelength is much larger than the antenna length, the antenna wire is being assumed to be very thin and that the current concentrates on the surface [134]. Additionally, the antenna wire is seen as a perfect conductor so that the power loss inside antenna is generally assumed to be negligible. Hence, the variation of current density inside the antenna in the r direction is not taken into account and the radial component of this current is $j_{ra} = 0$. Considering the magnitude of current I_a which

oscillates with frequency ω, we can write [134, 135]

$$\boldsymbol{j}_a(\boldsymbol{r},t) = I_a \exp(-i\omega t)\left[\mathbf{1}_z s_z(r,\theta,z) + \mathbf{1}_\theta s_\theta(r,\theta,z)\right] \tag{3.44}$$

where s_z and s_θ are functions defining the geometry of antenna. This expression of $\boldsymbol{j}_a$ admits a Fourier transform in the azimuthal direction,

$$\frac{\partial}{\partial\theta} \to im, \quad m \in Z \tag{3.45}$$

yielding

$$s_z(r,\theta,z) = \sum_{\forall m\in Z} s_z^{(m)}(r,z)\exp(im\theta), \tag{3.46}$$

and similarly for $s_\theta(r,\theta,z)$. Performing now the Fourier θ-transform in the above 3D Maxwell equations we obtain for *for each m-mode* of the electromagnetic field [74, 76]

$$\frac{im}{r}E_z - \frac{\partial}{\partial z}E_\theta - i\omega B_r = 0, \tag{3.47}$$

$$\frac{\partial}{\partial z}E_r - \frac{\partial}{\partial r}E_z - i\omega B_\theta = 0, \tag{3.48}$$

$$\frac{1}{r}\frac{\partial}{\partial r}(rE_\theta) - \frac{im}{r}E_r - i\omega B_z = 0, \tag{3.49}$$

$$\frac{im}{r}B_z - \frac{\partial}{\partial z}B_\theta + i\omega\mu_0 D_r = 0, \tag{3.50}$$

$$\frac{\partial}{\partial z}B_r - \frac{\partial}{\partial r}B_z + i\omega\mu_0 D_\theta = \mu_0 j_{\theta a}, \tag{3.51}$$

$$\frac{1}{r}\frac{\partial}{\partial r}(rB_\theta) - \frac{im}{r}B_r + i\omega\mu_0 D_z = \mu_0 j_{za} \tag{3.52}$$

where superscript (m) has been omitted for $\boldsymbol{E}$, $\boldsymbol{B}$, $\boldsymbol{D}$ and $\boldsymbol{j}_a$. This 2D model of partial differential equations can be solved with numerical method, such as Finite Difference Method(FDM) or Finite Element Method(FEM) [74]. The former approach will be carried out in Chapter 6 in detail.

3.4. The radial 1D model

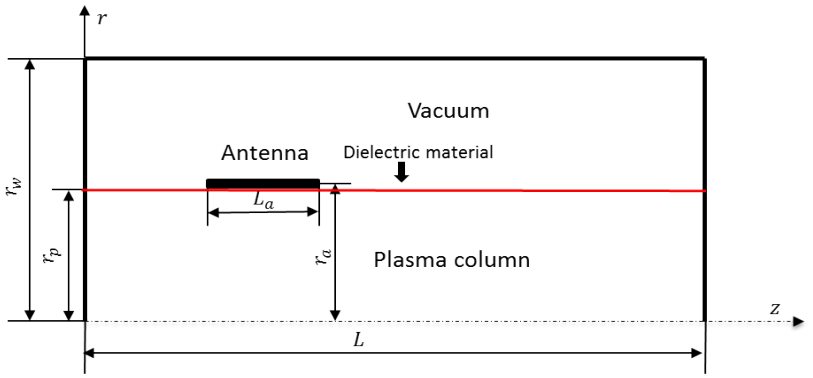

FIGURE 3.5: Geometric structure of 1D model.

Although the 2D model is the most valuable one to analyze practical configurations of the helicon source, its numerical implementation and solving are still too cumbersome for carrying out parametric studies. This explains that a simpler 1D radial model with limited axial variations has been the most popular choice in research studies of the helicon wave propagation [55, 59, 70]. This model would correspond to the simplified configuration depicted in Fig. 3.5 where $\boldsymbol{B}_0$ is purely axial ($\alpha = 0$) and both B_0 and plasma properties change only in the r-direction [41, 71], thus leading to the dielectric tensor $\bar{\bar{\kappa}} = \bar{\bar{\kappa}}(r)$.

The plasma is here limited to the purely axially-uniform finite cylinder structure, and the plasma plume is not taken into account. This allows applying the additional Fourier z-transform

$$\frac{\partial}{\partial z} \rightarrow ik_z, \qquad k_z \in R \tag{3.53}$$

to the above 2D model equations. Nonetheless, before performing the axial Fourier transformation, the boundary conditions at the axial end of the domain $z = 0$ and $z = L$ are considered. There, since the cavity walls are assumed to be metallic, reflection conditions are applied [55, 59]

$$E_r(0) = E_\theta(0) = 0, \qquad E_r(L) = E_\theta(L) = 0, \tag{3.54}$$

As a consequence, the Fourier transform of these two fields can be written in the form of sin series

$$E_r, E_\theta \propto \sin k_z z, \quad k_z = \frac{l\pi}{L} \quad l \in N$$

Then, considering the set of six Maxwell equations, it is found that the most suitable Fourier-transformation is [55, 59],

$$\begin{pmatrix} E_r(r,\theta,z,t) \\ E_\theta(r,\theta,z,t) \\ B_z(r,\theta,z,t) \end{pmatrix} = \sum_{l,m} \begin{pmatrix} E_r^{(l,m)}(r) \\ E_\theta^{(l,m)}(r) \\ B_z^{(l,m)}(r) \end{pmatrix} \sin\left(\frac{l\pi}{L}z\right) \exp\left[i\left(m\theta - \omega t\right)\right] \tag{3.55}$$

$$\begin{pmatrix} B_r(r,\theta,z,t) \\ B_\theta(r,\theta,z,t) \\ E_z(r,\theta,z,t) \end{pmatrix} = \sum_{l,m} \begin{pmatrix} B_r^{(l,m)}(r) \\ B_\theta^{(l,m)}(r) \\ E_z^{(l,m)}(r) \end{pmatrix} \cos\left(\frac{l\pi}{L}z\right) \exp\left[i\left(m\theta - \omega t\right)\right] \tag{3.56}$$

provided that the current densities of the antenna are transformed as

$$j_\theta(r,\theta,z,t) = \sum_{l,m} j_\theta^{(l,m)}(r) \sin\left(\frac{l\pi}{L}z\right) \exp i(m\theta - \omega t) \tag{3.57}$$

$$j_z(r,\theta,z,t) = \sum_{l,m} j_z^{(l,m)}(r) \cos\left(\frac{l\pi}{L}z\right) \exp i(m\theta - \omega t) \tag{3.58}$$

Therefore, the 1D model *for each* (l,m) *mode* is [55, 59, 70, 105]

$$\frac{im}{r}E_z - k_z E_\theta - i\omega B_r = 0, \tag{3.59}$$

$$k_z E_r - \frac{\partial}{\partial r}E_z - i\omega B_\theta = 0, \tag{3.60}$$

$$\frac{1}{r}\frac{\partial}{\partial r}(rE_\theta) - \frac{im}{r}E_r - i\omega B_z = 0, \tag{3.61}$$

$$\frac{im}{r}B_z + k_z B_\theta + i\omega\mu_0(\kappa_1 E_r + i\kappa_2 E_\theta) = 0, \tag{3.62}$$

$$k_z B_r - \frac{\partial}{\partial r}B_z + i\omega\mu_0(\kappa_1 E_\theta - i\kappa_2 E_r) = \mu_0 j_{\theta a}, \tag{3.63}$$

$$\frac{1}{r}\frac{\partial}{\partial r}(rB_\theta) - \frac{im}{r}B_r + i\omega\mu_0\kappa_3 E_z = \mu_0 j_{za} \tag{3.64}$$

and superscripts (l,m) have been again dropped for simplicity. Notice that the first and fourth of the equations above are now algebraic, while the other four have become ordinary differential equations, making the integration much simpler. The solution of this 1D model will be extensively studied in the following Chapters.

3.5. Power deposition and antenna Impedance

From the viewpoint of time-averaged energy flow, the helicon plasma thruster can be regarded as a two-terminal antenna, fed by an electrical circuit, that is radiating into the plasma volume and into space. The (resistive) input power at the antenna terminals,

P_{in}, is then divided into resistive losses in the antenna material P_{copper}, power absorbed by the plasma P_{abs}, and power lost as radiation into empty space P_{space},

$$P_{in} = P_{copper} + P_{abs} + P_{space} \tag{3.65}$$

This last contribution is non-existent when modeling the plasma discharge in a closed perfect conductor cavity such as a laboratory vacuum chamber, since any escaping radiation is reflected back by this boundary condition. Moreover, if we consider an ideal conductor antenna, P_{copper} is also zero. Under these assumptions, we can equate the time-averaged power at the input with the time-averaged power absorbed by the plasma,

$$P_{in} = P_{abs}. \tag{3.66}$$

In order to obtain a model for P_{abs}, the instantaneous power dP_{inst} delivered to a differential plasma volume $d\Omega$ by the electromagnetic field is considered, which is given by Joule's dissipation,

$$dP_{inst} = \tilde{\boldsymbol{j}} \cdot \tilde{\boldsymbol{E}} d\Omega. \Rightarrow dP_{abs} = \frac{1}{T}\int_0^T (dP_{inst})dt \tag{3.67}$$

For harmonic fields that vary as $\exp(-i\omega t)$, the instantaneous power is the sum of a time-varying contribution at frequency 2ω plus an average value. It is customary to define the *resistive or true* power dP and the *reactive* power dQ at each differential volume in the plasma. Writing $\tilde{\boldsymbol{j}}$ and $\tilde{\boldsymbol{E}}$ using the complex vector amplitudes,

$$\tilde{\boldsymbol{j}} = \frac{1}{2}\left(\boldsymbol{j}\exp(-i\omega t) + \boldsymbol{j}^*\exp(i\omega t)\right), \tag{3.68}$$

$$\tilde{\boldsymbol{E}} = \frac{1}{2}\left(\boldsymbol{E}\exp(-i\omega t) + \boldsymbol{E}^*\exp(i\omega t)\right), \tag{3.69}$$

we define these powers through the following expression:

$$dP + idQ = \frac{\boldsymbol{j}^* \cdot \boldsymbol{E}}{2} d\Omega. \tag{3.70}$$

Note that this does not represent the full product of Eq. (3.67), but only one of the four terms that come out of it[1]. It is stressed that the instantaneous power dP_{inst} is *not* equal to $dP + idQ$; however, dP and dQ contain all the necessary information to reconstruct dP_{inst} (except for the phase of the 2ω signal). Moreover, it can be proven that $dP_{abs} \equiv dP$ in the plasma, the only remaining term after time-averaging.

Considering Maxwell's equations Eq. (3.13)–(3.14), the integral of this last expression over the plasma domain Ω_p (which includes any vaccum parts but excludes the antenna)

[1] Observe that the 2ω power term is non-zero even in a purely resistive case

can be written as

$$\begin{aligned}\frac{1}{2}\int_{\Omega_p}\boldsymbol{j}^*\cdot\boldsymbol{E}d\Omega &= \frac{1}{2}\int_{\Omega_p}\left(\frac{1}{\mu_0}\nabla\times\boldsymbol{B}^*-i\omega\varepsilon_0\boldsymbol{E}^*\right)\cdot\boldsymbol{E}d\Omega \\ &= \frac{1}{2}\int_{\Omega_p}\left[\frac{1}{\mu_0}\boldsymbol{B}^*\cdot\nabla\times\boldsymbol{E}-\frac{1}{\mu_0}\nabla\cdot(\boldsymbol{E}\times\boldsymbol{B}^*)-\boldsymbol{E}\cdot i\omega\varepsilon_0\boldsymbol{E}^*\right]d\Omega \\ &= \frac{1}{2}\int_{\Omega_p}\left[-\frac{1}{\mu_0}\nabla\cdot(\boldsymbol{E}\times\boldsymbol{B}^*)+i\omega\left(\frac{1}{\mu_0}\boldsymbol{B}\cdot\boldsymbol{B}^*-\varepsilon_0\boldsymbol{E}\cdot\boldsymbol{E}^*\right)\right]d\Omega\end{aligned} \tag{3.71}$$

where Poynting's vector is defined as [136]

$$\boldsymbol{S}=\frac{1}{2\mu_0}\left(\boldsymbol{E}\times\boldsymbol{B}^*\right), \tag{3.72}$$

and the electric and magnetic energy densities in vacuum are:

$$w_e=\frac{1}{4}\varepsilon_0\left(\boldsymbol{E}\cdot\boldsymbol{E}^*\right), \quad w_m=\frac{1}{4\mu_0}\left(\boldsymbol{B}\cdot\boldsymbol{B}^*\right). \tag{3.73}$$

With these definitions, and applying Gauss integral theorem, the following law of conservation of energy is readily obtained in the plasma volume

$$\frac{1}{2}\int_{\Omega_p}\boldsymbol{j}^*\cdot\boldsymbol{E}d\Omega=2i\omega\int_{\Omega_p}\left(w_m-w_e\right)d\Omega-\int_{\partial\Omega_p}\boldsymbol{S}\cdot\boldsymbol{\nu}d\sigma. \tag{3.74}$$

where the last term is the surface integral describing the radiation power flowing through the boundary of Ω_p, whose normal unit vector pointing outwards is $\boldsymbol{\nu}$. It is zero at the outer boundary of Ω_p as the metallic chamber walls reflect all incoming radiation; the integral of Poynting's vector is only non-zero at the interface with the radiating antenna, through which all power is flowing into the plasma.

Analogously, the conservation of energy can be applied to the antenna volume Ω_a. In this case, the Poynting term includes the power radiated to the plasma through the boundary $\partial\Omega_p$ plus the resistive and reactive power at the antenna terminals,

$$\frac{1}{2}\int_{\Omega_a}\boldsymbol{j}_a^*\cdot\boldsymbol{E}d\Omega=2i\omega\int_{\Omega_a}\left(w_m-w_e\right)d\Omega+\int_{\partial\Omega_p}\boldsymbol{S}\cdot\boldsymbol{\nu}d\sigma+\frac{V_aI_a^*}{2}. \tag{3.75}$$

Combining Eqs. (3.74) and (3.75) finally leads to

$$\frac{1}{2}\int_{\Omega_p}\boldsymbol{j}^*\cdot\boldsymbol{E}d\Omega+\frac{1}{2}\int_{\Omega_a}\boldsymbol{j}_a^*\cdot\boldsymbol{E}d\Omega+2i\omega\int_{\Omega_p+\Omega_a}\left(w_e-w_m\right)d\Omega=\frac{V_aI_a^*}{2}. \tag{3.76}$$

As we have neglected the resistive losses in the antenna, the second term is purely imaginary, and the real part of this equation gives the absorbed power, P_{abs}, which then

coincides with the resistive or true power P at the antenna terminals:

$$P_{abs} = \Re\left[\frac{1}{2}\int_{\Omega_p} \boldsymbol{j}^* \cdot \boldsymbol{E} d\Omega\right] = \Re\left[\frac{V_a I_a^*}{2}\right]. \tag{3.77}$$

On the other hand, the reactive power Q at the antenna terminals is given by the imaginary part of this equation,

$$Q = \Im\left[\frac{1}{2}\int_{\Omega_p} \boldsymbol{j}^* \cdot \boldsymbol{E} d\Omega\right] + \frac{1}{2}\int_{\Omega_a} \boldsymbol{j}_a^* \cdot \boldsymbol{E} d\Omega + 2i\omega \int_{\Omega_p+\Omega_a} (w_e - w_m)\, d\Omega \tag{3.78}$$

$$= \Im\left[\frac{V_a I_a^*}{2}\right]. \tag{3.79}$$

Observe that the reactive power has contributions due to the plasma, the antenna, and the electromagnetic power stored in the fields.

Lastly, the *apparent power* S at the antenna terminals is defined as $S = \sqrt{P^2 + Q^2}$. The powers P, Q, S are directly related to the *input impedance at the antenna terminals*[2],

$$Z = R - iX.$$

i.e.,

$$P = \frac{|I|^2}{2} R, \tag{3.80}$$

$$Q = \frac{|I|^2}{2} X, \tag{3.81}$$

$$S = \frac{|I|^2}{2} Z, \tag{3.82}$$

and the angle $\alpha = \arctan(X/R)$ in the power triangle coincides with the argument of the impedance. The cosine of this angle, $\cos\alpha$, is generally known as the power factor of the antenna-plasma system.

To conclude, observe that for a given $\boldsymbol{j}_a$ the computation of P and Q can be carried out, besides using the integral definitions above, by computing the potential difference V_a between the antenna terminals. For a thin antenna, this is given by the surface integral over the area supported on the antenna of the time derivative of the magnetic flux. Equivalently, it can be computed as the line integral of the electric field along the antenna line:

$$V_a = \int_{\Gamma_a} \boldsymbol{E} \cdot d\boldsymbol{\ell}. \tag{3.83}$$

[2]Note that this definition of impedance takes the opposite sign for the reactance to that conventionally used in circuit theory

Chapter 4

The 1D Plasma-wave interaction Model

The Fourier-transformed 1D finite-cylinder model has been presented in Chapter 3. This system has been introduced by numerous authors and widely used in the study of helicon sources [18, 55, 59, 100, 104, 107]. This chapter will focus on the mathematical treatment of the model, particular in boundary conditions, antenna source terms, numerical integration and the convergence of Fourier series. Next Chapter will afford a systematically parametric investigation of the parameters characterizing the source with the aim of addressing a source preliminary design.

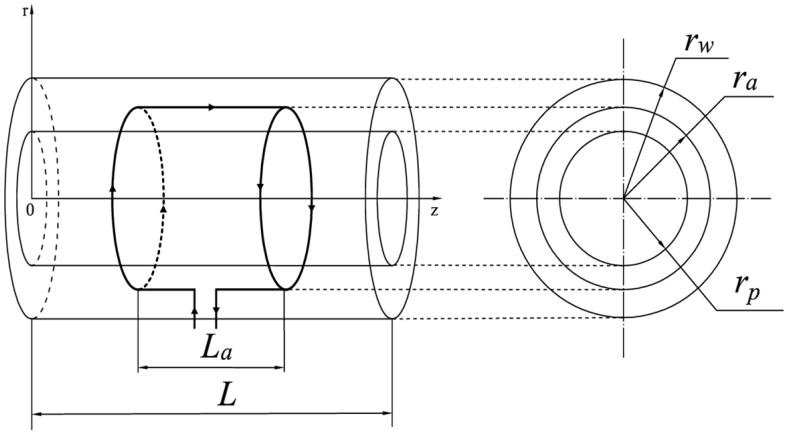

FIGURE 4.1: Geometric structure of 1D model.

4.1. 1D plasma-wave model

In order to describe 1D finite-cylinder model clearly, we show the structure of 1D finite-cylinder model in a different way from Fig. 3.5. Fig. 4.1 presents the geometry of the finite-cylinder model with Nagoya antenna (although any antenna type can be applied). A vessel of length L (placed between $z = 0$ and $z = L$) and radius r_w contains a plasma column of radius r_p, surrounded by an antenna located around $r = r_a$ and with an axial extension L_a. At the conducting wall of vessel, the tangential electric field is zero due to applying reflection boundary conditions.

An important assumption on the antenna was already made in Chapter. 3. The antenna is represented by a perfectly-conducting wire carrying a current I_a along its surface, which is constant spatially and oscillates in time with frequency ω. A second important assumption is proposed that the antenna wire is assumed to be infinitely thin [55, 59] and located at the position $r = r_a$. Hence, Eq. 3.44 for the current density is expressed as

$$\boldsymbol{j}_a(\boldsymbol{r}, t) = I_a \delta(r - r_a) \left[\mathbf{1}_z s_z(\theta, z) + \mathbf{1}_\theta s_\theta(\theta, z)\right] \exp(-i\omega t) \tag{4.1}$$

where δ presents the Dirac delta function. This 'zero-thickness antenna limit' is extensively used in 1D model [55, 59, 70, 104]. This assumption is beneficial to simplify equations and obtain a reasonable solution within the plasma. The weakness of this approach is that some wave fields are divergent in the position of antenna because of the singularity, and the antenna reactance cannot be obtained correctly [66, 108]. Meanwhile, some papers consider the thickness of antenna wires [89, 109] using different method and obtain a reasonable reactance.

In the zero-thickness limit, the physical domain is naturally divided in three subregions: the plasma region $0 < r < r_p$, the inner vacuum region $r_p < r < r_a$ and the outer vacuum region $r_a < r < r_w$.

Then, the governed wave equations are normalized in order to simply the equation system. Introducing the dimensionless variables

$$\hat{k}_l = \frac{k_z c}{\omega} = \frac{l\pi c}{L\omega}, \quad \hat{r} = \frac{r\omega}{c}, \quad \hat{\boldsymbol{B}} = \frac{\boldsymbol{B} r_a}{\mu_0 I_a}, \quad \hat{\boldsymbol{E}} = \frac{\boldsymbol{E} r_a}{\mu_0 I_a c}, \quad \hat{\boldsymbol{j_a}} = \frac{\boldsymbol{j_a} r_a c}{I_a \omega}$$

and phase modified fields

$$E_\phi = -iE_\theta, \qquad B_\phi = iB_\theta$$

Eq. 3.59-3.64 can be rearranged into the four differential equations, for each (l, m) mode

$$\frac{d\hat{E}_\phi}{d\hat{r}} = \left(\frac{\kappa_2 m}{\kappa_1 \hat{r}} - \frac{1}{\hat{r}}\right)\hat{E}_\phi + \frac{\hat{k}_l m}{\kappa_1 \hat{r}}\hat{B}_\phi + \left(1 - \frac{m^2}{\hat{r}^2 \kappa_1}\right)\hat{B}_z, \tag{4.2}$$

$$\frac{d\hat{E}_z}{d\hat{r}} = \frac{\kappa_2 \hat{k}_l}{\kappa_1}\hat{E}_\phi + \left(\frac{\hat{k}_l^2}{\kappa_1} - 1\right)\hat{B}_\phi - \frac{\hat{k}_l m}{\kappa_1 \hat{r}}\hat{B}_z, \tag{4.3}$$

$$\frac{d\hat{B}_\phi}{d\hat{r}} = \frac{m\hat{k}_l}{\hat{r}}\hat{E}_\phi + \left(\kappa_3 - \frac{m^2}{r^2}\right)\hat{E}_z - \frac{1}{\hat{r}}\hat{B}_\phi, \tag{4.4}$$

$$\frac{d\hat{B}_z}{d\hat{r}} = \left(\frac{\kappa_2^2}{\kappa_1} + \hat{k}_l^2 - \kappa_1\right)\hat{E}_\phi - \frac{m\hat{k}_l}{\hat{r}}\hat{E}_z + \frac{\kappa_2 \hat{k}_l}{\kappa_1}\hat{B}_\phi - \frac{\kappa_2 m}{\kappa_1 \hat{r}}\hat{B}_z \tag{4.5}$$

and the two algebraic equations:

$$\hat{E}_r = \frac{\kappa_2}{\kappa_1}\hat{E}_\phi + \frac{\hat{k}_l}{\kappa_1}\hat{B}_\phi - \frac{m}{\hat{r}\kappa_1}\hat{B}_z, \tag{4.6}$$

$$\hat{B}_r = \frac{m}{\hat{r}}\hat{E}_z - \hat{k}_l \hat{E}_\phi \tag{4.7}$$

These equations are completed with the jump conditions across the antenna surface $r = r_a$, continuity conditions at $r = r_p$, and the previously mentioned conditions at conducting walls.

4.1.1. Analytical solution for uniform plasma density

In the general case of the plasma density n_0 (or the applied field B_0) varying radially, the differential equation system must be treated numerically. Here and in next chapter we focus on the case of a uniform plasma column with a uniform magnetic field, when the dielectric functions in Eq. 4.2-4.7 are constant. Then, these equations admit also the analytical solution within the plasma in terms of Bessel functions [55, 59].

In order to obtain the analytical solution, the EM fields $\hat{E}_\phi$ and $\hat{B}_\phi$ have been expressed in terms of ($\hat{E}_z$, $\hat{B}_z$) and their derivatives ($\hat{E}'_z$, $\hat{B}'_z$) from Eq. 4.2-4.7 as follows

$$\hat{E}_\phi = \left(\delta^2 - \frac{\alpha\beta}{\kappa_3}\right)^{-1}\left[\delta\hat{E}'_z + \frac{\beta}{\kappa_3}\hat{B}'_z + \frac{\eta\beta}{\kappa_3}\hat{E}_z + \left(\frac{\delta\eta}{\kappa_1} + \frac{\zeta\beta}{\kappa_3}\right)\hat{B}_z\right], \tag{4.8}$$

$$\hat{B}_\phi = \left(\delta^2 - \frac{\alpha\beta}{\kappa_3}\right)^{-1}\left[\alpha\hat{E}'_z + \delta\hat{B}'_z + \eta\delta\hat{E}_z + \left(\frac{\alpha\eta}{\kappa_1} + \delta\zeta\right)\hat{B}_z\right] \tag{4.9}$$

where

$$\alpha = \kappa_1 - \frac{\kappa_2^2}{\kappa_1} - \hat{k}_l^2, \quad \beta = \kappa_3\left(1 - \frac{\hat{k}_l^2}{\kappa_1}\right), \quad \delta = \frac{\hat{k}_l \kappa_2}{\kappa_1}$$

and

$$\eta = \frac{\hat{k}_l m}{\hat{r}}, \qquad \zeta = \frac{\kappa_2 m}{\kappa_1 \hat{r}}$$

Substituting now $\hat{E}_\phi$ and $\hat{B}_\phi$ into Maxwell equations one has

$$\hat{E}_z'' + \frac{1}{\hat{r}}\hat{E}_z' + \left(\beta - \frac{m^2}{\hat{r}^2}\right)\hat{E}_z = \delta\hat{B}_z \tag{4.10}$$

$$\hat{B}_z'' + \frac{1}{\hat{r}}\hat{B}_z' + \left(\alpha - \frac{m^2}{\hat{r}^2}\right)\hat{B}_z = \kappa_3\delta\hat{E}_z \tag{4.11}$$

Defining the Bessel operator [55]

$$\hat{L} = \frac{1}{\hat{r}}\frac{\partial}{\partial\hat{r}}\left(\hat{r}\frac{\partial}{\partial\hat{r}}\right) - \frac{m^2}{\hat{r}^2}$$

Eq. (4.10-4.11) can be combined into

$$\left[\left(\hat{L}+\alpha\right)\left(\hat{L}+\beta\right) - \kappa_3\delta^2\right]\hat{B}_z \equiv \left(\hat{L}+N_1^2\right)\left(\hat{L}+N_2^2\right)\hat{B}_z = 0 \tag{4.12}$$

The same 4th order equation is also satisfied by $\hat{E}_z$ and $N_{1,2}$ here are the roots of the biquadratic equation

$$N^4 - (\alpha+\beta)N^2 + \alpha\beta - \kappa_3\delta^2 = 0 \tag{4.13}$$

and also $N_{1,2} = \hat{k}_\perp^\pm$ is the perpendicular wavenumber of two different kinds [55]. Thus, the solution of Eq. 4.12 is

$$\hat{B}_z = a_1 J_m\left(N_1\hat{r}\right) + a_2 J_m\left(N_2\hat{r}\right) \tag{4.14}$$

where J_m is the mth order Bessel function of first kind, a_1 and a_2 are constants determined by boundary conditions. As we know, the general solution for Eq. 4.12 should be the combination of J_m and Y_m functions [137]. Here, we only use the J_m function due to the boundary condition for $r = 0$. When $r = 0$, EM fields should be finite in the axis. However, Y_m function tends to be infinite at $r = 0$. Therefore, the Y_m functions are ruled out. Then, we rewrite the Eq. 4.12 in the form of

$$\left(\hat{L}+\alpha-\alpha+N_1^2\right)\left(\hat{L}+\alpha-\alpha+N_2^2\right)\hat{B}_z = 0 \tag{4.15}$$

and we consider the solution separately

$$\left(\hat{L}+\alpha\right)\hat{B}_z = \left(\alpha - N_1^2\right)\hat{B}_z \tag{4.16}$$

$$\left(\hat{L}+\alpha\right)\hat{B}_z = \left(\alpha - N_2^2\right)\hat{B}_z \tag{4.17}$$

Using Eq. 4.11, we obtain

$$\kappa_3 \delta \hat{E}_z = \left(\alpha - N_{1,2}^2\right) \hat{B}_z \tag{4.18}$$

Hence, the expression of $\hat{E}_z$ can be obtained

$$\hat{E}_z = a_1 \frac{\left(\alpha - N_1^2\right)}{\kappa_3 \delta} J_m\left(N_1 \hat{r}\right) + a_2 \frac{\left(\alpha - N_2^2\right)}{\kappa_3 \delta} J_m\left(N_2 \hat{r}\right). \tag{4.19}$$

In addition, the other components of field can be solved from Eq. 4.6-4.7 and 4.8-4.9 once $\hat{B}_z$ and $\hat{E}_z$ are calculated.

4.1.2. Analytical solution in vacuum

In this part, the analytical solution in vacuum is considered. In two vacuum regions the dielectric tensor reduces to $\bar{\bar{\epsilon}} = \epsilon_o \bar{\bar{I}}$, i.e. $\kappa_1 = \kappa_3 = 1$ and $\kappa_2 = 0$, and Maxwell equations are simplified to the well-known wave form [55, 59]

$$\hat{E}_z'' + \frac{1}{\hat{r}} \hat{E}_z' + \left(\kappa^2 - \frac{m^2}{\hat{r}^2}\right) \hat{E}_z = 0 \tag{4.20}$$

$$\hat{B}_z'' + \frac{1}{\hat{r}} \hat{B}_z' + \left(\kappa^2 - \frac{m^2}{\hat{r}^2}\right) \hat{B}_z = 0 \tag{4.21}$$

where $\kappa^2 = \hat{k}_l^2 - 1$. The general solution is of the form

$$\hat{B}_z = a_3 I_m\left(\kappa \hat{r}\right) + a_4 K_m\left(\kappa \hat{r}\right) \tag{4.22}$$

$$\hat{E}_z = a_5 I_m\left(\kappa \hat{r}\right) + a_6 K_m\left(\kappa \hat{r}\right) \tag{4.23}$$

where a_j are constants depending on the boundary condition. I_m and K_m are the modified Bessel functions of mth order.

4.1.3. Boundary and matching conditions

From previous analysis, the general solutions we have obtained for three spatial regions involve 10 coefficients (a_1-a_{10}). In order to determine them, the boundary conditions are imposed. First, at $r = r_w$, the electric field parallel to the conducting wall is zero:

$$\hat{E}_z\left(\hat{r}_w\right) = 0 \tag{4.24}$$

$$\hat{E}_\phi\left(\hat{r}_w\right) = 0 \tag{4.25}$$

Second, there is continuity of the EM fields across the plasma boundary,

$$\hat{E}_z\left(\hat{r}_p^+\right) - \hat{E}_z\left(\hat{r}_p^-\right) = 0 \tag{4.26}$$
$$\hat{E}_\phi\left(\hat{r}_p^+\right) - \hat{E}_\phi\left(\hat{r}_p^-\right) = 0 \tag{4.27}$$
$$\hat{B}_z\left(\hat{r}_p^+\right) - \hat{B}_z\left(\hat{r}_p^-\right) = 0 \tag{4.28}$$
$$\hat{B}_\phi\left(\hat{r}_p^+\right) - \hat{B}_\phi\left(\hat{r}_p^-\right) = 0 \tag{4.29}$$

Finally, at $r = r_a$, there is a current sheet generated by the antenna. Integrating directly Maxwell equations across the sheet, the jump in the parallel and azimuthal magnetic fields are [59]

$$\hat{E}_z\left(\hat{r}_a^+\right) - \hat{E}_z\left(\hat{r}_a^-\right) = 0 \tag{4.30}$$
$$\hat{E}_\phi\left(\hat{r}_a^+\right) - \hat{E}_\phi\left(\hat{r}_a^-\right) = 0 \tag{4.31}$$
$$\hat{B}_z\left(\hat{r}_a^+\right) - \hat{B}_z\left(\hat{r}_a^-\right) = -\hat{j}_{\theta a} \tag{4.32}$$
$$\hat{B}_\phi\left(\hat{r}_a^+\right) - \hat{B}_\phi\left(\hat{r}_a^-\right) = i\hat{j}_{za} \tag{4.33}$$

For each (l, m) mode, these ten boundary conditions constitute a set of 10 linear algebraic equations involving ten a_j's in terms of two antenna coefficients $\hat{j}_{\theta a}$ and $\hat{j}_{za}$. Solving that system, the (l, m) mode of the EM field in the whole domain $0 < r < r_w$ is the linear combination of two fundamental modes, proportional to $\hat{j}_{\theta a}$ and $\hat{j}_{za}$. Furthermore, since the current density along the antenna wire must satisfy the continuity equation [94]

$$\nabla \cdot \boldsymbol{j}_a = 0. \tag{4.34}$$

Taking into consideration the respective Fourier expansions for the azimuthal and axial components, the above equation yields a simple relation between the azimuthal and axial components of each (l, m) mode,

$$-\frac{m}{r_a} j_{\theta a}^{(l,m)} = i\frac{l\pi}{L} j_{za}^{(l,m)}, \quad i.e. \quad -\frac{m}{r_a} s_\theta^{(l,m)} = i\frac{l\pi}{L} s_z^{(l,m)} \tag{4.35}$$

With respect to parameters used for non-dimensionalization, the choice of I_a is quite obvious, while lengths c/ω and r_a have been chosen with the aim of reducing the number of parameters in the dimensionless equations, including the boundary conditions. However, it must be pointed out that there are rather different lengths in the problem. Typical ranges of variation would be

$$r_p, r_a \sim 1 - 5\text{cm}, \qquad r_w \sim 0.5 - 2\text{m} \qquad c/\omega \sim 2 - 50\text{m}. \tag{4.36}$$

As a consequence, with the choice we made, we have

1. $\hat{r}_p, \hat{r}_a \ll 1$, which must be taken into account for tolerances and accuracy, when integrating Maxwell equations numerically in the plasma region.
2. $\hat{r}_w < 1$, which implies that the oscillatory EM wave pattern does not develop fully inside the container, and the solution is going to be sensitive to the vessel size.

4.2. The Fourier transform of the antenna current

The geometry of the antenna current is central in deciding the main modes that are going to be excited inside plasmas. Two antenna families are going to be considered here: the double-saddle family and the helical family. The Nagoya III antenna, widely used in industrial applications, with two circle loops on either side connected by straight wires, is the common antenna shape of previous two families, thus providing a useful connection for a parametric study. Fig. 4.2 shows some of antennas of those families. The last two are helical antennas with half and one turns cases, $n = 0.5$ and $n = 1$. Because of their geometry, wave energy vectors for helcial antennas propagate mainly along the magnetic field [89].

(a) Nagoya III (b) Double saddle (c) Half-turn helical (d) 1-turn helical

FIGURE 4.2: Different types of antennas[70, 89, 94].

Due to the Eq. 3.57 and 3.57, three different Fourier expansions are going to be used for covering all the needed azimuthal and axial modes. These are:

$$f(\theta) = \sum_{m=-\infty}^{\infty} f^{(m)} e^{-im\theta}, \qquad f^{(m)} = \frac{1}{2\pi}\int_0^{2\pi} d\theta e^{im\theta} f(\theta) \tag{4.37}$$

$$f(z) = \sum_{l=1}^{\infty} f^{(l)} \sin k_l z, \qquad f^{(l)} = \frac{2}{L}\int_0^{L} dz \sin k_l z f(z) \tag{4.38}$$

$$f(z) = \frac{1}{L}\int_0^{L} dz f(z) + \sum_{l=1}^{\infty} f^{(l)} \cos k_l z, \qquad f^{(l)} = \frac{2}{L}\int_0^{L} dz \cos k_l z f(z), \tag{4.39}$$

We next apply these expansions to several functions. For the Dirac function, we have

$$\delta(\theta-\theta_0)=\sum_{m=-\infty}^{\infty}\frac{e^{im\theta_0}}{2\pi}e^{-im\theta} \tag{4.40}$$

$$\delta(z-z_0)=\sum_{l=1}^{\infty}\frac{2}{L}\sin k_l z_0 \sin k_l z \tag{4.41}$$

$$\delta(z-z_0)=\frac{1}{L}+\sum_{l=1}^{\infty}\frac{2}{L}\cos k_l z_0 \cos k_l z \tag{4.42}$$

For the Heaviside function $H(z-a)$, we have

$$H(\theta-\theta_0)=\sum_{m=-\infty}^{\infty}\frac{e^{im\theta_0}-1}{2\pi m}e^{-im\theta} \tag{4.43}$$

$$H(z-z_0)=2\sum_{l=1}^{\infty}\frac{\cos k_l z_0+(-1)^{l+1}}{\pi l}\sin k_l z \tag{4.44}$$

$$H(z-z_0)=\frac{L-z_0}{L}-2\sum_{l=1}^{\infty}\frac{\sin k_l z_0}{\pi l}\cos k_l z \tag{4.45}$$

The water-bag function

$$g(z;z_1,z_2)=H(z-z_1)-H(z-z_2)=\begin{cases}1, & z_1\le z\le z_2\\ 0, & \text{otherwise}\end{cases} \tag{4.46}$$

is going to be used for all antennas. Its cosine expansion is

$$g(z;z_1,z_2)=\frac{z_2-z_1}{L}+2\sum_{l=1}^{\infty}\frac{\sin k_l z_2-\sin k_l z_1}{\pi l}\cos k_l z \tag{4.47}$$

while the azimuthal expansion is

$$g(\theta;\theta_1,\theta_2)=\sum_{m=-\infty}^{\infty}\frac{e^{im\theta_2}-e^{im\theta_1}}{2\pi m}e^{-im\theta} \tag{4.48}$$

Next, based on the different geometry, the expression of current density for each type of antennas is discussed.

4.2.1. Nagoya III antenna

For the **Nagoya III antenna** shown in Fig. 4.2(a), the current shape functions can be written as

$$s_z(\theta, z) = g(z; z_1, z_2)\frac{\delta(\theta) - \delta(\theta - \pi)}{r_a} \tag{4.49}$$

$$s_\theta(\theta, z) = [\delta(z - z_1) - \delta(z - z_2)][g(\theta; \pi, 2\pi) - g(\theta; 0, \pi)] \tag{4.50}$$

where z_1 and z_2 represent the positions of two ends of antenna, respectively. It has the relation $z_{1,2} = z_a \mp L_a/2$, with the antenna length L_a and the center of antennas z_a. The two shape functions are expanded as Fourier double series

$$s_z(\theta, z) = \sum_{m=-\infty}^{\infty}\sum_{l=1}^{\infty} s_z^{(l,m)} e^{-im\theta}\cos k_l z, \tag{4.51}$$

$$s_\theta(\theta, z) = \sum_{m=-\infty}^{\infty}\sum_{l=1}^{\infty} s_\theta^{(l,m)} e^{-im\theta}\sin k_l z, \tag{4.52}$$

and the expression for each modes are obtained

$$s_z^{(l,m)} = \frac{4}{\pi^2 l r_a}\cos k_l\frac{z_1 + z_2}{2}\sin k_l\frac{z_1 - z_2}{2}, \quad l > 0 \tag{4.53}$$

$$s_z^{(0,m)} = \frac{2(z_2 - z_1)}{\pi L r_a} \tag{4.54}$$

Here, the m modes yield to be odd and the even m modes are zero. This also satisfies the double-saddle and helical antennas. Moreover, the component of azimuthal shape function s_θ satisfies Eq. 4.35 and can be easily obtained. Hence, For the cases below only the expression of s_z is given.

4.2.2. Double saddle antenna family

For a **double saddle antenna** with an azimuthal aperture $\theta_t \leq \pi$ shown in Fig. 4.2(b), which is first introduced by Boswell [29], the current shape functions are

$$\begin{aligned} s_z(\theta, z) = \frac{g(z; z_1, z_2)}{2r_a}[&\delta\left(\theta - \frac{\pi - \theta_t}{2}\right) - \delta\left(\theta - \frac{\pi + \theta_t}{2}\right) \\ &+ \delta\left(\theta + \frac{\pi - \theta_t}{2}\right) - \delta\left(\theta + \frac{\pi + \theta_t}{2}\right)] \end{aligned} \tag{4.55}$$

The corresponding Fourier expansion for $m =$ odd is

$$s_z^{(l,m)} = \frac{4}{\pi^2 l r_a} \cos k_l \frac{z_1 + z_2}{2} \sin k_l \frac{z_1 - z_2}{2} \sin\left(\frac{m\pi}{2}\right) \sin\left(\frac{m\theta_t}{2}\right) \tag{4.56}$$

$$s_z^{(0,m)} = \frac{2\,(z_2 - z_1)}{\pi L r_a} \sin\left(\frac{m\pi}{2}\right) \sin\left(\frac{m\theta_t}{2}\right) \tag{4.57}$$

The advantage of this antenna is that the antenna can be easily splitted around a cylindrical discharge tube without breaking the vacuum [18].

4.2.3. Helical antenna family

For an **helical antenna** with n turns shown in Fig. 4.2(c) and 4.2(d), the axial shape function is

$$s_z\,(\theta, z) = \frac{g(z; z_1, z_2)}{r_a} \left[\delta\left(\theta - \theta_w(z)\right) - \delta\left(\theta - \theta_w(z) - \pi\right)\right]. \tag{4.58}$$

where:

$$\theta_w(z) = 2\pi n \frac{z - z_1}{z_2 - z_1}$$

is the azimuthal angle along one of the helix wires. Also we define the helical angle as

$$\beta = \arctan 2\pi n \frac{r_a}{z_2 - z_1}$$

Hence, the Fourier transform is

$$\begin{aligned} s_z^{(l,m)} &= \frac{2\cos\beta}{\pi L\left(m^2 \sin^2\beta - (k_l r_a)^2 \cos^2\beta\right)} \times \\ &[im \sin\beta (e^{-2imn\pi} \cos k_l z_2 - \cos k_l z_1) - k_l r_a \cos\beta (e^{-2imn\pi} \sin k_l z_2 - \sin k_l z_1)] \end{aligned} \tag{4.59}$$

This can be expressed as

$$s_z^{(l,m)} = \frac{2}{\pi L} \frac{im \tan\beta (e^{-2imn\pi} \cos k_l z_2 - \cos k_l z_1) - k_l r_a (e^{-2imn\pi} \sin k_l z_2 - \sin k_l z_1)}{m^2 \tan^2\beta - (k_l r_a)^2} \tag{4.60}$$

$$s_z^{(0,m)} = \frac{i\,(z_2 - z_1)}{\pi^2 L m n r_a} \left[e^{-2imn\pi} - 1\right] \tag{4.61}$$

which recovers the Nagoya III antenna expression for $n = 0$. For all antennas, only odd m modes ($m = \pm 1, \pm 3, \pm 5 \ldots$) are excited in terms of Fourier transform.

4.3. Nominal simulation case

In order to discuss the truncation of Fourier series, a particular design of 15kW HPT [133], which is also applied in the parametric investigation with the purpose of optimising the thruster, are used as the input data. The gas is argon, the radially uniform plasma and axial static magnetic field are considered. The main parameters are summarized in Tab. 4.1. These parameters are used in all the calculations of modes discussion and parametric investigations, except for the one whose variation is being studied.

Parameter		**Value**
r_p	Plasma radius	$0.0735m$
L	Plasma and cage axial length	$5r_p$
r_w	External cage radius	$2r_p$
B_0	Applied magnetic field	$450G$
T_e	Plasma temperature	$20eV$
n_0	Plasma density	$5.6 \times 10^{18} m^{-3}$
ν_e	Electron collision frequency	$3.26MHz$
f_{RF}	Frequency of the RF emission	$13.56MHz$
r_a	Antenna loop radius	$1.05r_p$
$L_a = 2a$	Antenna axial length	$L/2$
z_a	Antenna symmetry plane	$L/2$

TABLE 4.1: Summary of input data for the plasma-wave interaction simulations.

4.4. The truncation of the Fourier double series

The 1D radial model is based on the Fourier expansion in axial and azimuthal directions. A specific number of (l, m) modes are used in the calculations and the simulation time increases with the number of (l, m) modes. Thus, in this part, for each type of antenna, the influence of different numbers of (l, m) modes on the resistance is discussed in order to choose the appropriate number of modes which yields to a good accuracy of results with a reasonable simulation time.

For the nominal case of Tab. 4.1, a large number of (l, m) modes with $m = [-151, 151]$ and $l = [0, 200]$ are taken into account as a standard in calculating the total resistance. For all the antennas, the modes which make the current density zero are ruled out. In addition, in order to evaluate both the azimuthal and axial component, it is convenient to define the 'norm' of the current density as

$$j_n^{(l,m)} = \sqrt{\left|j_z^{(l,m)}\right|^2 + \left|j_\theta^{(l,m)}\right|^2} \tag{4.62}$$

This expression is used to evaluate the contribution of each mode to the total current.

4.4.1. Nagoya III antenna

The contribution of each (l, m) mode to the resistance and current density for the Nagoya III antenna is shown in Fig. 4.3. As we see, with the increase of (l, m) modes, the contribution to the resistance decreases gradually. And the maximum individual contribution to the resistance is for $l = 2$ and $m = -1$. This is consistent with the result of current density. It makes sense because from Eq. 4.53 and Eq. 4.35, the azimuthal current density j_θ is proportional to $1/m$ and the axial current density j_z is proportional to $1/l$ for Nagoya III antennas. Therefore, for a fixed current I_a, a larger current density can be obtained when l and m are small and it leads to a large contribution to the total resistance. In addition, the behaviour of the $l = 2$ profile illustrates that the wave propagation for m modes is not symmetric.

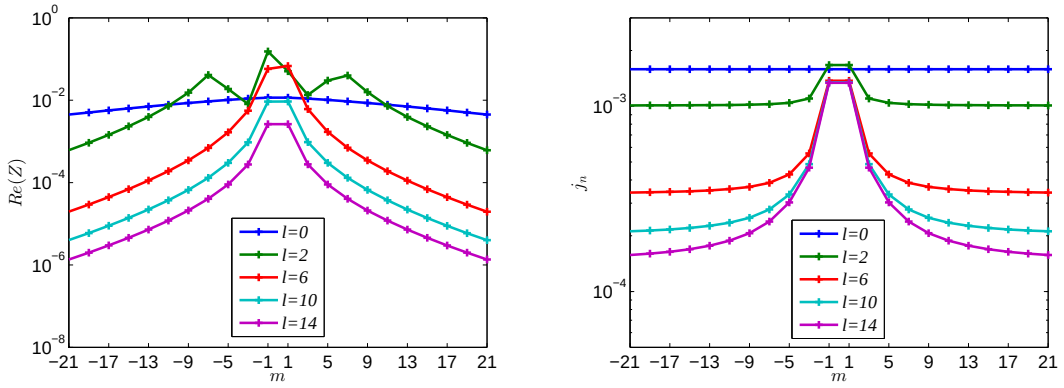

(a) Resistance (b) Current density

FIGURE 4.3: The contribution of each (l, m) mode to the resistance and current density in Nagoya III type of antennas.

In Fig. 4.4, the plasma resistance $R = Re(Z)$, obtained from truncation of the different ranges of (l, m) modes is investigated. The results show that the resistance reaches convergence at 3.515 ohm when (l_n, m_n) are up to $(30, 35)$; the influence of number of (l, m) modes on $Re(Z)$ can be neglected if the number is beyond it. Hence, for Nagoya III antennas, the ranges $l = [0, 30]$ and $m = [-35, 35]$ are selected for the calculations.

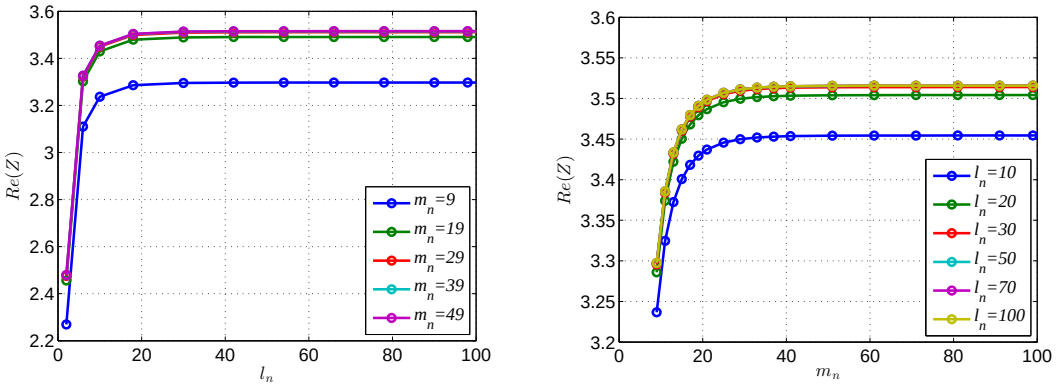

(a) Resistance with (l_n, m_n) (b) Resistance with (m_n, l_n)

FIGURE 4.4: The resistance $Re(Z)$ for different number of (l, m) modes in Nagoya III case. Figure in left side is $Re(Z)$ varying with l_n for different m_n, the right side is opposite. l_n and m_n mean the number of (l, m) modes, respectively. For example,$l_n = 200$ means $l = [0, 200]$ is selected, $m_n = 9$ means $m = [-9, 9]$ is selected.

4.4.2. Double saddle family

In the case of the double saddle coil antenna, the case $\theta_t = \pi/2$ is selected. The results for the contribution of each (l, m) mode are shown in Fig. 4.5. The variation is similar with Nagoya III type of antenna because of the similar geometry. The maximum contribution to the resistance is achieved when $l = 2$ and $m = -1$.

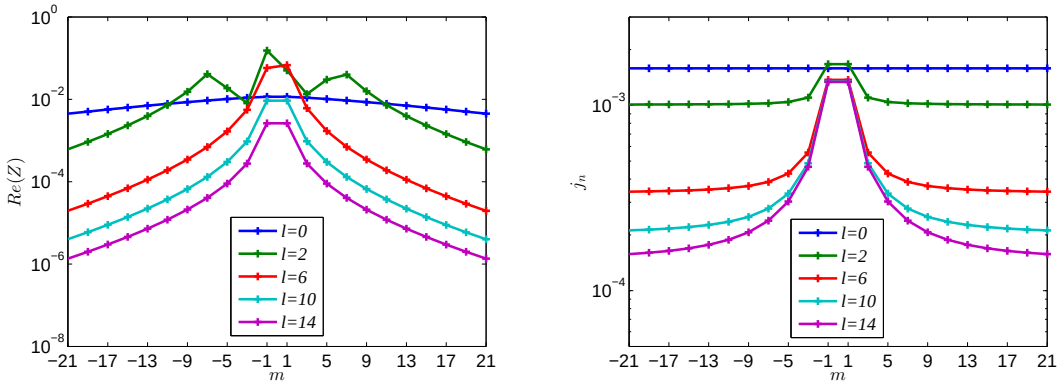

(a) Resistance (b) Current density

FIGURE 4.5: The contribution of each (l, m) mode to the resistance and current density in double saddle coil antennas. The extended angle $\theta_t = \pi/2$.

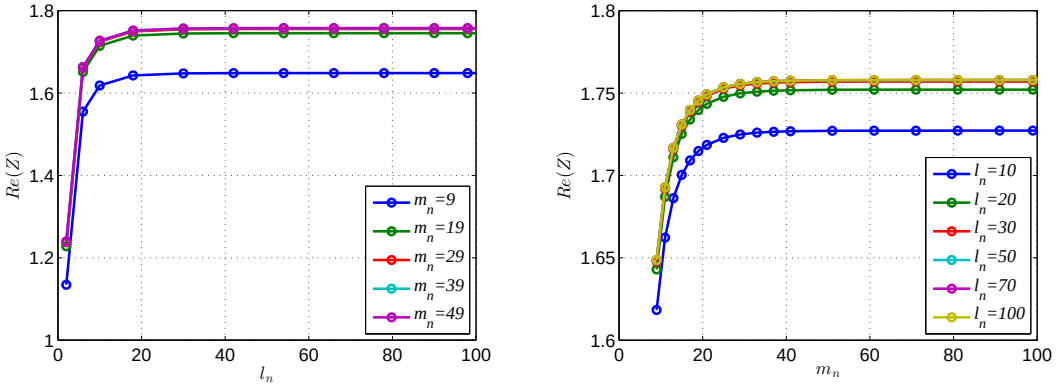

(a) Resistance with (l_n, m_n)

(b) Resistance with (m_n, l_n)

FIGURE 4.6: The resistance $Re(Z)$ for different number of (l, m) modes in double saddle coil antenna case. Figure in left side is $Re(Z)$ varying with l_n for different m_n, the right side is opposite. l_n and m_n mean the number of (l, m) modes, respectively. For example, $l_n = 200$ means $l = [0, 200]$ is selected, $m_n = 9$ means $m = [-9, 9]$ is selected.

The convergence profiles of (l, m) modes are shown in Fig. 4.6. The range for truncating the series is $(l_n, m_n) = (30, 35)$. Notice that the resistance is 1.76 ohm, which is twice lower than the Nagoya III antenna case. Tab. 4.2 shows the contribution of j_θ and j_z to the resistance, respectively. As we see, the contribution of j_θ is higher than j_z in both cases and the percentage for double saddle coil antenna and Nagoya III is the same. That means the azimuthal component of current density is the main part and the arc angle influences not only the azimuthal component j_θ, but also the axial component j_z. It also can be checked from Eq. 4.56.

Antenna type	**Contribution of j_θ**		**Contribution of j_z**		**Total $Re(Z)$**
	$Re(Z)[\Omega]$	Percentage	$Re(Z)[\Omega]$	Percentage	$[\Omega]$
Double saddle	1.05	60%	0.71	40%	1.760
Nagoya III	2.106	60%	1.409	40%	3.515

TABLE 4.2: The contribution of each component of current density to the resistance for double saddle coil and Nagoya III antennas.

4.4.3. Helical antenna family

In the discussion of helical antennas, different helix turns are taken into account. In Fig. 4.7, the contribution of each mode for the half-turn helical antenna is described. The maximum contribution comes from $(l, m) = (3, -1)$. Compared with the Nagoya III and double saddle coil antennas, the contributions to resistance concentrate in the range of $m = (-9, 9)$. The convergence profiles in Fig. 4.8 illustrate this conclusion. Thus, the

number of modes to be used in the calculation for the half-turn helical antenna is up to $(l_n, m_n) = (30, 13)$.

The plasma resistance for the half-turn helical antenna is 7.4 ohm, which doubles the resistance of the Nagoya III antenna.

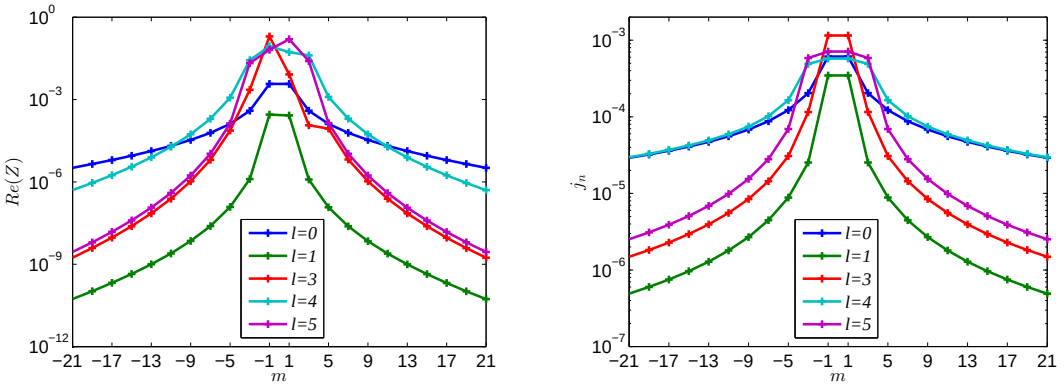

(a) Resistance (b) Current density

FIGURE 4.7: The contribution of each (l,m) mode to the resistance and the norm of current density for half-turn helical antennas.

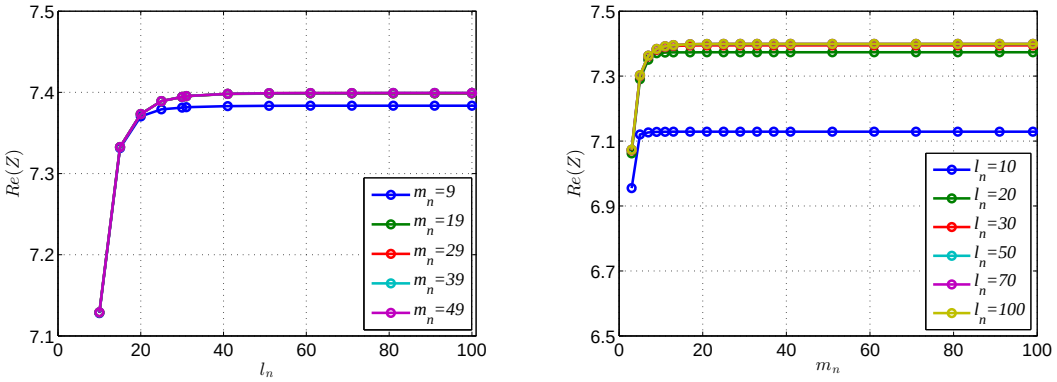

(a) Resistance with (l_n, m_n) (b) Resistance with (m_n, l_n)

FIGURE 4.8: The resistance $Re(Z)$ for different number of (l, m) modes in half turn helical antenna case. Figure in left side is $Re(Z)$ varying with l_n for different m_n, the right side is opposite. l_n and m_n mean the number of (l, m) modes, respectively. For example, $l_n = 200$ means $l = [0, 200]$ is selected, $m_n = 9$ means $m = [-9, 9]$ is selected.

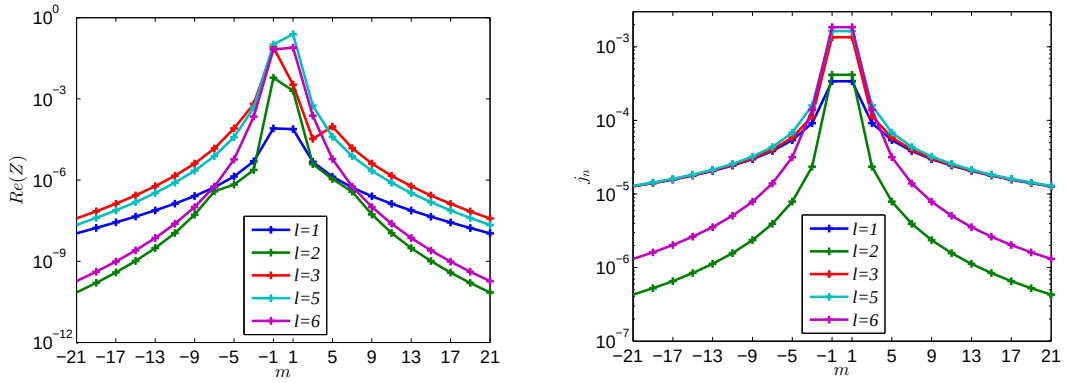

(a) Resistance (b) Current density

FIGURE 4.9: The contribution of each (l,m) mode to the resistance and the norm of current density for 1-turn helical antennas.

For the one-turn helical antenna, the maximum contribution to the resistance comes from $(l, m) = (5, 1)$, as shown in Fig. 4.9, which differs slightly with the maximum contribution to the current density at $(l, m) = (6, \pm 1)$. The similar phenomenon comes out in the case of the two-turn helical antenna in Fig. 4.11, the current density at $(l, m) = (6, \pm 1)$ is higher than $(l, m) = (5, \pm 1)$, however, the contribution to the resistance at $(l, m) = (6, \pm 1)$ is almost equal to $(l, m) = (5, \pm 1)$. Because of the different parallel wavenumber they have for $l = 5$ and $l = 6$, the condition of wave propagation should be taken into account as the reason for the difference. We will discuss this in detail in next chapter.

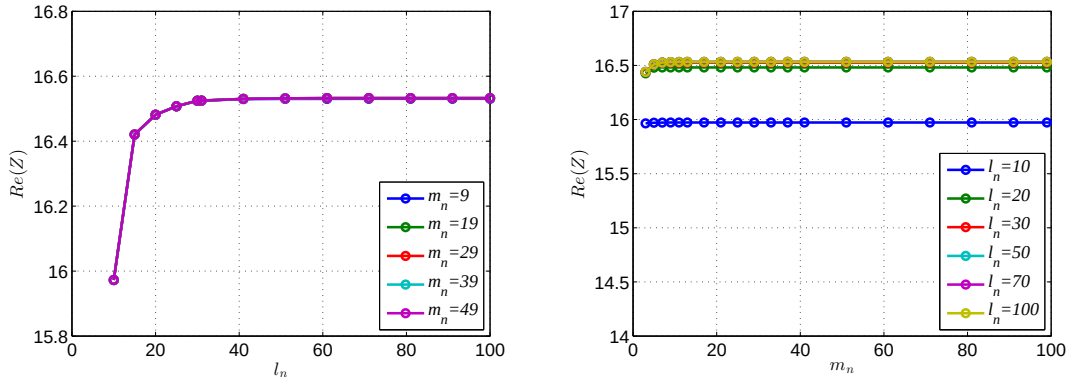

(a) Resistance with (l_n, m_n) (b) Resistance with (m_n, l_n)

FIGURE 4.10: The resistance $Re(Z)$ for different number of (l, m) modes in 1-turn helical antenna case. Figure in left side is $Re(Z)$ varying with l_n for different m_n, the right side is opposite. l_n and m_n mean the number of (l, m) modes, respectively. For example, $l_n = 200$ means $l = [0, 200]$ is selected, $m_n = 9$ means $m = [-9, 9]$ is selected.

From Fig. 4.10 and Fig. 4.12, the series for resistance reaches convergence fast in the range of m modes. Comparing this two Figures with half-turn helical antenna case and Nagoya III antenna case, fewer m modes need to be considered as the number of antenna turns increases. And this conclusion can be extended to helical antennas with more turns. Hence, $(l_n, m_n) = (30, 11)$ and $(40, 9)$ can be chosen for the one-turn and two-turn helical antenna cases, respectively. Fig. 4.13 and Fig. 4.14 shows the results of the three-turn helical antenna case, in which up to $(l_n, m_n) = (40, 9)$ modes are used.

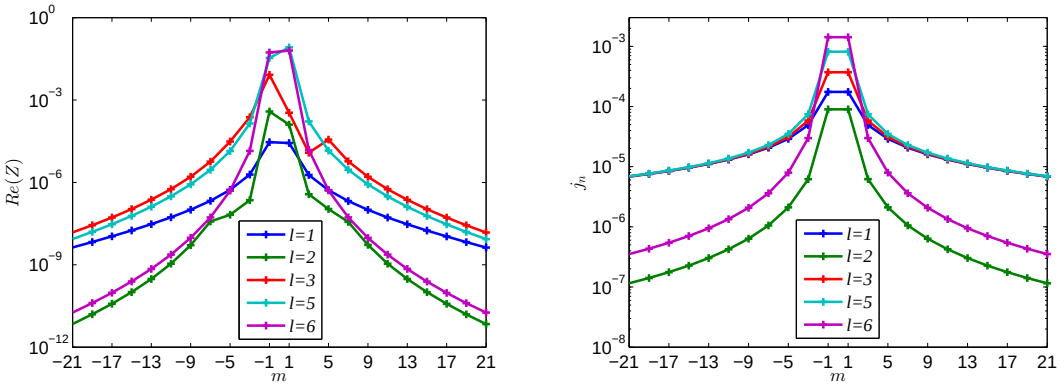

(a) Resistance (b) Current density

FIGURE 4.11: The contribution of each (l, m) mode to the resistance and the norm of current density for 2-turn helical antennas.

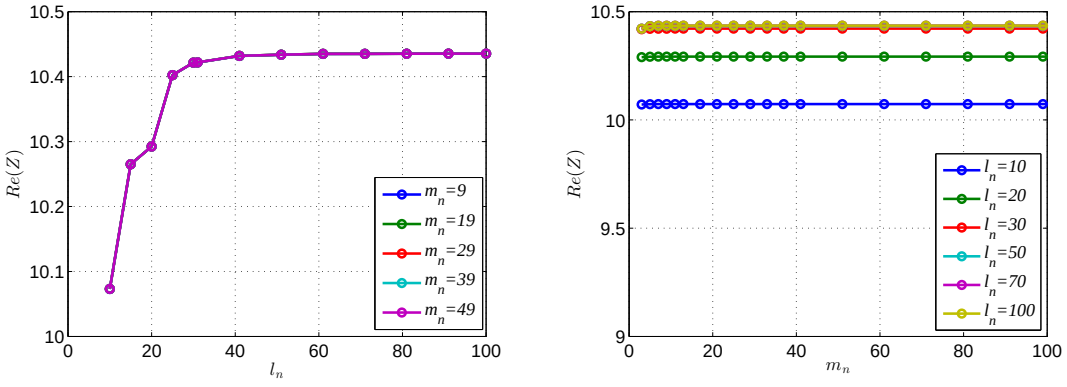

(a) Resistance with (l_n, m_n) (b) Resistance with (m_n, l_n)

FIGURE 4.12: The resistance $Re(Z)$ for different number of (l, m) modes in 2-turn helical antenna case. Figure in left side is $Re(Z)$ varying with l_n for different m_n, the right side is opposite. l_n and m_n mean the number of (l, m) modes, respectively. For example, $l_n = 200$ means $l = [0, 200]$ is selected, $m_n = 9$ means $m = [-9, 9]$ is selected.

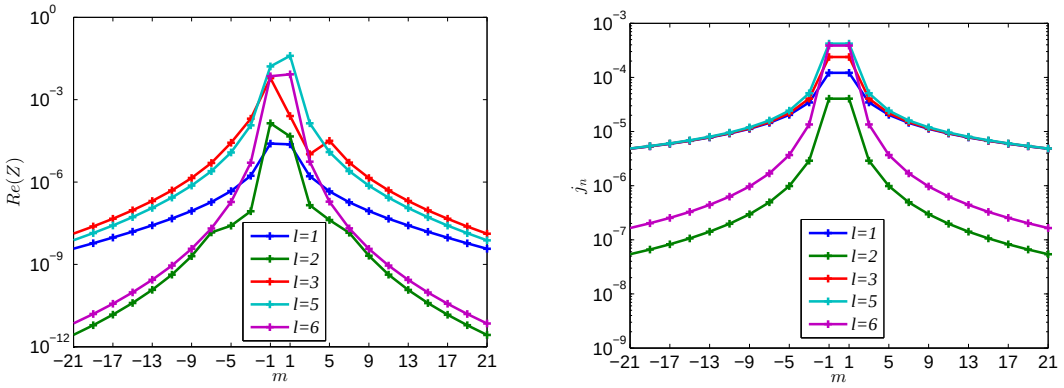

(a) Resistance (b) Current density

FIGURE 4.13: The contribution of each (l, m) mode to the resistance and the norm of current density for 3-turn helical antennas.

Comparing the resistance for the different helical antennas, the one-turn case, with 16.53 ohm, has the maximum resistance of the cases studied here. Plasma resistance lowers to 10.43 ohm for the two-turn antenna and to 5.3 ohm for the three-turn antenna. We will see later that this is not intrinsic to these high-turn antennas but caused by the axial length of antenna we have used.

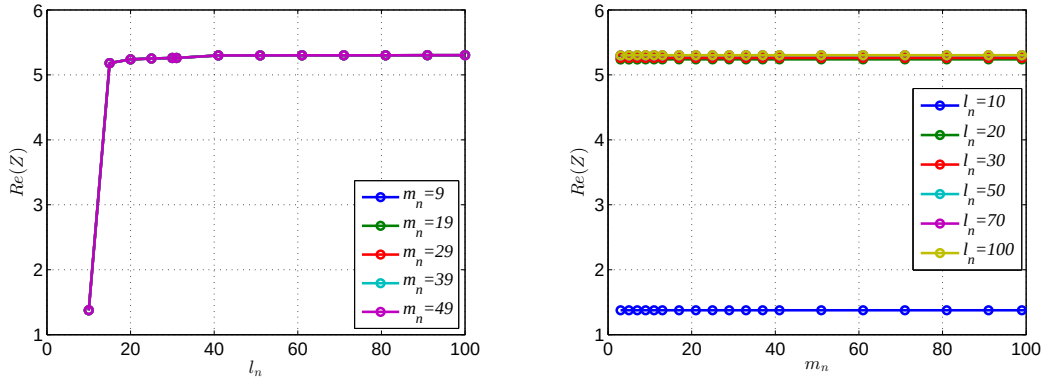

(a) Resistance with (l_n, m_n) (b) Resistance with (m_n, l_n)

FIGURE 4.14: The resistance $Re(Z)$ for different number of (l, m) modes in 3-turn helical antenna case. Figure in left side is $Re(Z)$ varying with l_n for different m_n, the right side is opposite. l_n and m_n mean the number of (l, m) modes, respectively. For example, $l_n = 200$ means $l = [0, 200]$ is selected, $m_n = 9$ means $m = [-9, 9]$ is selected.

4.4.4. Summary for the modes truncation

The influence of number of (l, m) modes on the resistance with different types of antennas was analysed in order to compute accurately the plasma resistance. The contribution of each mode is strongly related with the corresponding current density mode. For all

the antennas, the resistance series reach convergence with varying numbers of (l, m) modes. With the turns of helical antennas increasing, the number of m modes required is smaller. The suggested ranges of modes are summarized in Tab. 4.3.

For a fixed antenna geometry with an axial length half of the plasma column length and placed symmetrically at the mid-plane, Tab. 4.3 also shows that within the double saddle family, the resistance increases with the arcs of the antenna loops and thus the largest resistance is achieved when this topology converges to the Nagoya III antenna geometry (arc angle = π). Then, for the helical family, it is found that the resistance increases with the number of turns n, until $n = 2$ and then the resistance decreases. The reason of decrease will be explained in next chapter, it is related to the length of plasma column.

Antenna type	$(\boldsymbol{l_n, m_n})$	$\boldsymbol{Re(Z)}[\Omega]$
Double saddle	$(30, 35)$	1.76
Nagoya III	$(30, 35)$	3.52
Half-turn helical	$(30, 13)$	7.40
1 turn helical	$(30, 11)$	16.53
2 turn helical	$(40, 9)$	10.44
3 turn helical	$(40, 9)$	5.30

TABLE 4.3: The number of computed (l, m) modes and the resulting plasma resistance in nominal case. The l_n and m_n mean the number of (l, m) modes, respectively. For example, $l_n = 40$ means $l = [0, 40]$ is selected, $m_n = 9$ means $m = [-9, 9]$ is selected.

Chapter 5

Parametric Investigation of Helicon Sources

In order to optimize the overall efficiency of the helicon source, a complete parametric investigation is carried out in this chapter. The studies of mode truncation for different kinds of antennas have been done in Chapter 4 to find out the appropriate number of modes to keep in the analysis. Here, the influence of antenna type and antenna geometric parameters on the wave propagations are studied in the conventional frequency regime the and extended frequency regime mentioned in Chapter 3.

5.1. Influence of antenna geometrical parameters

Based on the previous discussion, the effect of the geometrical parameters for each antenna type, including double saddle family and helical family, are studied in this section. The geometrical parameters of antennas influence the plasma resistance with the variation of antenna current density.

5.1.1. Double saddle family

Considering the similarities, Nagoya III antenna is discussed in this section as a special double saddle coil antenna, which has an arc angle $\theta_t = \pi$. Fig. 5.1(a) describes the variation of resistance when the arc angle increases. It shows that a larger angle generally yields a larger resistance, so that Nagoya III antenna is the best case within the family of double saddle coil antennas.

In order to rule out the influence of θ_t on the other parameters, two cases when $\theta_t = \pi/2$ and $\theta_t = \pi$ (Nagoya III antenna) are discussed for the main geometrical parameters (z_a, L_a and r_a). From the expression of the current density in Eq. 4.56 and Eq. 4.62, the axial component j_z is inversely proportional to the radius r_a, and also the norm j_n increases when r_a decreases. Therefore, with the radius of antenna increasing, the resistance is reduced. The numerical results prove this prediction in Fig. 5.1(b), the resistance goes down varying with r_a for two antennas. It is demonstrated that the antenna-plasma coupling improves as the antenna approaches the plasma. In addition, when the antenna is near to the conducting wall ($r_a \approx 2r_p$), the resistance is almost zero. This is because the conducting wall produces an image current to cancel out the influence of the antenna when the antenna approaching it [100]. Thus, it is concluded that the radius of the antenna should be close to the plasma radius and away from the conducting chamber.

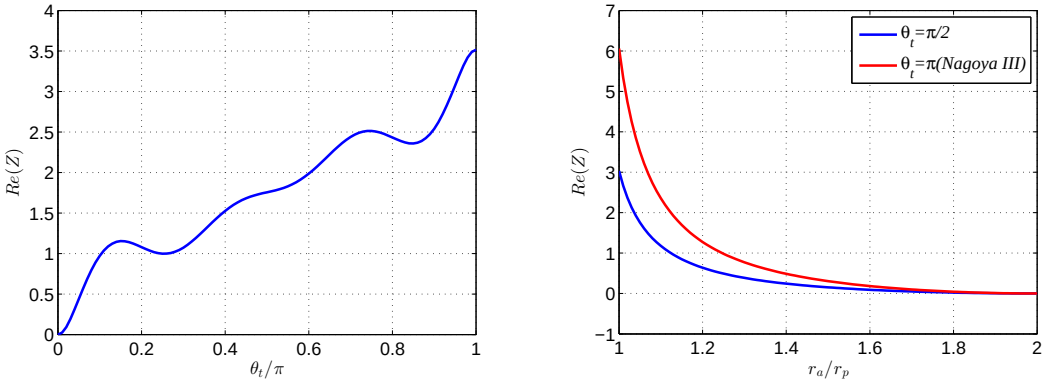

(a) Extend angle θ_t (b) Radius of antenna r_a

FIGURE 5.1: Resistance varying with the extend angle θ_t and antenna radius r_a for double saddle antenna family.

With the variation of z_a and L_a, the current density follows a sinusoidal function. It leads to a symmetric oscillation of resistance in Fig. 5.2. For both antennas, the maximum resistance takes place when $z_a = 0.41L$ or $0.59L$ for the fixed antenna axial length $L_a = L/2$. Similarly, with a fixed location $z_a = L/2$, maximum resistance is achieved when the antenna axial length is $0.26L$ or $0.74L$. Very interestingly, these results show that the optimum location and length of double-saddle antennas are independent of the arc angle θ_t.

The 2D colour maps considering both the variation of z_a and L_a are shown in Fig. 5.3. According to the model, the antenna axial length is restricted to the length of plasma column. With the variation of z_a and L_a, the current density follows the sine and cosine function. It leads to a symmetric oscillation of resistance. As we see, the maximum

resistance is 5.285Ω takes place when $L_a = 0.22L$ and $z_a = 0.22L$ or $0.78L$, and amounts to 5.29Ω for the Nagoya III antenna and half that value for the case $\theta_t = \pi/2$. It is further confirmed that the optimum location and length of double saddle antennas are independent of the arc angle θ_t.

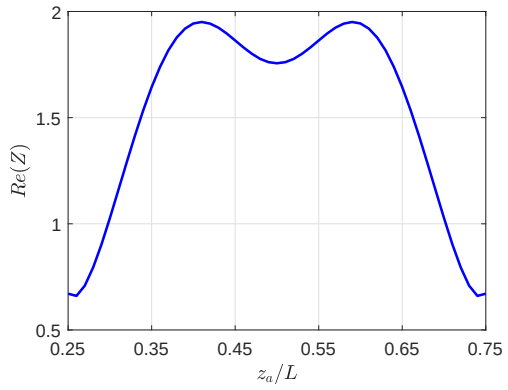

(a) Antenna location ($\theta_t = \pi/2$)

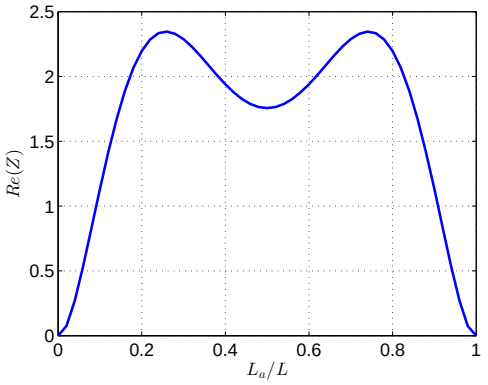

(b) Antenna length ($\theta_t = \pi/2$)

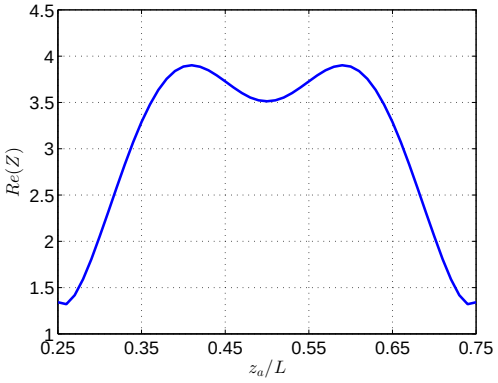

(c) Antenna location ($\theta_t = \pi$)

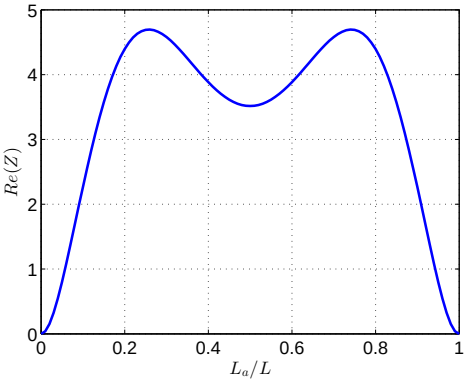

(d) Antenna length ($\theta_t = \pi$)

FIGURE 5.2: Plasma resistance versus the antenna center location z_a with a fixed antenna length $L_a = L/2$ (left) and versus the antenna axial length L_a with a fixed antenna location $z_a = L/2$ (right), for $\theta_t = \pi/2$ and $\theta_t = \pi$.

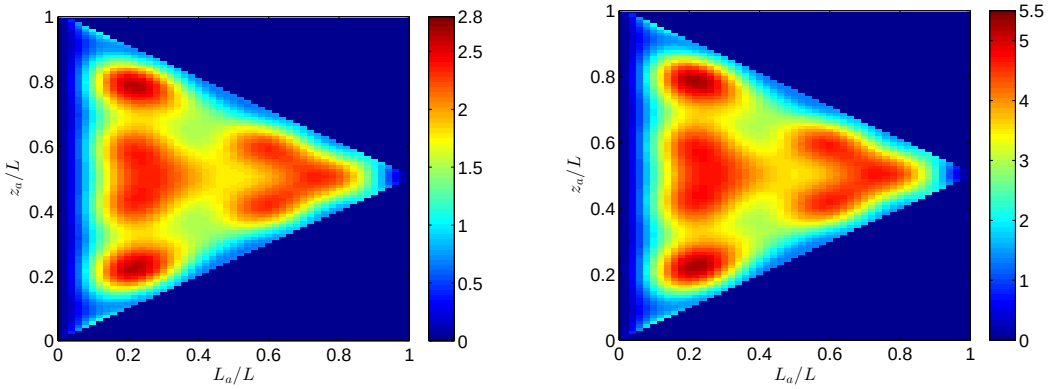

(a) $\theta_t = \pi/2$ (b) $\theta_t = \pi$

FIGURE 5.3: Resistance versus both the antenna location and the antenna length for $\theta_t = \pi/2$ and $\theta_t = \pi$.

5.1.2. Helical antenna family

In this section, the analysis of geometrical parameters for helical antenna series is discussed. The variations of the resistance with the antenna location and axial length for different number of turns are described in Fig. 5.4 and 5.5. As we see, resistance values oscillate with the antenna parameters. We observe that the influence of the symmetry plane z_a is weakened as the number of turns increase for fixed antenna length.

Observing the resistance profiles varying with the antenna axial length, the value of resistance is strongly related to L_a. For the half-turn helical antenna case, there are two peak values for the resistance and only one appears in one-turn and two-turn cases. With the number of turns increasing, the maximum resistance increases but requires a larger antenna axial length. This explains why for fixed antenna length, high-turn antennas do not yield large resistances: the antenna length is not optimized. The maximum resistance in the two-turn case is 41.1 ohm for $L_a = 0.88L$.

Similarly, the 2D contour map with both the variation of L_a and z_a are given in Fig. 5.6. It further illustrates that a higher resistance can be obtained with increasing the number of turns of helical antennas if the antenna length is increased.

The variation of the resistance with the relative antenna loop radius, for different helical antennas, is shown in Fig. 5.7. As before, with the double saddle antenna, plasma resistance is higher when the antenna is closer to the plasma boundary. The resistance is approximately proportional to $1/r_a$, and resistance becomes zero when $r_a = r_w$ since the conducting cage would short-circuit the antenna fields.

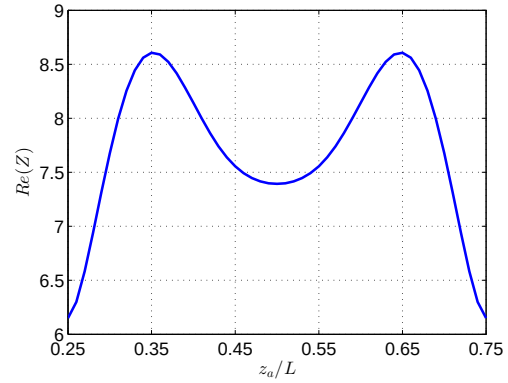

(a) Antenna location ($n = 0.5$)

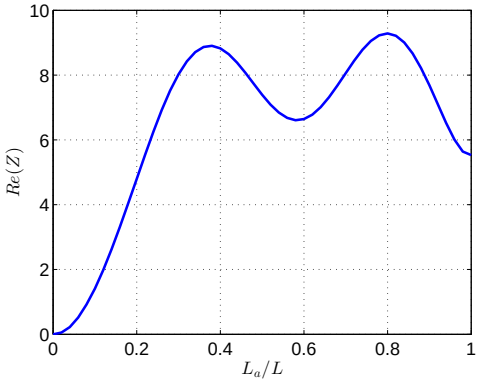

(b) Antenna length ($n = 0.5$)

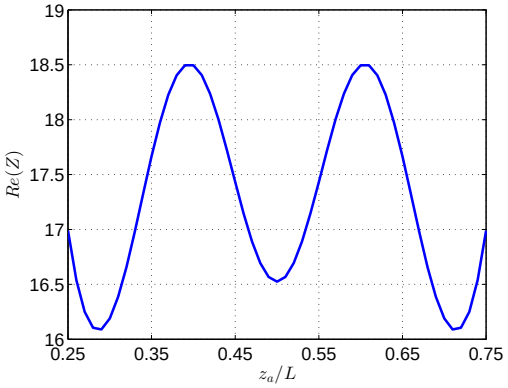

(c) Antenna location ($n = 1$)

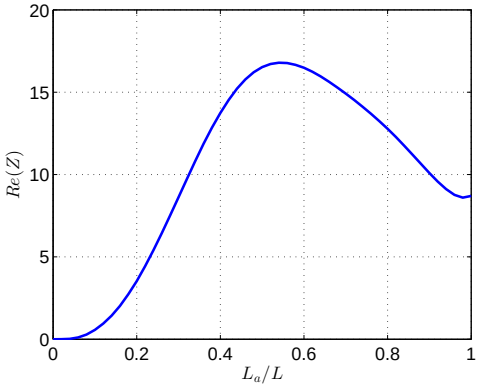

(d) Antenna length ($n = 1$)

FIGURE 5.4: Plasma resistance versus the antenna center location z_a and $L_a = L/2$ (left) and versus the antenna axial length L_a and $z_a = L/2$ (right), for half-turn and 1-turn helical antennas.

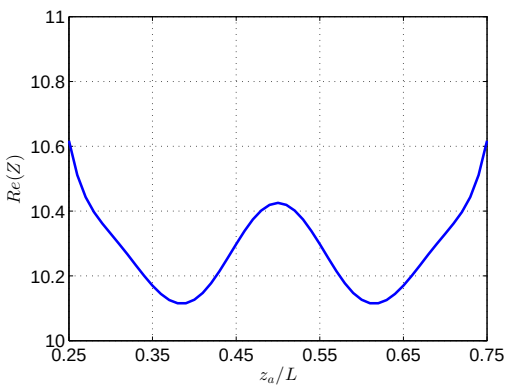

(a) Antenna location ($n = 2$)

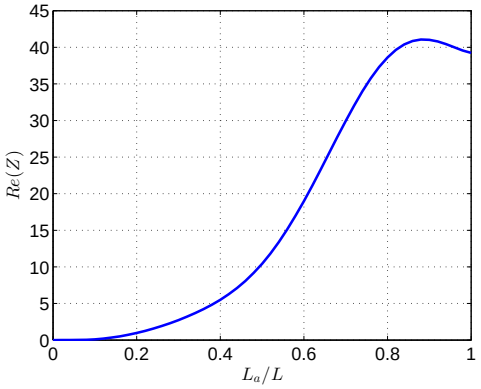

(b) Antenna length ($n = 2$)

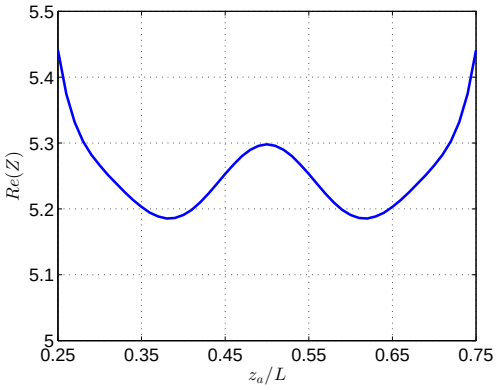

(c) Antenna location ($n = 3$)

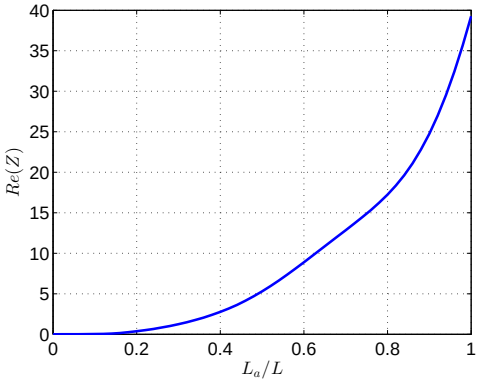

(d) Antenna length ($n = 3$)

FIGURE 5.5: Plasma resistance versus the antenna center location z_a and $L_a = L/2$ (left) and versus the antenna axial length L_a and $z_a = L/2$ (right), for 2-turn and 3-turn helical antennas.

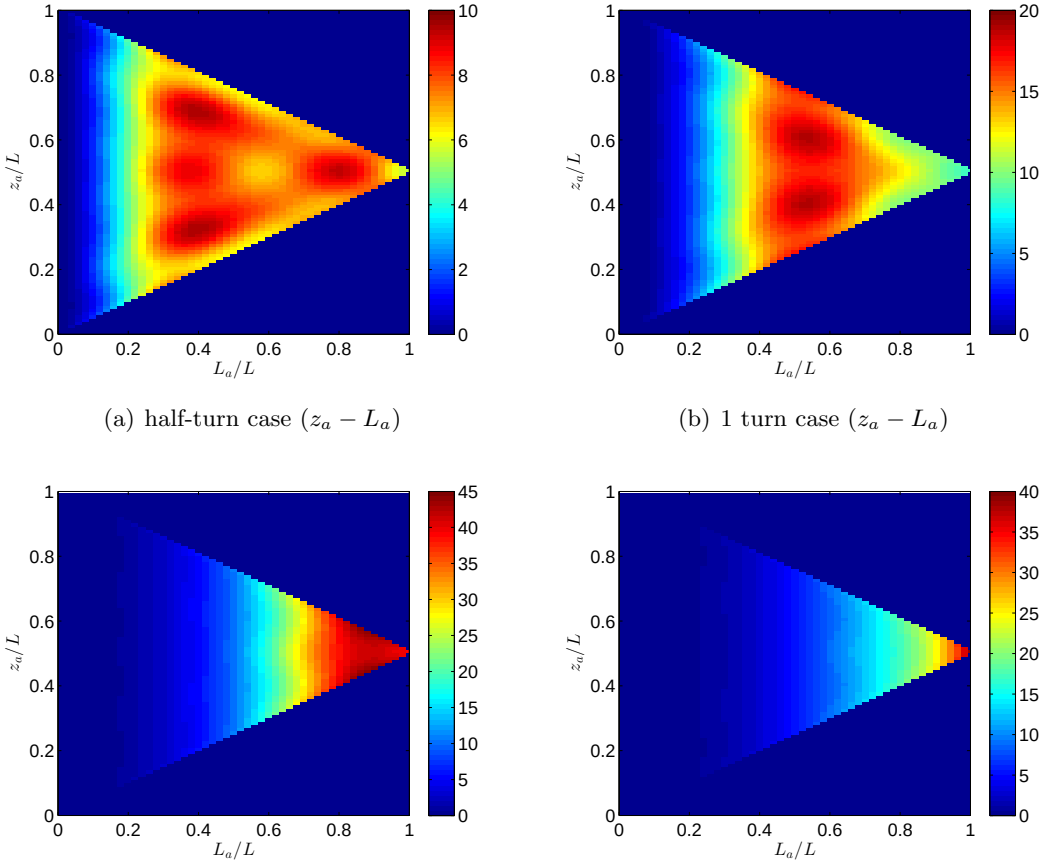

(a) half-turn case ($z_a - L_a$)

(b) 1 turn case ($z_a - L_a$)

(c) 2 turn case ($z_a - L_a$)

(d) 3 turn case ($z_a - L_a$)

FIGURE 5.6: Resistance versus both the antenna location and the antenna length for different number of turns.

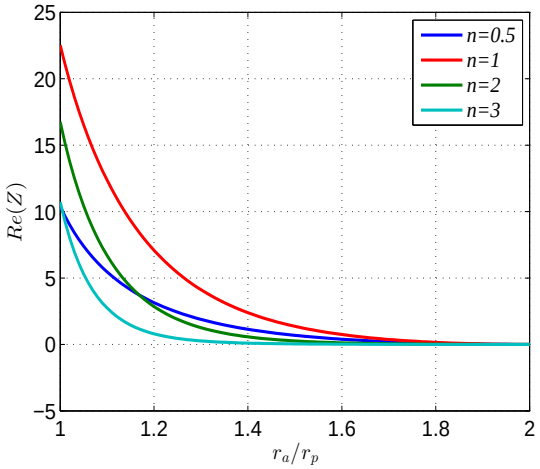

FIGURE 5.7: Resistance versus the antenna radius r_a for different number of turns.

5.2. Analysis of the high frequency regime

In this section, the analysis is restricted to frequencies much higher than the lower hybrid frequency. The wave propagation and parametric investigation are discussed in detail. Furthermore, the half-turn helical antenna, which has been widely used in practice, is applied in simulations. The selected antenna parameters are the optimal combination from previous results:

$$L_a = 0.4L, \quad z_a = L/3 \quad r_a = 1.05r_p. \tag{5.1}$$

5.2.1. Wave field and power deposition

Fig. 5.8, Fig. 5.9 and Fig. 5.10 illustrate the radial profiles of electromagnetic field in the three different regimes. Based on the nominal case, only the axial mode $l = 3$ is taken into account in order to illustrate the behaviour of the three regimes clearly; for m the range $[-13, 13]$ was considered. Changing the plasma density, the EM fields in different regimes are obtained.

At low plasma density $n_0 = 5.6\times10^{17}m^{-3}$, the parameters are in the surface wave regime, and only TG waves propagate. These are highly oscillating near the plasma boundary and damped out toward the center. It is clear that power deposition of TG mode concentrates in a narrow layer near the boundary region. At $n_0 = 5.6 \times 10^{18}m^{-3}$, the mode l=3 is in the DWR. Two kinds of waves are observed clearly in Fig. 5.9, the long-wavelength helicon wave and the short-wavelength TG wave. Near the boundary, the TG wave dominates the behaviour. Observing the profile of E_r, the amplitude becomes much higher near the boundary. It shows that the plasma flow will be influenced largely by the induced electric field in the region near the boundary.

When the plasma density is $n_0 = 5.6 \times 10^{19}m^{-3}$, the waves are in the ICR, and no wave propagates. Fig. 5.10 shows this phenomenon, the wave is damped out in most regions and the amplitude is very small. The radial distribution of power absorption for these three cases, which are shown in Fig. 5.11, also illustrates the features of these three regimes. The power absorption is very small in the ICR because no wave propagates. In the double wave regime, energy deposition occurs everywhere although it reaches a higher value near the boundary where the TG wave dominates. In Fig. 5.11(a), the profile proves that the energy deposition of TG wave concentrates near the boundary. Comparing the resistance of these three cases in Tab. 5.1, the resistance in the DWR case is larger than in the other cases. That means that operating in the DWR is beneficial for power deposition.

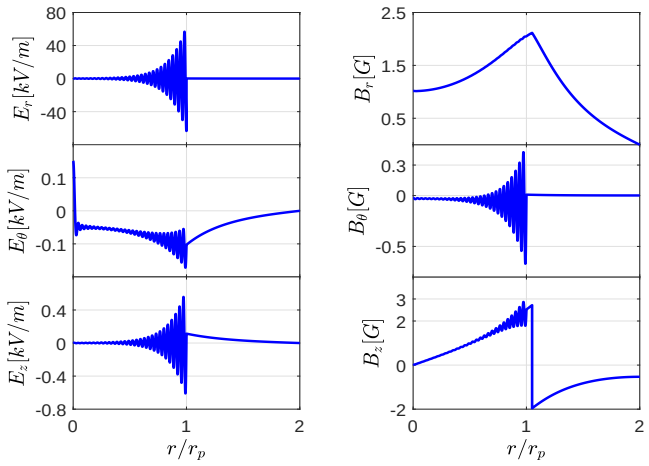

FIGURE 5.8: Radial profiles of electromagnetic fields at $\theta = 0$, $z = L/4$, $n_0 = 5.6 \times 10^{17} m^{-3}$ and $I_0 = 15A$.

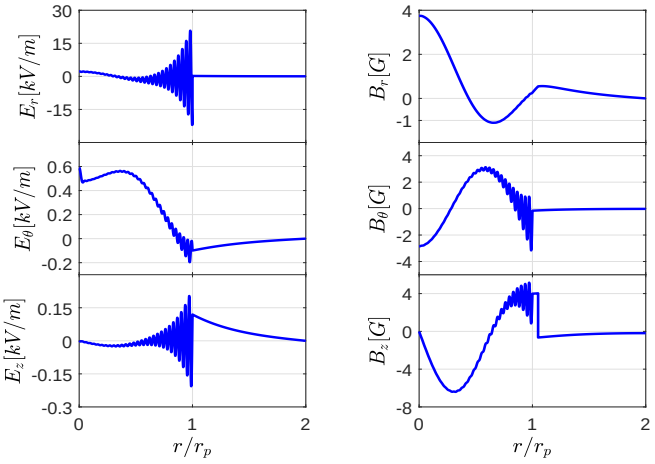

FIGURE 5.9: Radial profiles of electromagnetic fields at $\theta = 0$, $z = L/4$, $n_0 = 5.6 \times 10^{18} m^{-3}$ and $I_0 = 15A$.

$n_0(m^{-3})$	5.6×10^{17}	5.6×10^{18}	5.6×10^{19}
$Re(Z)[\Omega]$	0.394	0.682	0.005

TABLE 5.1: Plasma resistance in different regimes

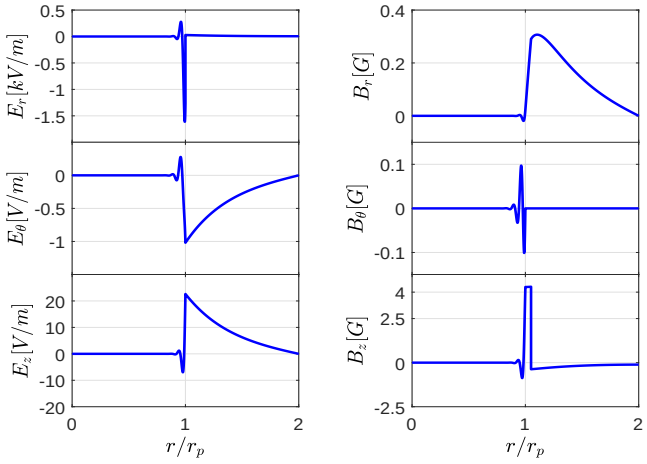

FIGURE 5.10: Radial profiles of electromagnetic fields at $\theta = 0$, $z = L/4$, $n_0 = 5.6 \times 10^{19} m^{-3}$ and $I_0 = 15A$.

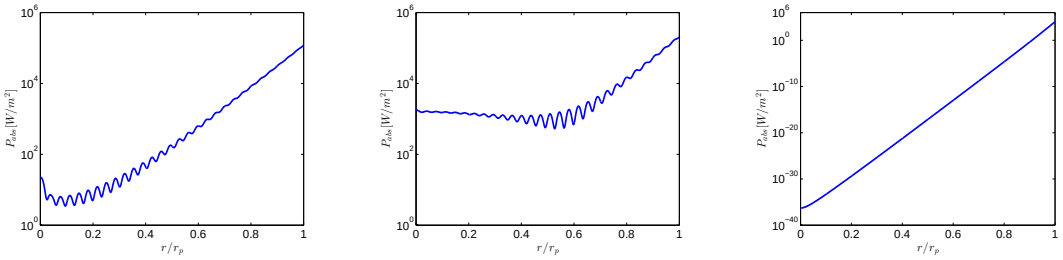

(a) $n_0 = 5.6 \times 10^{17} m^{-3}$ (b) $n_0 = 5.6 \times 10^{18} m^{-3}$ (c) $n_0 = 5.6 \times 10^{19} m^{-3}$

FIGURE 5.11: Power absorption distribution in the radial direction for the case of Fig. 5.8, Fig. 5.9 and Fig. 5.10.

5.2.2. Magnetic field and plasma density

Here, we first introduce the influence of magnetic field and plasma density.

Fig. 5.12 shows the resistance of different modes with variation of the applied magnetic field. The red dashed lines separate the different wave propagation regimes. It illustrates that in the condition of $\omega_{lh} \ll \omega$, the plasma resistance has numerous local peaks because of the existence of multiple eigenmodes in a bounded plasma. Moreover, all the local peak values are in the double wave regime (DWR). For the different modes, the double wave regime becomes narrow if the axial mode increases. It can be explained with the Fig. 3.2. With the l mode increasing, the value $1/k_{\|}d_e$ goes up and the DWR becomes narrower. In the ICR, the resistance is very small since no wave propagates in this regime. Fig. 5.12(d) shows the results considering all the l modes. The maximum resistance is 9.44 ohms at $B_0 = 450G$.

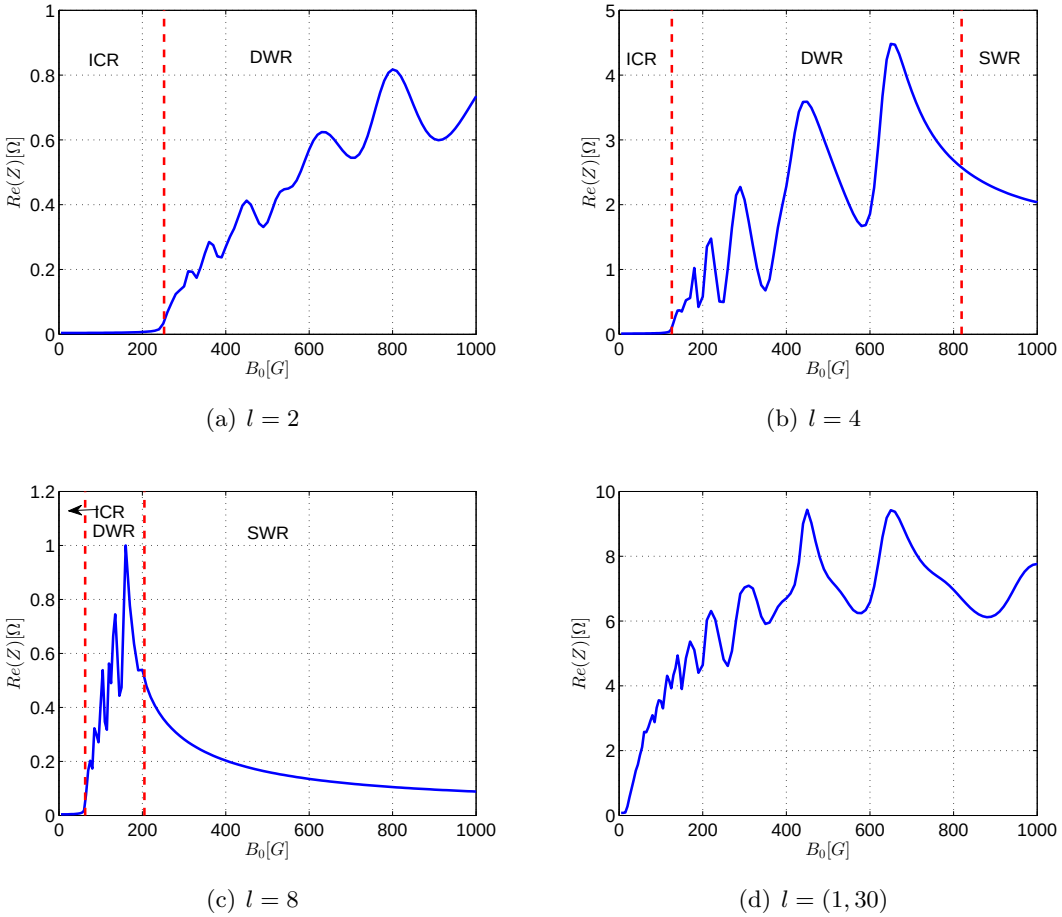

(a) $l = 2$ (b) $l = 4$

(c) $l = 8$ (d) $l = (1, 30)$

FIGURE 5.12: Resistance versus the magnetic field for different l modes. The red dashed lines separate the wave propagation regimes.

The resistance variation with the plasma density is shown in Fig. 5.13. For the different l modes, the resistance increases gradually in the SWR and reaches the local maximum in the double wave regime. In addition, a number of local peaks lie in the DWR. Maps considering both magnetic fields and plasma density variations are shown in Fig. 5.14. The results prove the previous conclusion that the main local peaks of resistance are within the double wave regimes. Furthermore, the relation between the magnetic field and plasma density is almost linear when a family of local peaks is followed. Therefore, higher magnetic field must be applied as the plasma becomes denser. On the other hand, low magnetic field and plasma density should be avoided.

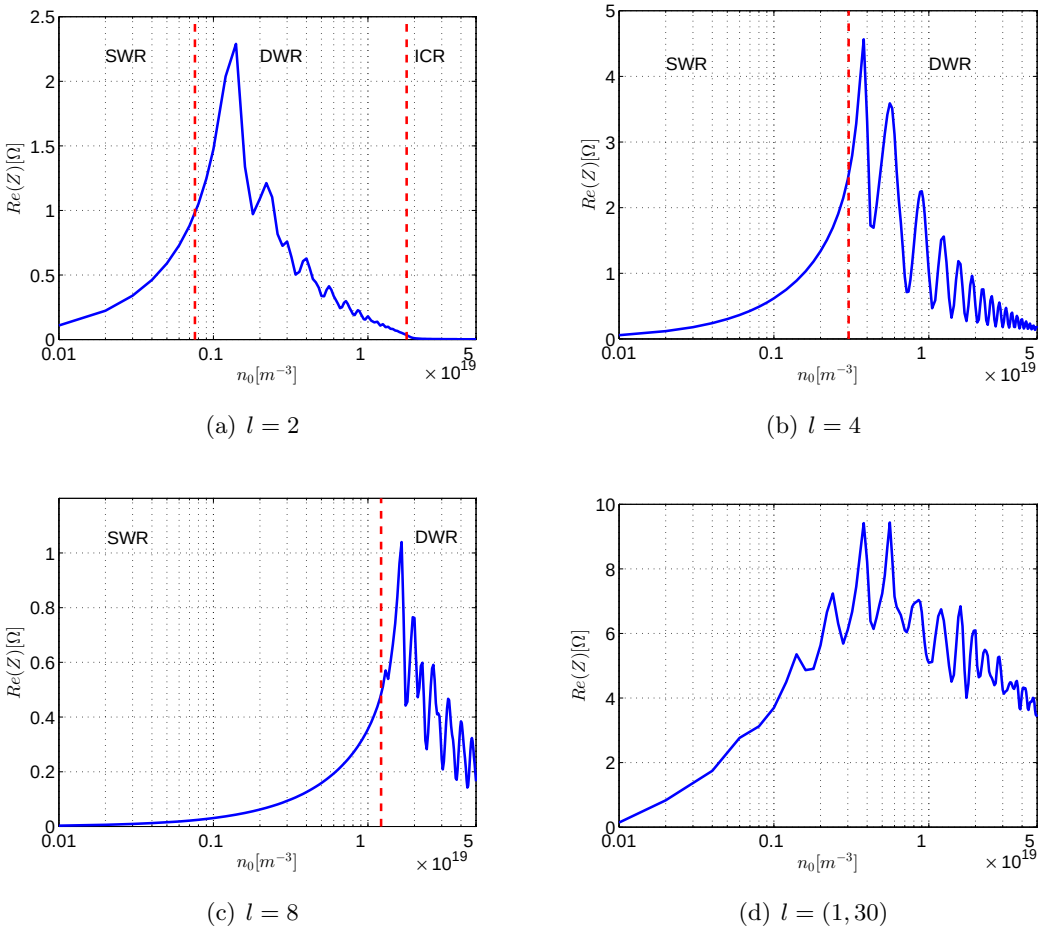

(a) $l = 2$ (b) $l = 4$

(c) $l = 8$ (d) $l = (1, 30)$

FIGURE 5.13: Resistance versus the plasma density for different l modes. The red dashed lines separate the wave propagation regimes.

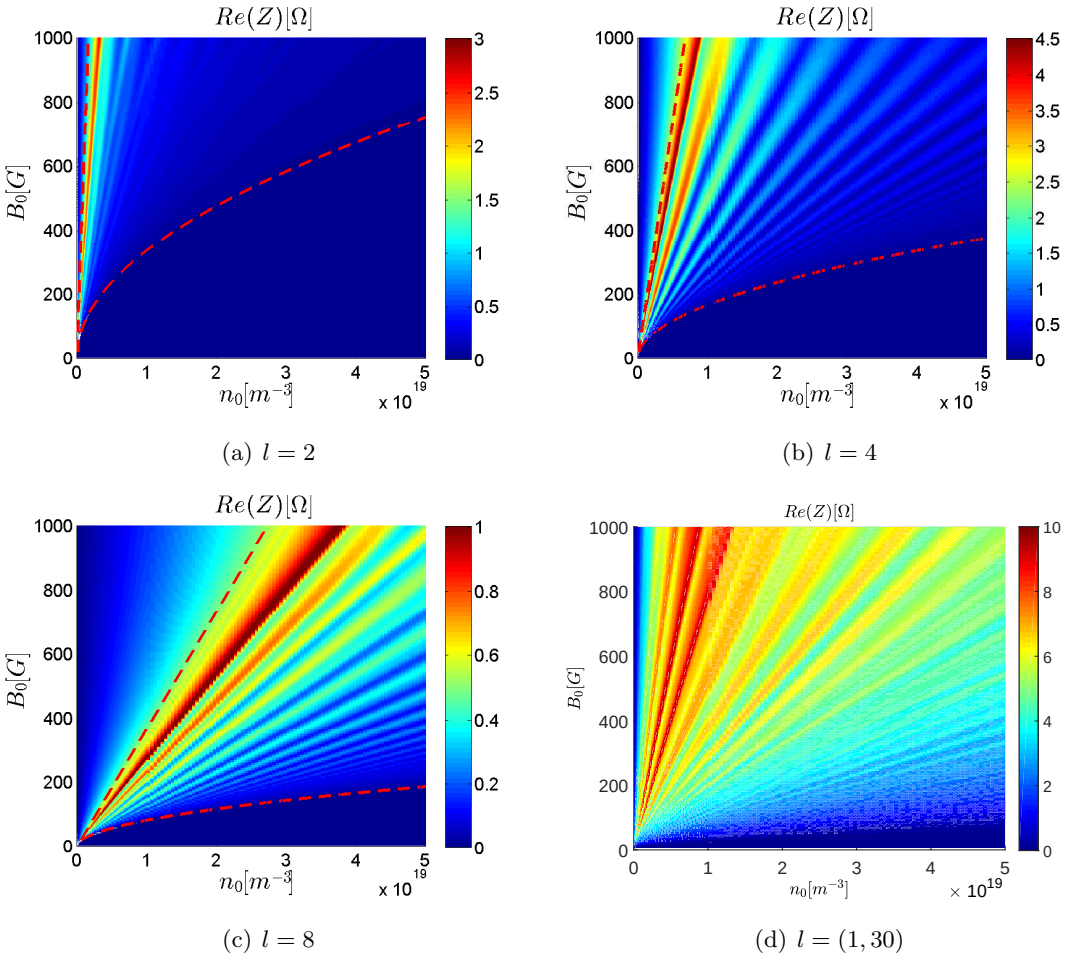

(a) $l = 2$ (b) $l = 4$

(c) $l = 8$ (d) $l = (1, 30)$

FIGURE 5.14: 2D Resistance map as functions of magnetic field and plasma density for different l modes. Red dashed lines are the boundaries of the wave propagation regimes for individual l modes.

5.2.3. Emission frequency and chamber length

The emission frequency ω and the chamber length L are also involved in the wave dispersion relation and therefore influence the development of the waves propagating in one of the three propagation regimes.

The nominal operation frequency is $f_0 = 13.56MHz$ ($\omega = 2\pi f_0$), which is widely used in industry. It is necessary to check whether other frequencies are more appropriate for a helicon source applied in a thruster.

Fig. 5.15 and Fig. 5.16 illustrate the dependence of the plasma resistance with ω_{ce}/ω and ω, which is of the form

$$R \propto \omega \times \text{function}\,(\omega_{ce}/\omega) \tag{5.2}$$

as can be derived from Maxwell equations and the expressions of the dielectric tensor components[62, 66]. R/ω presents several local maxima in the DWR.

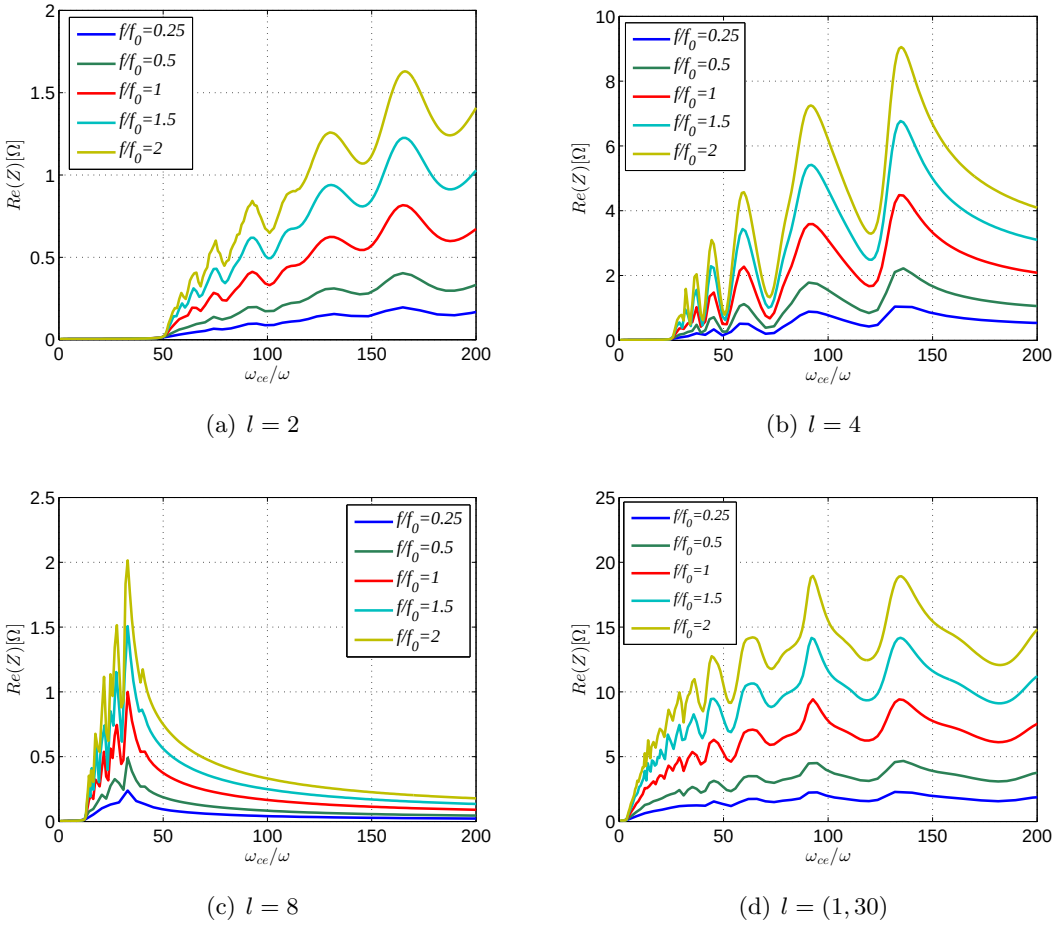

(a) $l = 2$ (b) $l = 4$

(c) $l = 8$ (d) $l = (1, 30)$

FIGURE 5.15: Plasma resistance versus the ratio $\omega_c e/\omega$ for different frequencies. The applied magnetic field is varied proportionally to the frequency. Subplots a to d correspond to different l mode.

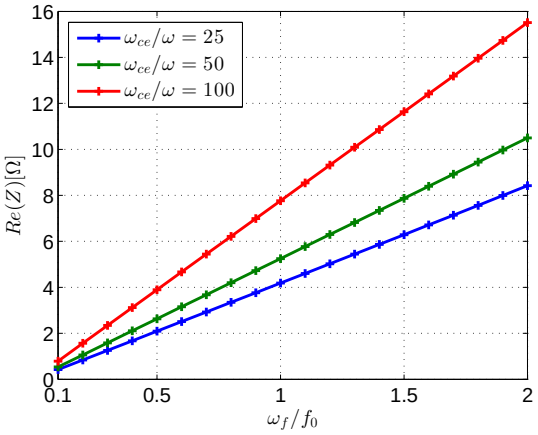

FIGURE 5.16: Plasma resistance varying with the operation frequency for different ω_{ce}/ω.

Therefore, it concluded that taking the highest maximum there, the source design would follow

$$R \propto \omega \propto B_0 \tag{5.3}$$

The larger frequency is applied, the larger resistance can be obtained and requires stronger magnetic fields.

Fig. 5.17 shows the resistance as a function of plasma density for different chamber lengths. With the length increasing, the maximum resistance increases, requiring to decrease the plasma density. Fig. 5.18 shows the relation between the chamber length and plasma density for the maximum resistance of Fig. 5.17. In $l = 8$ case, the resistance profile does not reach the maximum when the chamber length is $L = 0.5L_0$. Hence, only other four cases are shown in Fig. 5.18(c). From the results, the plasma density for maximum resistance can be seen nearly inversely proportional to the chamber length. This can be used to estimate the plasma density for a specific chamber length.

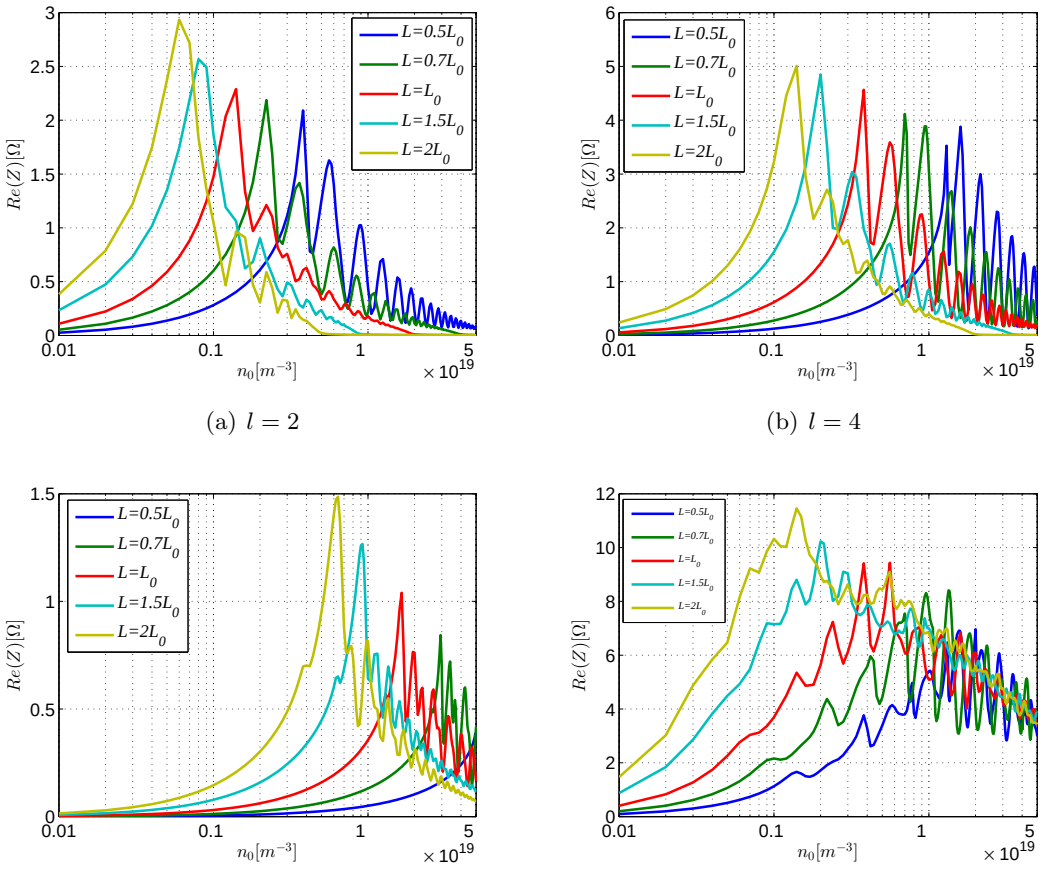

(a) $l = 2$ (b) $l = 4$

(c) $l = 8$ (d) $l = (1, 30)$

FIGURE 5.17: Plasma resistance versus plasma density for different chamber length. Subplots a to d correspond to different l mode.

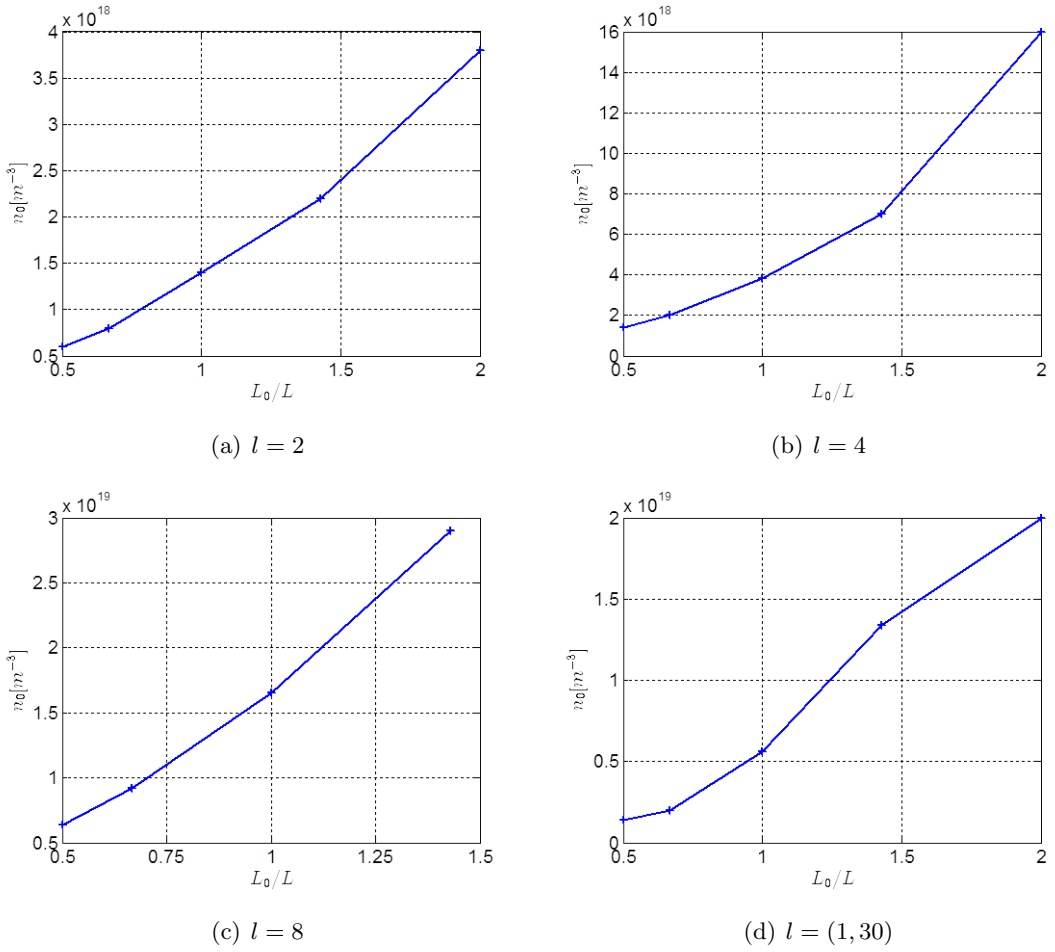

(a) $l = 2$ (b) $l = 4$

(c) $l = 8$ (d) $l = (1, 30)$

FIGURE 5.18: Relation between the chamber length and the plasma density for the maximum resistance peak of Fig. 5.17.

5.2.4. Radial parameters

Finally, we analyze the influence of radial magnitudes on the helicon source for the plasma-wave interaction. In Chapter 4, the antenna radius r_a has been investigated to discuss the influence on resistance. Here, the influence of r_a on resistance related to magnetic fields and plasma densities is taken into account. In addition, the radii of the conducting container r_w will also be discussed in detail. The plasma column radius is fixed at $r_p = 73.5$ mm and all l and m modes discussed above are taken into account.

The influence of different values r_a on plasma resistance with changing magnetic fields and plasma density are given in Fig. 5.19. As we see, for the different antenna radius the shape of resistance profiles are not changed (the same wave modes are involved in computation of R). Fig. 5.20 shows that the resistance decreases with the antenna radius increasing. The relation between them is almost inversely proportional because of the expression of the current density in Chapter 5.

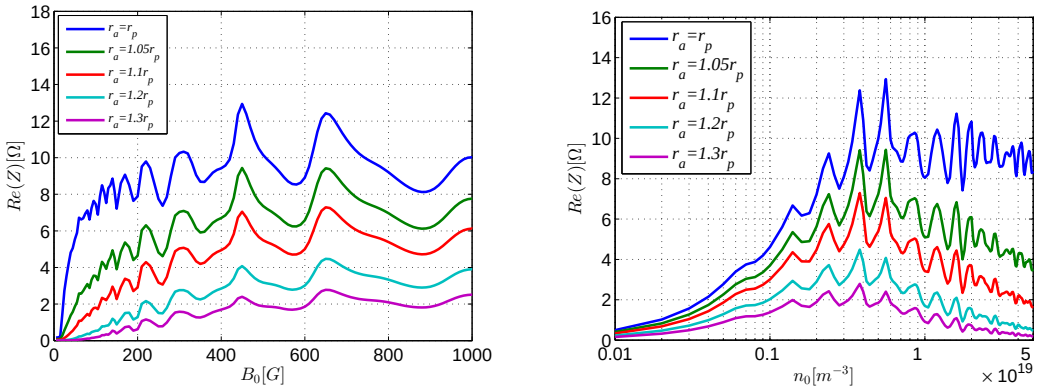

(a) $B_0 - r_a$ (b) $n_0 - r_a$

FIGURE 5.19: Resistance profiles of different r_a varying with the magnetic field and plasma density.

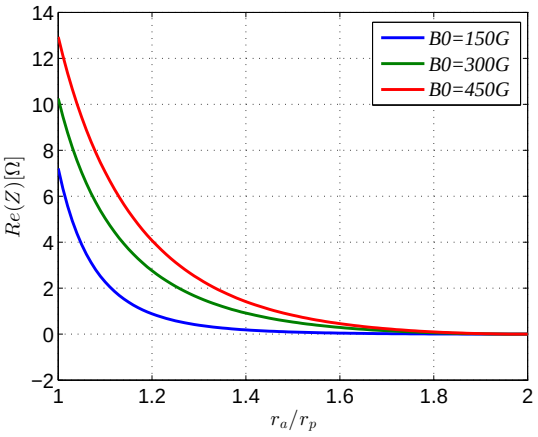

FIGURE 5.20: Plasma resistance versus the antenna radius r_a for different magnetic fields.

Similarly, Fig. 5.21 shows the influence of the radius of cylindrical conducting cage. In this case, the plasma-wave coupling is favoured when the cage is large, and the antenna is not close to it. Fig. 5.22 gives the relation between the resistance and cage radius. The resistance increases with the cage radius until reaching an asymptotic value for $r_w > 1.5r_a$ approximately. The reason is that for the cage too close to the antenna, it tends to produce a short-circuit in it.

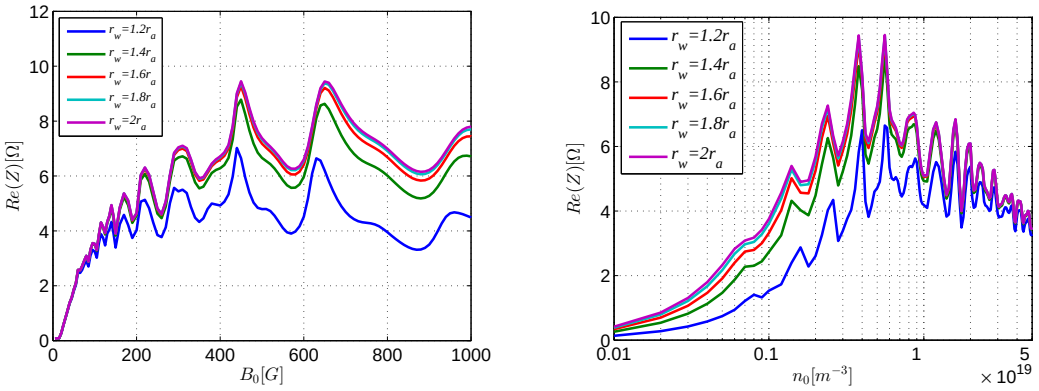

(a) $B_0 - r_w$ (b) $n_0 - r_w$

FIGURE 5.21: Resistance profiles of different r_w varying with the magnetic field and plasma density.

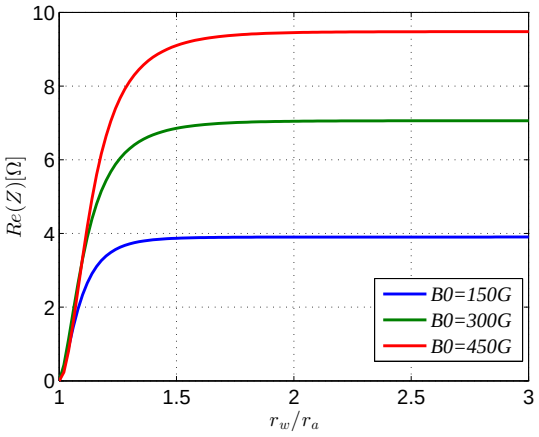

FIGURE 5.22: Plasma resistance versus the wall radius r_w for different magnetic fields.

5.3. Investigation in the extended frequency regime

Up to here the parametric analysis was carried out when the operating frequency ω was much larger than the lower hybrid frequency ω_{lh}, so ion oscillations could be ignored. An estimated scaling law for the optimum parameter combination of helicon source was achieved. While the more conventional operating frequency of helicon plasmas is between the lower hybrid frequency ω_{lh} and the electron cyclotron frequency ω_{ce}, several experimental and theoretical studies suggest that an optimal frequency could be close to the lower hybrid frequency [53]. In this part, the wave propagation and the power deposition is analysed in depth when ω is near ω_{lh}.

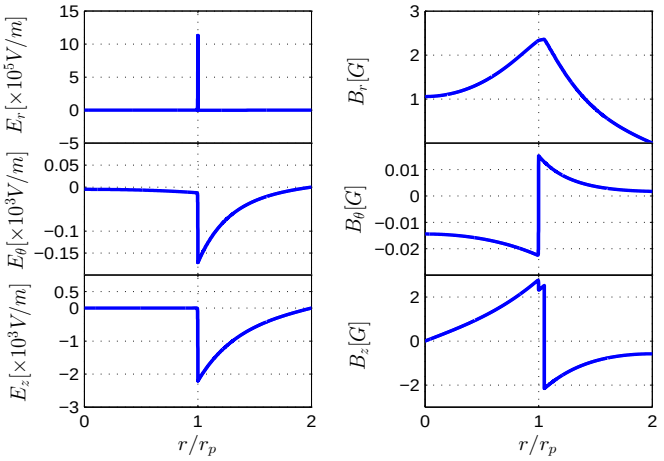

FIGURE 5.23: Radial profiles of electromagnetic fields at $\theta = 0$,$z = L/4$ and $B_0 = 2000G, n_0 = 5.6 \times 10^{17} m^{-3}$.

5.3.1. Wave field and power deposition

Fig. 5.23-5.25 give the wave fields in different two regimes with changing the plasma density. At low plasma density $n_0 = 5.6 \times 10^{17} m^{-3}$, the waves are in the inductive regime(ICR) and no wave propagates in this regimes. The radial distribution of wave fields in Fig. 5.23 shows that the wave in the bulk region of the plasma is small and only has a large amplitude near the boundary. That is the difference between low magnetic fields and high magnetic fields for ICR. The radial power absorption distribution also gives the evidence.

Fig. 5.24 shows the wave in the ICR too, but near the boundary between ICR and HWR at $n_0 = 5.6 \times 10^{18} m^{-3}$. The wave behaviour is similar with $n_0 = 5.6 \times 10^{17} m^{-3}$. However, it has a very high value near the boundary so that it provides larger power than low density case shown in Fig. 5.26. Continuing to increase plasma density to $n_0 = 5.6 \times 10^{19} m^{-3}$. The waves go to helicon wave regime (HWR). Only helicon wave propagates shown in Fig. 5.25 and 5.26(c).

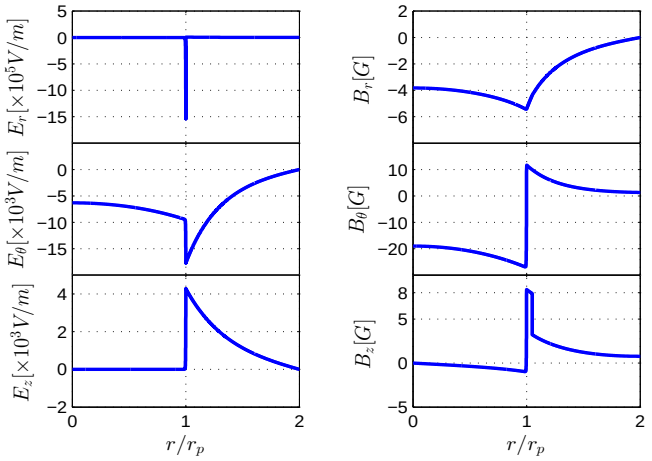

FIGURE 5.24: Radial profiles of electromagnetic fields at $\theta = 0$,$z = L/4$ and $B_0 = 2000G, n_0 = 5.6 \times 10^{18} m^{-3}$.

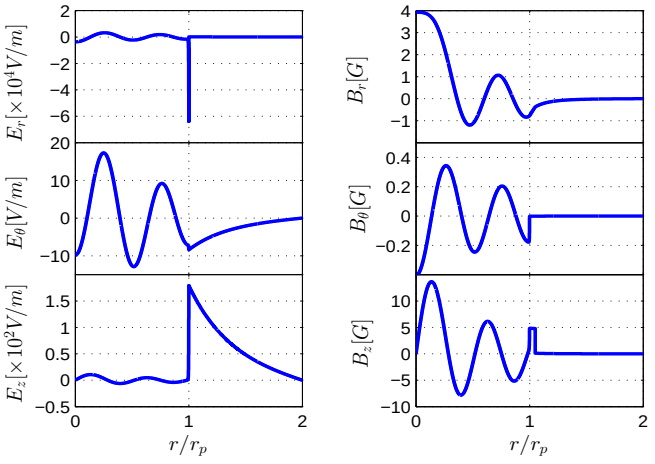

FIGURE 5.25: Radial profiles of electromagnetic fields at $\theta = 0$,$z = L/4$ and $B_0 = 2000G, n_0 = 5.6 \times 10^{19} m^{-3}$.

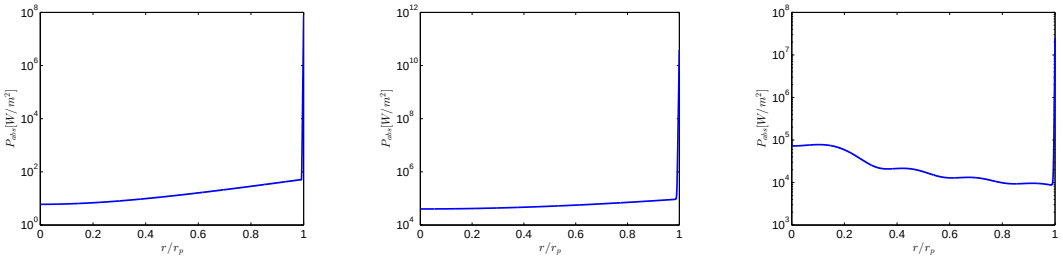

(a) $n_0 = 5.6 \times 10^{17} m^{-3}$ (b) $n_0 = 5.6 \times 10^{18} m^{-3}$ (c) $n_0 = 5.6 \times 10^{19} m^{-3}$

FIGURE 5.26: Power absorption distribution in the radial direction for the case of Fig. 5.23, Fig. 5.24 and Fig. 5.25.

5.3.2. Influence of frequency, magnetic field and plasma density

Fig. 5.27 shows the plasma resistance versus the magnetic field for different l modes and plasma densities, and the RF frequency is fixed. As we see, the resistance when $\omega < \omega_{lh}$ has numerous local peaks in the double wave regime. Then, when the lower hybrid frequency is near the wave frequency, the plasma resistance presents few sharp peaks. For $l = 2$ the resistance is up to 15.08Ω. However, for different l modes, the peak location changes with the magnetic field and the plasma density.

Fig. 5.28 represents the 2D colour maps of resistance varying with the magnetic field and plasma density. The different wave propagation regimes are separated by the dashed line and the solid lines is the separatrix of the lower hybrid frequency. Below the red solid line, we can see numerous local peaks in the double wave regime. The linear relation between the magnetic field and plasma density for the plasma resistance is achieved.

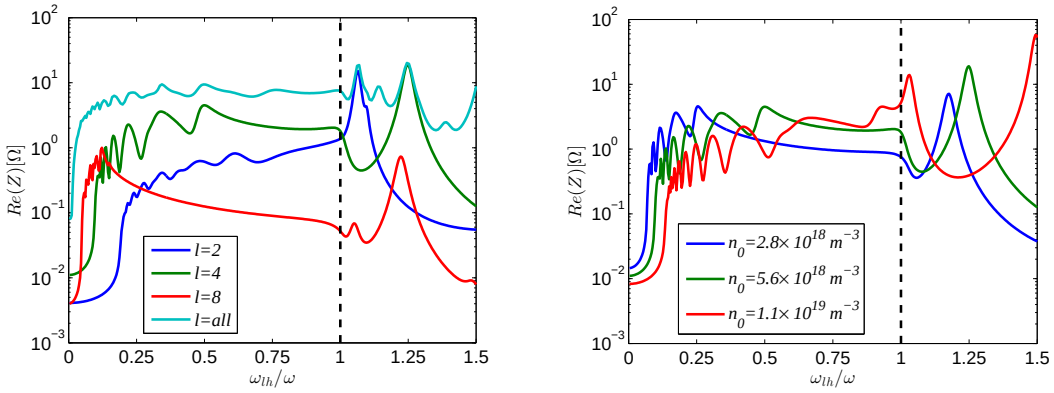

(a) l mode (b) plasma density

FIGURE 5.27: Resistance profiles varying with the ratio ω_{lh}/ω. The RF frequency is fixed and equal to 13.56 MHz. The magnetic field is varied. Figure a shows the case for different l modes, the plasma density is $5.6 \times 10^{18} m^{-3}$. Figure b gives the results of different plasma density for $l = 4$.

Near the lower hybrid resonance, the peaks in the double wave regime become larger. In the regimes above this line, several isolated peaks of resistance emerge and the linear relation between the magnetic field and plasma density for the local peaks still holds. There is a transition near the lower hybrid frequency. The linear slope for the peaks is changed and the values of these peaks are much higher than the peaks in double wave regimes. It is because the change of wave propagation. Near the lower hybrid frequency, the perpendicular wavenumber of TG wave goes to infinite. The inductive mode dominates the behaviour of wave propagation. Hence, the plasma becomes more inductive. In Fig. 5.28(d), all l modes are taken into account. More local peaks lie in the regime above the red line because of the contribution of all modes.

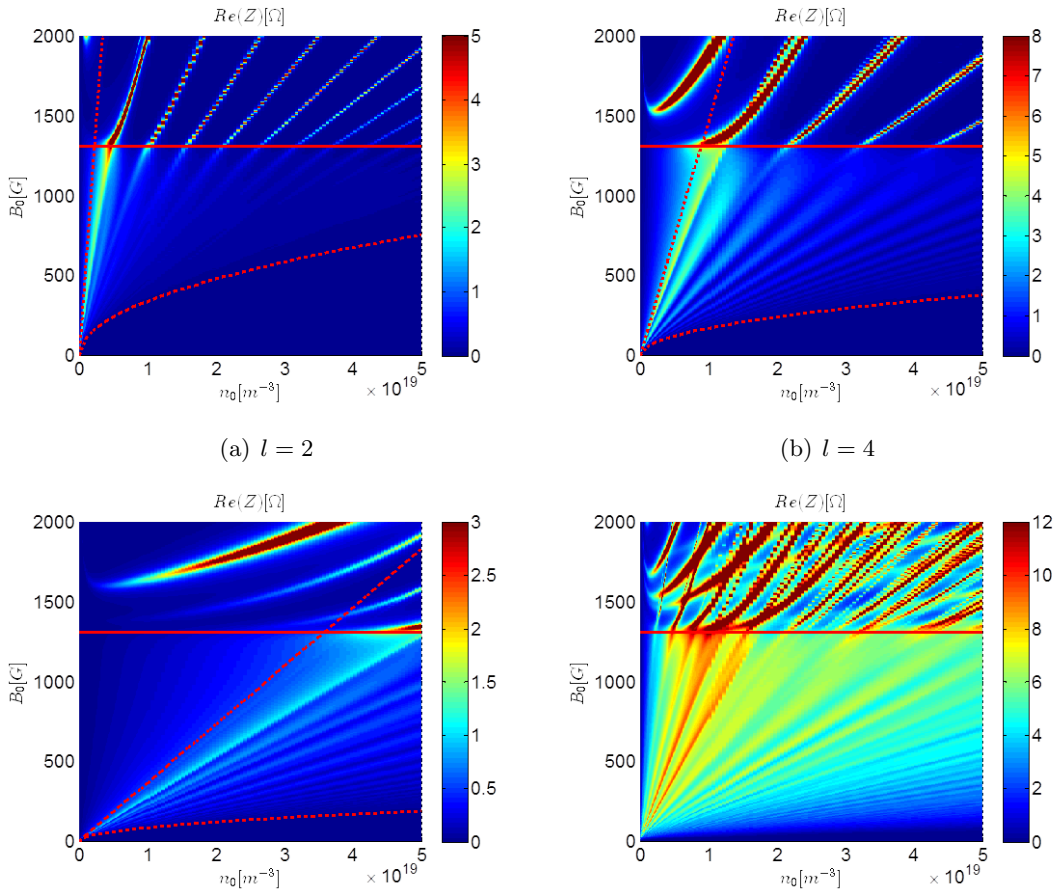

(a) $l = 2$ (b) $l = 4$

(c) $l = 8$ (d) $l = (1, 30)$

FIGURE 5.28: The 2D colour map of resistance varying with both the magnetic field and plasma density for different l mode. The red dashed line represents the different wave propagation regimes and the red solid line is the separatrix of the lower hybrid frequency.

Fig. 5.29(a) gives the resistance for different RF frequency as a function of magnetic fields. All l modes are taken into account. The large peaks appear in the case of $\omega < \omega_{lh}$. The higher the applied frequency the higher the resistance is, provided that the magnetic field increases proportionally.

Fig. 5.29(b) which shows the resistance for different magnetic fields as a function of RF frequency proves this point. And near the lower hybrid resonance, there is a local peak of the resistance. With the frequency increasing, several modes go through the double wave regime, and several local peaks appear. Additionally, We can observe the proportional dependence of the resistance with the antenna frequency in terms of Eq. 3.75. At a fixed ω_{lh}/ω, the power absorption is proportional to the emission frequency.

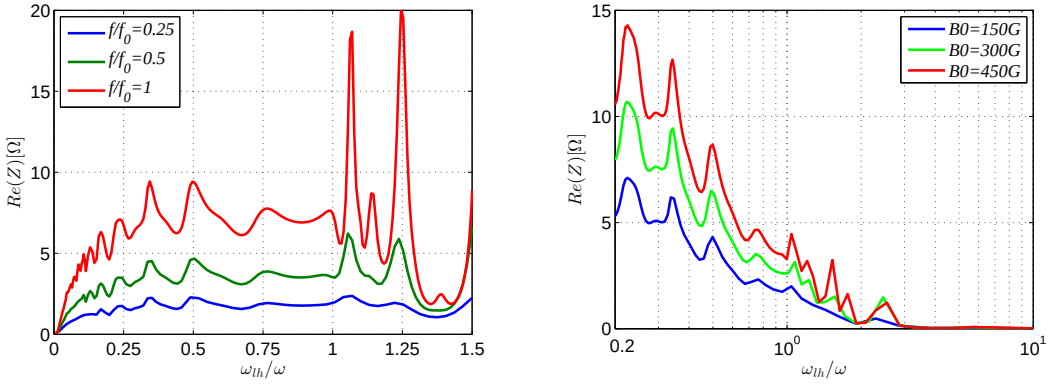

(a) $B_0 - \omega$ case (b) $\omega - B_0$ case

FIGURE 5.29: Plasma resistance versus magnetic field and wave frequency. Figure a shows the resistance as a function of magnetic field with different frequency. The nominal frequency f_0 is $13.56MHz$. Figure b shows the resistance as a function of frequency with different magnetic fields.

5.3.3. Influence of collision frequency

The influence of electron collision frequency ν_e on the resistance is discussed in this part. Fig. 5.30 shows the dependency of electron collision frequency and magnetic fields on the resistance for different modes. In a very low magnetic field (ICR, which means no wave propagates), the resistance increases but still very small when the ν_e becomes larger. Because no propagation occurs in this regime, the power absorption only depends on collisions. In resonance regimes(DWR,SWR and LHR), the resistance has a local maximum for each magnetic field with changing the electron collision frequency, and then the resistance goes down if ν_e increases. When ν_e reaches up to a specific value, the resistance tends to be a constant. This illustrates that in a specific range, the collision frequency influences the power absorption largely. Furthermore, a very large ν_e is not beneficial for the power deposition.

Observing the variation of different magnetic fields in the range of $\omega > \omega_{lh}$, the value of ν_e which can make the resistance maximum become smaller. This means that only a very small range of electron collision frequency can effect the resistance in a high magnetic field. For a relatively large ν_e, the resistance becomes near constant. However, a different behavior appears when $\omega < \omega_{lh}$. In a wide range of ν_e, the resistance keeps a very high value if the magnetic field makes it reach a local peak.

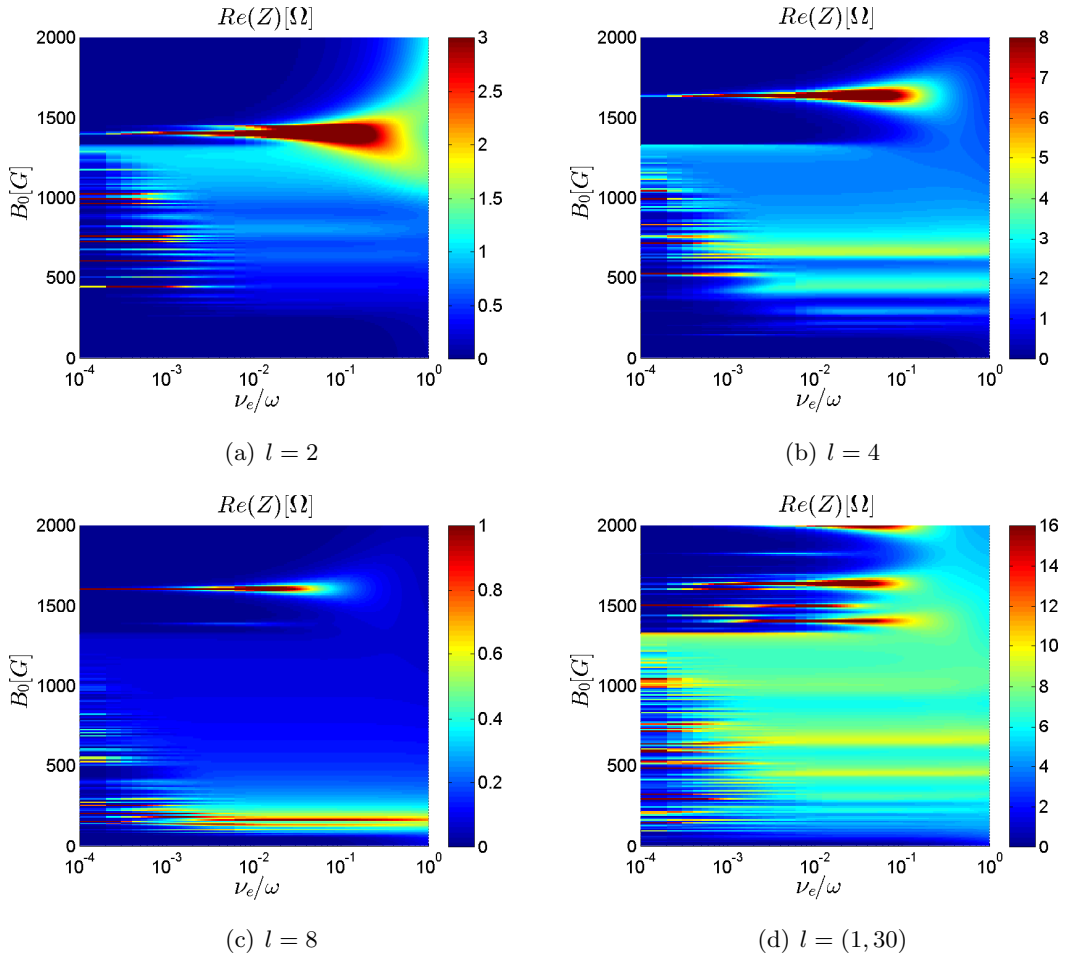

(a) $l = 2$ (b) $l = 4$

(c) $l = 8$ (d) $l = (1, 30)$

FIGURE 5.30: The 2D colour map of resistance varying with both the magnetic field and electron collision frequency for different l mode.

5.4. Summary

The plasma-wave coupling has been studied for different parameters including the applied magnetic field, plasma density, RF frequency and antenna geometry. In the study of antenna parameters, it is found that the plasma resistance is largest when the antenna is close to the plasma column. Second, the optimum combination of antenna length L_a and antenna position z_a has been calculated for different types of antennas. For the double-saddle antenna family, the behavior is identical for the whole family, with the Nagoya III yielding the maximum resistance at some intermediate antenna axial lengths and locations. The helical family behaves differently. Higher turn-number antennas can yield larger resistances but require larger plasma column lengths, which eventually limits the number of turns to 2. For the geometry of the plasma column selected in our case, the optimal antenna is the helical with 1 or 2 turns.

For magnetic field and plasma density, in order to obtain the maximum resistance of helicon source, the larger the plasma density is, the larger the magnetic field should be. The optimal combination for plasma density and magnetic field is inside the DWR and follows an almost linear trend. Then, the maximum resistance can be reached with higher RF frequencies.

The parametric investigation yields a fitting scaling law for the optimal parameter combination. The parameter combination is always within the double wave regime and the optimal magnetic field is proportional to the plasma density, RF frequency and the plasma density is nearly inversely proportional to the chamber length. Hence, the estimated scaling law can be written as

$$B_0 \propto \omega n_0 L \tag{5.4}$$

The relation can be used to estimate the parameter and performance when designing a helicon source. It was found that the radius of the external conducting cage must be large enough (more than $1.5r_a$) in order to avoid short-circuit effects with the antenna RF fields.

The characteristics of helicon plasmas near the lower hybrid resonance were investigated numerically. A large local peak of resistance is achieved near the lower hybrid resonance. The positions of these peaks are different for each axial l mode, and depend on plasma density. The linear relation between magnetic fields and plasma density is still valid. The transition in the lower hybrid frequency changes the linear slope.

In addition, a higher frequency gives a higher resistance but requires larger magnetic fields. The resistance is essentially proportional to the applied frequency. For a fixed frequency, the magnetic field near the lower hybrid resonance provides larger resistance. This could be beneficial for wave power deposition. The influence of electron collision frequency on the resistance depends on the wave resonance and the resistance tends to be a constant for large collision frequencies.

Chapter 6

The 2D Plasma-wave Interaction Model

The 2D cylindrical plasma-wave interaction model presented in Chapter 3 is used in this chapter to explore the 2D aspects of the plasma-wave interaction problem. The finite-differences computational code HELWAVE2D is developed to investigate the wave propagation, antenna coupling and power absorption in the HPT. Non-uniform plasma density and magnetic field profiles are considered in both radial and axial directions. The wave propagation and power absorption are studied not only in the helicon source but also in the near region of plasma plume.

6.1. Introduction

A general understanding of wave behaviors and power deposition in cylindrically uniform plasmas have been obtained in previous chapters using the 1D plasma-wave model. However, the plasma density and magnetic field are not purely uniform in the HPT. Additionally, the plasma is not confined to the plasma source, but expands downstream forming a plasma plume, with which the wave can interact too.

The inhomogeneous properties of helicon plasmas in HPT are important and can strongly influence the wave propagation and power absorption [71, 111]. Therefore, the 2D cylindrical plasma-wave model is considered to deal with the non-uniformity. In order to investigate this issue in helicon plasmas, Takechi and Shinohara [110] used the Transport Analyzing System for tokamaK/Wave analysis (TASK/WA) code which was developed by Fukuyama to study the 2D convergent and divergent magnetic fields in helicon plasmas and compared the numerical results with experimental data. Mouzouris and

Scharer [111] developed a 2D wave code MAXEB which includes not only the collisional damping but Landau damping to investigate the power absorptions. It is found that the collisional damping is the dominant heating mechanism for moderate pressures and higher density ranges [111]. In comparison, the Landau damping becomes important at low pressure and heats the electrons mainly at the surface where the resonant electrons have velocities near the wave phase velocity [111]. Kinder and Kushner [112, 113] developed a two-dimensional Hybrid plasma Equiqment Model (HPEM) to study the power absorption and plasma transport in helicon sources. The Electromagnetics module in this self-consistent model can deal with the 2D applied magnetic fields. However, this model mainly focus on the pure helicon mode and neglect the influence of TG mode [114]. They involved the influence of TG mode in a later paper [112]. The electrostatic term was only approximated by a damping factor. Similarly, the other self-consistent model which can deal with 2D non-uniform properties and involve the influence of TG mode are introduced by Bose et al [115]. The results show that the propagation of waves is enhanced in the downstream with increasing the electromagnet coil current ratio (CCR) and this is accompanied by a increase of power absorption in the downstream. Additionally, another 2D plasma-wave code using finite difference method was implemented by Guangye et al [74]. The staggered grids of Yee' s scheme [116] were applied to discretize the EM field. In this approach it is easier to deal with the boundary condition and it is naturally suited for Maxwell equations [116]. The radially localized helicon mode (RLH) has been studied by using this code [74, 75]. The approach of staggered grids is also applied in our code because of these advantages.

However, these codes and previous studies have been rather limited, and only treated the cylindrical plasma inside the source. The wave propagation into the plasma plume is not taken into account. In the HPT, this problem is significant in order to improve the performance. In the plasma plume, the non- uniformity becomes stronger especially for the applied magnetic field, considering the divergence in the magnetic nozzle. Therefore, the influence of the plasma plume on the wave propagation and power deposition must be taken into account. Based on this purpose, the 2D plasma-wave interaction code HELWAVE2D is developed here and the investigation of plasma plume effects on wave propagation and absorption is carried out.

6.2. Numerical scheme of the 2D code

6.2.1. The governing equations

Based on the typical geometry structure of HPT and appropriate assumptions, the cold plasma dielectric tensor and governed by Maxwell equations was derived in Chapter 3. Similar to the 1D model, the normalization of the variables is implemented as follows:

$$\hat{r} = \frac{r\omega}{c}, \quad \hat{\boldsymbol{E}} = \frac{\boldsymbol{E} r_a}{\mu_0 I_a c}, \quad \hat{\boldsymbol{j_a}} = \frac{\boldsymbol{j_a} r_a c}{I_a \omega},$$

$$\hat{z} = \frac{z\omega}{c}, \quad \hat{\boldsymbol{B}} = \frac{\boldsymbol{B} r_a}{\mu_0 I_a}, \quad \hat{\boldsymbol{D}} = \frac{\boldsymbol{D} r_a c}{I_a \omega}.$$

Applying these relations, Maxwell equations can be written in the form of Eq. 3.47-3.52, repeated here for convenience:

$$\frac{im}{\hat{r}}\hat{E}_z - \frac{\partial}{\partial \hat{z}}\hat{E}_\theta - i\hat{B}_r = 0, \tag{6.1}$$

$$\frac{\partial}{\partial \hat{z}}\hat{E}_r - \frac{\partial}{\partial \hat{r}}\hat{E}_z - i\hat{B}_\theta = 0, \tag{6.2}$$

$$\frac{1}{\hat{r}}\frac{\partial}{\partial \hat{r}}\left(\hat{r}\hat{E}_\theta\right) - \frac{im}{\hat{r}}\hat{E}_r - i\hat{B}_z = 0, \tag{6.3}$$

$$\frac{im}{\hat{r}}B_z - \frac{\partial}{\partial \hat{z}}\hat{B}_\theta + i\hat{D}_r = \hat{j}_{ra}, \tag{6.4}$$

$$\frac{\partial}{\partial \hat{z}}\hat{B}_r - \frac{\partial}{\partial \hat{r}}\hat{B}_z + i\hat{D}_\theta = \hat{j}_{\theta a}, \tag{6.5}$$

$$\frac{1}{\hat{r}}\frac{\partial}{\partial \hat{r}}\left(\hat{r}\hat{B}_\theta\right) - \frac{im}{\hat{r}}\hat{B}_r + i\hat{D}_z = \hat{j}_{za} \tag{6.6}$$

Hence, a set of first-order differential equations which can be solved numerically is obtained. Here, the finite difference method is applied to get the solution. The physical domain shown in Fig. 3.4 is discretized and Yee's scheme is applied, resulting in 4 staggered grids [74, 116].

The staggered grids are shown in Fig. 6.1. Each grid defines different components of the electric and magnetic field, and fractional indexing of the nodes is used to refer to each grid, according to [74]

$$\hat{r}_g = \frac{\hat{r}_{g+1/2} + \hat{r}_{g-1/2}}{2}, \qquad \hat{z}_h = \frac{\hat{z}_{h+1/2} + \hat{z}_{h-1/2}}{2} \tag{6.7}$$

The physical domain is discretized from $\hat{r} \in [0, \hat{r}_w]$ and $\hat{z} \in \left[0, \hat{L}\right]$. The origin point, $(0,0)$, corresponds with node $\left(\hat{r}_{1/2}, \hat{z}_{1/2}\right)$ and the bounding point $(\hat{r}_w, \hat{L})$ is $\left(\hat{r}_{N_r+1/2}, \hat{z}_{N_z+1/2}\right)$, where N_r and N_z are integers. Therefore, the integer indexes $g \in [0, N_r]$ and $h \in [0, N_z]$ are defined in radial and axial directions, respectively. Lastly, each rectangular grid (A, B, C and D) saves the following wavefield variables:

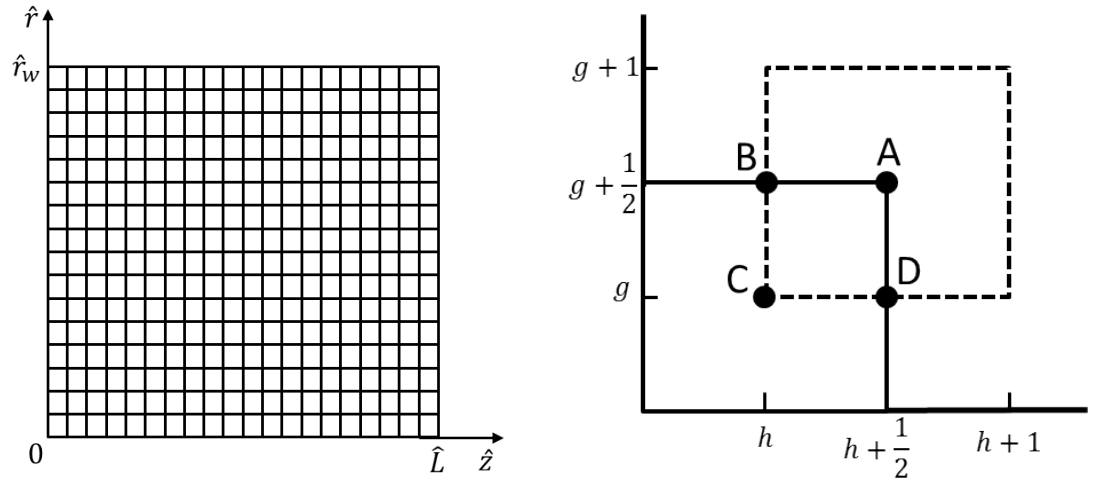

(a) Full grids (b) Staggered grids

FIGURE 6.1: Computational grid structure

Grid A: $\left(r_{g+1/2}, z_{h+1/2}\right)$, where $g \in [0, N_r]$ and $h \in [0, N_z]$. The quantities in grid A are $\hat{D}_\theta$, $\hat{E}_\theta$ and $\hat{j}_{\theta a}$.

Grid B: $\left(r_{g+1/2}, z_h\right)$, where $g \in [0, N_r]$ and $h \in [1, N_z]$. The quantities in grid B are $\hat{D}_z$, $\hat{E}_z$, $\hat{B}_r$ and $\hat{j}_{za}$.

Grid C: (r_g, z_h), where $g \in [1, N_r]$ and $h \in [1, N_z]$. The quantity in grid C is $\hat{B}_\theta$.

Grid D: $\left(r_g, z_{h+1/2}\right)$, where $g \in [1, N_r]$ and $h \in [0, N_z]$. The quantities in grid D are $\hat{D}_r$, $\hat{E}_r$, $\hat{B}_z$ and $\hat{j}_{ra}$.

The resulting finite difference equations are presented in Eqs. 6.9-6.14. In addition, it is necessary to give the range of indexes for each equations because each of them involve different quantities. This information is summarized in Tab. 6.1.

Equation	Parameter	Index range for r	Index range for z
Eq. 6.9	$\hat{E}_\theta$, $\hat{E}_z$, $\hat{B}_r$	$g \in [1, N_r - 1]$	$h \in [1, N_z]$
Eq. 6.10	$\hat{E}_r$, $\hat{E}_z$, $\hat{B}_\theta$	$g \in [1, N_r]$	$h \in [1, N_z]$
Eq. 6.11	$\hat{E}_r$, $\hat{E}_\theta$, $\hat{B}_z$	$g \in [1, N_r]$	$h \in [1, N_z - 1]$
Eq. 6.12	$\hat{B}_\theta$, $\hat{B}_z$, $\hat{D}_r$, $\hat{j}_r$	$g \in [1, N_r]$	$h \in [1, N_z - 1]$
Eq. 6.13	$\hat{B}_r$, $\hat{B}_z$, $\hat{D}_\theta$, $\hat{j}_\theta$	$g \in [1, N_r - 1]$	$h \in [1, N_z - 1]$
Eq. 6.14	$\hat{B}_r$, $\hat{B}_\theta$, $\hat{D}_z$, $\hat{j}_z$	$g \in [1, N_r - 1]$	$h \in [1, N_z]$

TABLE 6.1: The index range for each differential equations.

After the linear equation system for the whole grid structure has been established, it can be written as

$$A\mathbf{x} = \mathbf{b} \tag{6.8}$$

where A is the matrix of coefficients, $\mathbf{x}$ expresses the unknown EM field and $\mathbf{b}$ stores the electric current densities in the antenna.

$$\frac{im}{\hat{r}_{g+1/2}}\hat{E}_z\left(\hat{r}_{g+1/2},\hat{z}_h\right)-\frac{\hat{E}_\theta\left(\hat{r}_{g+1/2},\hat{z}_{h+1/2}\right)-\hat{E}_\theta\left(\hat{r}_{g+1/2},\hat{z}_{h-1/2}\right)}{\hat{z}_{h+1/2}-\hat{z}_{h-1/2}} - i\hat{B}_r\left(\hat{r}_{g+1/2},\hat{z}_h\right)=0, \tag{6.9}$$

$$\frac{\hat{E}_r\left(\hat{r}_g,\hat{z}_{h+1/2}\right)-\hat{E}_r\left(\hat{r}_g,\hat{z}_{h-1/2}\right)}{\hat{z}_{h+1/2}-\hat{z}_{h-1/2}}-\frac{\hat{E}_z\left(\hat{r}_{g+1/2},\hat{z}_h\right)-\hat{E}_z\left(\hat{r}_{g-1/2},\hat{z}_h\right)}{\hat{r}_{g+1/2}-\hat{r}_{g-1/2}} - i\hat{B}_\theta\left(\hat{r}_g,\hat{z}_h\right)=0, \tag{6.10}$$

$$\frac{\hat{r}_{g+1/2}\hat{E}_\theta\left(\hat{r}_{g+1/2},\hat{z}_{h+1/2}\right)-\hat{r}_{g-1/2}\hat{E}_\theta\left(\hat{r}_{g-1/2},\hat{z}_{h+1/2}\right)}{r_g\left(\hat{r}_{g+1/2}-\hat{r}_{g-1/2}\right)} - \frac{im}{\hat{r}_g}\hat{E}_r\left(\hat{r}_g,\hat{z}_{h+1/2}\right)-i\hat{B}_z\left(\hat{r}_g,\hat{z}_{h+1/2}\right)=0, \tag{6.11}$$

$$\frac{im}{\hat{r}_g}\hat{B}_z\left(\hat{r}_g,\hat{z}_{h+1/2}\right)-\frac{\hat{B}_\theta\left(\hat{r}_g,\hat{z}_{h+1}\right)-\hat{B}_\theta\left(\hat{r}_g,\hat{z}_h\right)}{\hat{z}_{h+1}-\hat{z}_h} + i\hat{D}_r\left(\hat{r}_g,\hat{z}_{h+1/2}\right)=\hat{j}_{ra}\left(\hat{r}_k,\hat{z}_{h+1/2}\right), \tag{6.12}$$

$$\frac{\hat{B}_r\left(\hat{r}_{g+1/2},\hat{z}_{h+1}\right)-\hat{B}_r\left(\hat{r}_{g+1/2},\hat{z}_h\right)}{\hat{z}_{h+1}-\hat{z}_h}-\frac{\hat{B}_z\left(\hat{r}_{g+1},\hat{z}_{h+1/2}\right)-\hat{B}_z\left(\hat{r}_g,\hat{z}_{h+1/2}\right)}{\hat{r}_{g+1}-\hat{r}_g} + i\hat{D}_\theta\left(\hat{r}_{g+1/2},\hat{z}_{h+1/2}\right)=\hat{j}_{\theta a}\left(\hat{r}_{k+1/2},\hat{z}_{h+1/2}\right), \tag{6.13}$$

$$\frac{\hat{r}_{g+1}\hat{B}_\theta\left(\hat{r}_{g+1},\hat{z}_h\right)-\hat{r}_g\hat{B}_\theta\left(\hat{r}_g,\hat{z}_h\right)}{r_{g+1/2}\left(\hat{r}_{g+1}-\hat{r}_g\right)}-\frac{im}{\hat{r}_{g+1/2}}\hat{B}_r\left(\hat{r}_{g+1/2},\hat{z}_h\right) + i\hat{D}_z\left(\hat{r}_{g+1/2},\hat{z}_h\right)=\hat{j}_{za}\left(\hat{r}_{g+1/2},\hat{z}_h\right) \tag{6.14}$$

6.2.2. Interpolation methods

Due to the way the different field quantities are defined in each grids, the component of the displacement field $\mathbf{D}$ involving electric fields need an interpolation procedure to be computed inside the plasma. The main principle of the interpolation is to satisfy the condition $\nabla\cdot\mathbf{D}=\mathbf{0}$ [94]. The discretization error due to the interpolation procedure leads to a virtually external charge which has to be minimized. This interpolation approach has been introduced by Guangye [74]. However, in the case of a non-uniform, non-axial

magnetic field, this procedure has to be adapted and must include all components of the electric displacement field. The expression is as follows:

$$\begin{aligned}\hat{D}_r\left(\hat{r}_g,\hat{z}_{h+1/2}\right) &= \kappa_{11}\left(\hat{r}_g,\hat{z}_{h+1/2}\right)\hat{E}_r\left(\hat{r}_g,\hat{z}_{h+1/2}\right)\\ &+\frac{1}{2\hat{r}_g}[\hat{r}_{g+1/2}\kappa_{12}\left(\hat{r}_{g+1/2},\hat{z}_{h+1/2}\right)\hat{E}_\theta\left(\hat{r}_{g+1/2},\hat{z}_{h+1/2}\right)\\ &+\hat{r}_{g-1/2}\kappa_{12}\left(\hat{r}_{g-1/2},\hat{z}_{h+1/2}\right)\hat{E}_\theta\left(\hat{r}_{g-1/2},\hat{z}_{h+1/2}\right)]\\ &+\frac{1}{4}[\kappa_{13}\left(\hat{r}_{g-1/2},\hat{z}_h\right)\hat{E}_z\left(\hat{r}_{g-1/2},\hat{z}_h\right)+\kappa_{13}\left(\hat{r}_{g-1/2},\hat{z}_{h+1}\right)\hat{E}_z\left(\hat{r}_{g-1/2},\hat{z}_{h+1}\right)\\ &+\kappa_{13}\left(\hat{r}_{g+1/2},\hat{z}_h\right)\hat{E}_z\left(\hat{r}_{g+1/2},\hat{z}_h\right)+\kappa_{13}\left(\hat{r}_{g+1/2},\hat{z}_{h+1}\right)\hat{E}_z\left(\hat{r}_{g+1/2},\hat{z}_{h+1}\right)]\end{aligned} \tag{6.15}$$

$$\begin{aligned}\hat{D}_\theta\left(\hat{r}_{g+1/2},\hat{z}_{h+1/2}\right) &= \kappa_{22}\left(\hat{r}_{g+1/2},\hat{z}_{h+1/2}\right)\hat{E}_\theta\left(\hat{r}_{g+1/2},\hat{z}_{h+1/2}\right)\\ &+\frac{1}{2}[\kappa_{21}\left(\hat{r}_g,\hat{z}_{h+1/2}\right)\hat{E}_r\left(\hat{r}_g,\hat{z}_{h+1/2}\right)+\kappa_{21}\left(\hat{r}_{g+1},\hat{z}_{h+1/2}\right)\hat{E}_r\left(\hat{r}_{g+1},\hat{z}_{h+1/2}\right)]\\ &+\frac{1}{2}[\kappa_{23}\left(\hat{r}_{g+1/2},\hat{z}_h\right)\hat{E}_z\left(\hat{r}_{g+1/2},\hat{z}_h\right)+\kappa_{23}\left(\hat{r}_{g+1/2},\hat{z}_{h+1}\right)\hat{E}_z\left(\hat{r}_{g+1/2},\hat{z}_{h+1}\right)]\end{aligned} \tag{6.16}$$

$$\begin{aligned}\hat{D}_z\left(\hat{r}_{g+1/2},\hat{z}_h\right) &= \kappa_{33}\left(\hat{r}_{g+1/2},\hat{z}_h\right)\hat{E}_z\left(\hat{r}_{g+1/2},\hat{z}_h\right)\\ &+\frac{1}{2}[\kappa_{32}\left(\hat{r}_{g+1/2},\hat{z}_{h-1/2}\right)\hat{E}_\theta\left(\hat{r}_{g+1/2},\hat{z}_{h-1/2}\right)+\kappa_{32}\left(\hat{r}_{g+1/2},\hat{z}_{h+1/2}\right)\hat{E}_\theta\left(\hat{r}_{g+1/2},\hat{z}_{h+1/2}\right)]\\ &+\frac{1}{4}[\kappa_{31}\left(\hat{r}_g,\hat{z}_{h-1/2}\right)\hat{E}_r\left(\hat{r}_g,\hat{z}_{h-1/2}\right)+\kappa_{31}\left(\hat{r}_g,\hat{z}_{h+1/2}\right)\hat{E}_r\left(\hat{r}_g,\hat{z}_{h+1/2}\right)\\ &+\kappa_{31}\left(\hat{r}_{g+1},\hat{z}_{h-1/2}\right)\hat{E}_r\left(\hat{r}_{g+1},\hat{z}_{h-1/2}\right)+\kappa_{31}\left(\hat{r}_{g+1},\hat{z}_{h+1/2}\right)\hat{E}_r\left(\hat{r}_{g+1},\hat{z}_{h+1/2}\right)]\end{aligned} \tag{6.17}$$

The advantage of this approach is that the error is of the order of h^2/λ^2, where h is the step size and λ is the characteristic scale length of electric field [74].

6.2.3. Boundary conditions

To model the presence of the vacuum chamber walls in Fig. 3.4, the simulation domain is enclosed by ideally conductor boundary conditions. Hence, the tangential component of electric field is equal to zero. The boundary conditions are summarized as

$$\hat{E}_r\left(\hat{r},0\right)=\hat{E}_\theta\left(\hat{r},0\right)=0, \tag{6.18}$$

$$\hat{E}_r\left(\hat{r},\hat{L}\right)=\hat{E}_\theta\left(\hat{r},\hat{L}\right)=0, \tag{6.19}$$

$$\hat{E}_\theta\left(\hat{r}_w,\hat{z}\right)=\hat{E}_z\left(\hat{r}_w,\hat{z}\right)=0. \tag{6.20}$$

The conditions on the magnetic field components are directly derived from the above, noting that the normal magnetic field component to the walls is equal to zero. In addition, axis conditions is applied at $r=0$. To analyze equations, this conditions

depend on the different value of m mode, so we have [74, 76]

$$\hat{E}_z\left(0,\hat{z}\right)=\left[\hat{r}\hat{E}_\theta\right]\left(0,\hat{z}\right)=0, \qquad (m\neq 0) \tag{6.21}$$

$$\left[\hat{r}\hat{E}_\theta\right]\left(0,\hat{z}\right)=\hat{B}_\theta\left(0,\hat{z}\right)=0, \qquad (m=0)\,. \tag{6.22}$$

An important advantage of Yee's scheme is that it can deal with the ideally conducting boundary condition easily, placing the boundary condition at the correct sub-grid.

6.2.4. The antenna discretizations

The antenna types used in the simulations are introduced below. In the study of code convergence and validation of next sections, the 1D plasma-wave code is applied to validate the 2D plasma-wave code. Hence, consistent antenna currents must be chosen for the two codes. According to the Fourier expansion of 1D and 2D model, the current density has the relation

$$\sum_m j_\theta^{(2)}\left(r,z,m\right)\exp\left(im\theta\right)=\sum_l\sum_m j_\theta^{(1)}\left(r,l,m\right)\sin\left(\frac{l\pi}{L}z\right)\exp\left(im\theta\right) \tag{6.23}$$

$$\sum_m j_z^{(2)}\left(r,z,m\right)\exp\left(im\theta\right)=\sum_l\sum_m j_z^{(1)}\left(r,l,m\right)\cos\left(\frac{l\pi}{L}z\right)\exp\left(im\theta\right) \tag{6.24}$$

where the superscript 1 and 2 express the current density in the 1D and 2D model, respectively. Selecting a given (l,m) mode, Eq. 6.23 and 6.24 can be simplified to

$$j_\theta^{(2)}\left(z\right)\delta\left(r-r_a\right)=j_\theta^{(1)}\sin(\frac{l\pi}{L}z)\delta\left(r-r_a\right) \tag{6.25}$$

$$j_z^{(2)}\left(z\right)\delta\left(r-r_a\right)=j_z^{(1)}\cos(\frac{l\pi}{L}z)\delta\left(r-r_a\right) \tag{6.26}$$

where δ represents the Dirac delta function. To simplify the validation of the 2D code, and taking into account the linearity of the problem, only in one component, j_θ or j_z, and only one (l,m) mode is considered at each time. All types of antenna can be seen as the sum of these two simple antennas with multiplying coefficients. Therefore, the expression of current density for these two antennas due to Eq. 6.25 and 6.26 can be written as follows:

1. Azimuthal antenna:

$$j_\theta^{(1)}=I_a, \quad j_z^{(1)}=0 \tag{6.27}$$

$$\begin{aligned} j_\theta^{(2)}\left(z\right)\delta\left(r-r_a\right)&=I_a\sin(\frac{l\pi}{L}z)\delta\left(r-r_a\right)\\ j_z^{(2)}\left(z\right)\delta\left(r-r_a\right)&=0\end{aligned} \tag{6.28}$$

2. Axial antenna:

$$j_\theta^{(1)} = 0, \quad j_z^{(1)} = I_a \tag{6.29}$$

$$\begin{aligned} j_\theta^{(2)}(z)\,\delta(r - r_a) &= 0 \\ j_z^{(2)}(z)\,\delta(r - r_a) &= I_a \cos(\frac{l\pi}{L} z)\delta(r - r_a) \end{aligned} \tag{6.30}$$

For the actual 2D simulations of plasma-wave interaction, the Nagoya III antenna shown in Fig. 4.2(a) is chosen to emit the RF wave into the plasma. The current shape function of Nagoya III antenna has been obtained in Chapter 4. Using the Fourier transform in the azimuthal direction in Eq. 4.49, the current density j_z can be described as

$$j_z(r, z, m) = \frac{I_a}{2\pi r_a}(1 - \cos m\pi)\,\delta(r - r_a)\,g(z; z_1, z_2) \tag{6.31}$$

where $g(z; z_1, z_2)$ which has been introduced in Eq. 4.46 describes a uniform function in the range of $(z_1 \leq z \leq z_2)$. z_1 and z_2 represent the position of two ends of antenna. In addition, the azimuthal component of current density j_θ can be easily obtained due to Eq. 4.34.

6.3. Discussion of convergence and validation

In this section, the convergence and validation of the 2D plasma-wave code are carried out and the accuracy of this code will be discussed. The 1D plasma- wave code (HELWAVE1D) which has been discussed in previous chapter is used to validate the 2D plasma-wave code (HELWAVE2D).

The same simulation is set up for both codes, and therefore the analysis is restricted to the type of simulations that the 1D code can tackle. Three different test cases, which include the pure vacuum case (without plasma), the uniform plasma case (plasma density n_0 is a constant) and the non-uniform plasma case (plasma density $n_0 = n_0(r)$), are calculated to verify the HELWAVE2D code.

A regular cylinder helicon source inside a metal chamber from a typical 50W helicon thruster geometry and plasma properties is considered as the input data to carry out in both 1D and 2D codes [15, 44]. The gas used here is argon and the main parameters are summarized in Tab. 6.2

6.3.1. Convergence

A general principle for the numerical convergence of Yee's scheme is that the mesh size must be smaller than half the smallest wavelength. Hence, the mesh sensitivity of the HELWAVE2D code in different situations is investigated.

Fig. 6.2 shows the radial profile of the component of EM fields with the variation of node numbers in the pure vacuum case. The curve convergences when the node number (n_r, n_z) is larger than $(100, 50)$. In this situation the wave field is dominated by transverse electric (TE) and transverse magnetic (TM) modes [107]. The wavelength in vacuum is $2\pi c/\omega$, of the order in the magnitude of meters, much larger than the mesh size used, therefore the speed of convergence is fast.

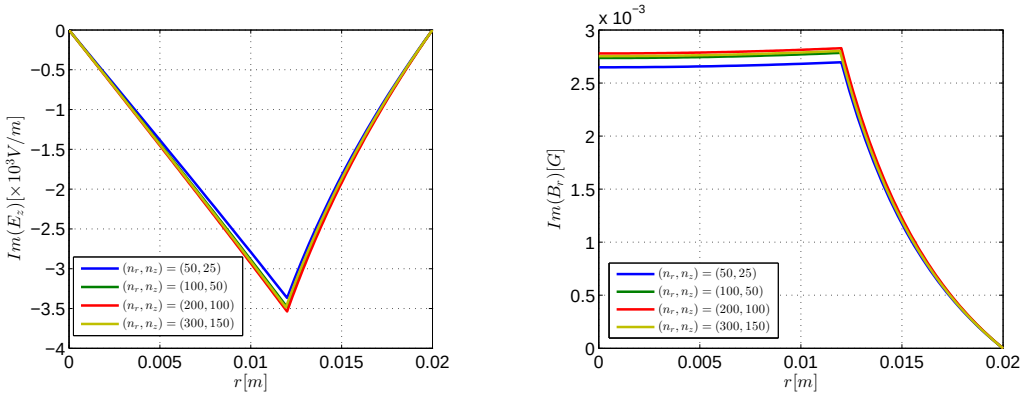

(a) $Im(E_z)$ (b) $Im(B_r)$

FIGURE 6.2: Convergence of wave field profiles in the pure vacuum case at $z = L/4$, $\theta = 0$ and $(l, m) = (1, 1)$. Fig a and b are $Im(E_z)$ and $Im(B_r)$, respectively. (n_r, n_z) represents the node number in r and z direction, respectively.

The convergence in the uniform plasma case at different magnetic fields is demonstrated in Fig. 6.3 and 6.4. At $B_0 = 150G$, the profiles converge quickly. To the contrary, the

Parameter		**Value**
r_p	Plasma radius	0.01 m
L	Plasma and cage axial length	0.1 m
r_w	External cage radius	0.02 m
B_0	Applied magnetic field	150 G
T_e	Plasma temperature	10 eV
n_0	Plasma density	$3.8 \times 10^{18}\ m^{-3}$
ν_e	Electron collision frequency	8.96 MHz
f_{RF}	Frequency of the RF emission	13.56 MHz
r_a	Antenna loop radius	0.012 m
I_a	Antenna current	1 A

TABLE 6.2: Summary of input data for the code validation.

convergence is slow and profiles are still divergent at $B_0 = 600$ G. This is because the wavelength at $B_0 = 600$ is quite small. As we previously mentioned, two general modes named helicon modes and Trivelpiece–Gould (TG) mode propagates in the uniform plasma [55]. The helicon mode has a larger wavelength than the TG mode. Increasing the magnetic field, plasmas go to the surface wave regime which only TG mode can propagate [44]. Therefore, the finer mesh grid should be taken into account in high magnetic field case.

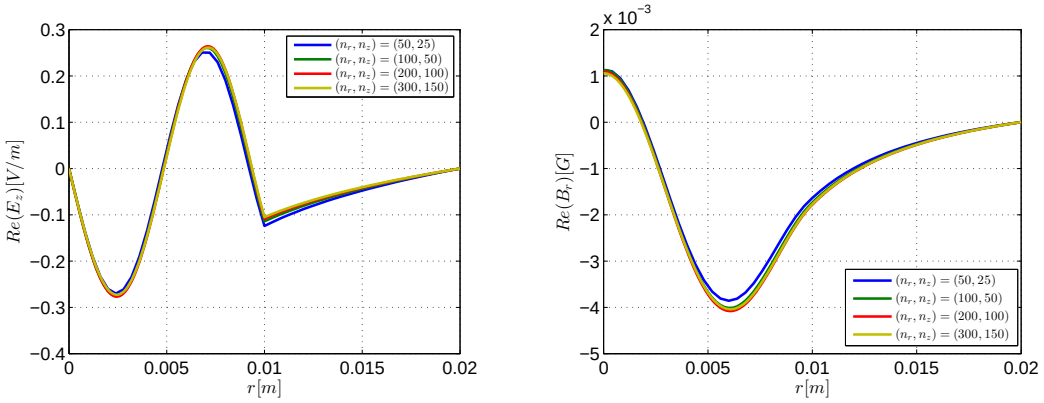

(a) $Re(E_z)$ (b) $Re(B_r)$

FIGURE 6.3: Convergence of wave field profiles in the uniform plasma case at $z = L/4$, $\theta = 0$ and $(l, m) = (1, 1)$. The magnetic field B_0 is $150G$. Fig a and b are $Im(E_z)$ and $Im(B_r)$, respectively. (n_r, n_z) represents the node number in r and z direction, respectively.

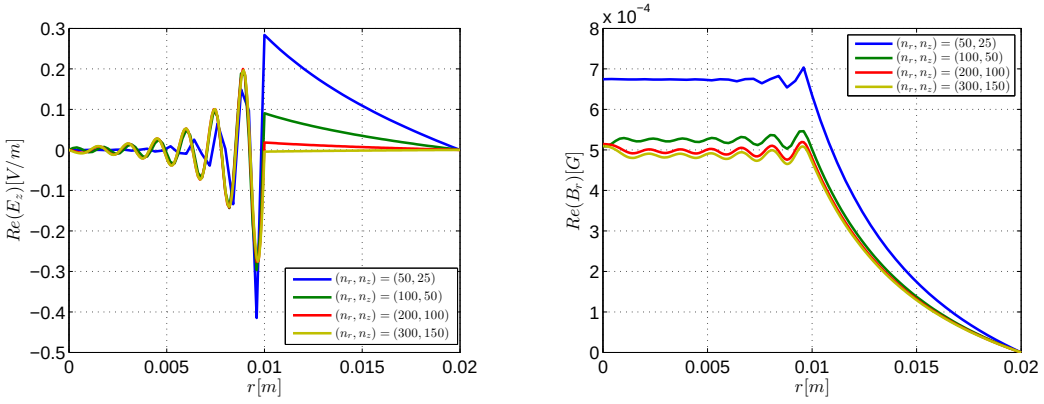

(a) $Re(E_z)$ (b) $Re(B_r)$

FIGURE 6.4: Convergence of wave field profiles in the uniform plasma case at $z = L/4$, $\theta = 0$ and $(l, m) = (1, 1)$. The magnetic field B_0 is $600G$. Fig a and b are $Im(E_z)$ and $Im(B_r)$, respectively. (n_r, n_z) represents the node number in r and z direction, respectively.

6.3.2. Validation

After the discussion of convergence, the validation of HELWAVE2D code is considered. The 1D radially wave code HELWAVE1D is used to benchmark the 2D code.

6.3.2.1. Comparison in the vacuum case

In this part, the comparison between HELWAVE1D code and HELWAVE2D code in the vacuum case is carried out. The radial distribution of wave fields is compared in Fig. 6.5. The calculated results in both codes are consistent. The fields vary sharply at the position of antenna due to the current sheet present there. The 2D plot of the component of EM field in both r and z direction shown in Fig. 6.6 further confirms the consistency between the two codes. The harmonic behaviors is observed in the axial direction.

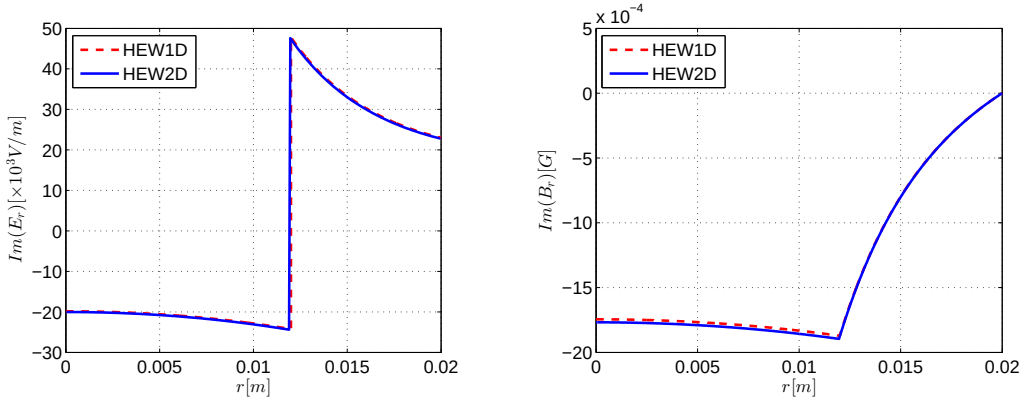

(a) $Im(E_r)$ (b) $Im(B_r)$

FIGURE 6.5: Comparison between HELWAVE1D and HELWAVE2D of wave field profiles in the pure vacuum case at $z = L/3$, $\theta = 0$ and $(l, m) = (2, 1)$. Fig a and b are $Im(E_r)$ and $Im(B_r)$, respectively.

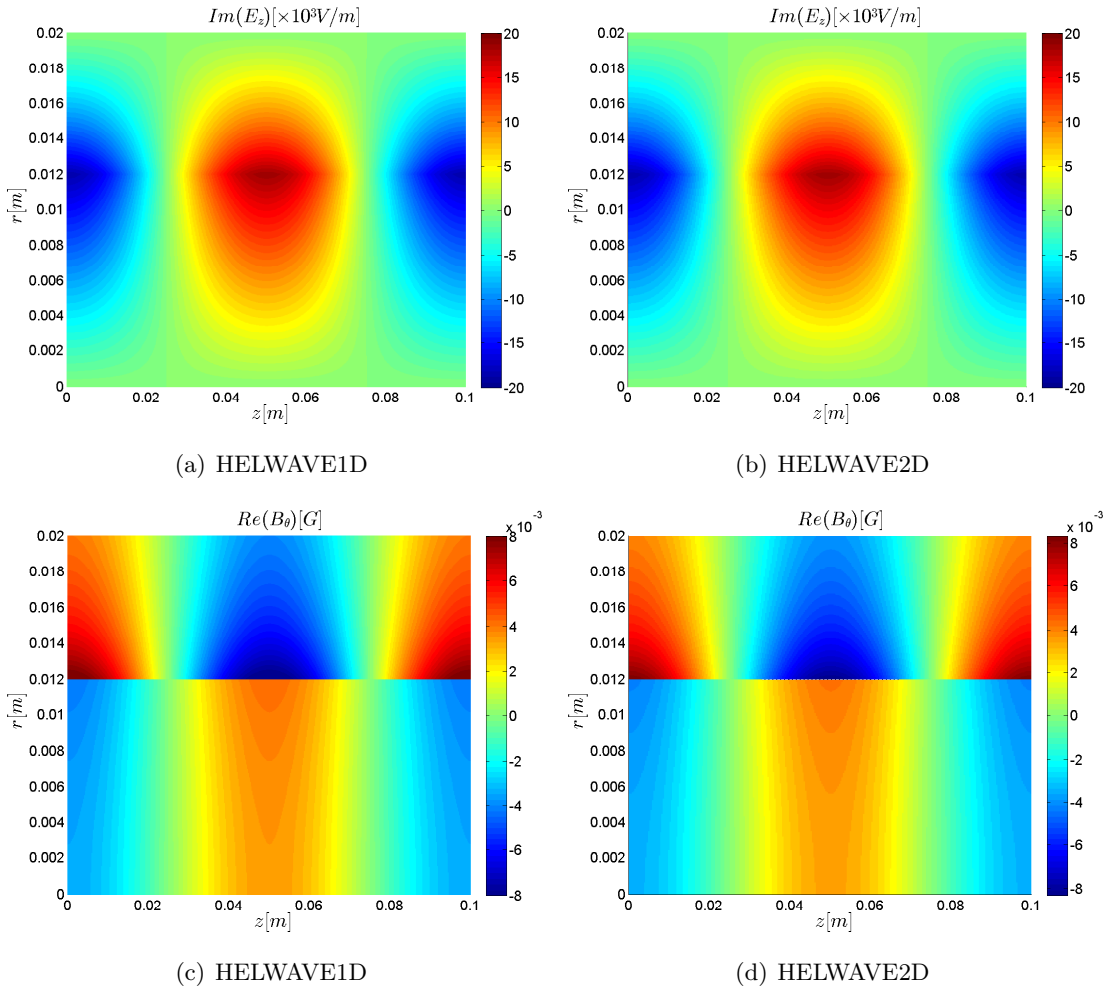

(a) HELWAVE1D

(b) HELWAVE2D

(c) HELWAVE1D

(d) HELWAVE2D

FIGURE 6.6: Comparison of 2D contour of wave field in the pure vacuum case between HELWAVE1D and HELWAVE2D code at $\theta = 0$ and $(l, m) = (2, 1)$.

6.3.2.2. Comparison in the uniform plasma case

Fig. 6.7 shows the validation in the uniform plasma at $B_0 = 150G$. The real part of E_r and B_r is compared between two codes. It is shown that the consistency is not changed whether having plasmas or without plasmas. In this case, waves propagates in the double wave regime and it lead to the helicon mode and TG mode combining with each other.

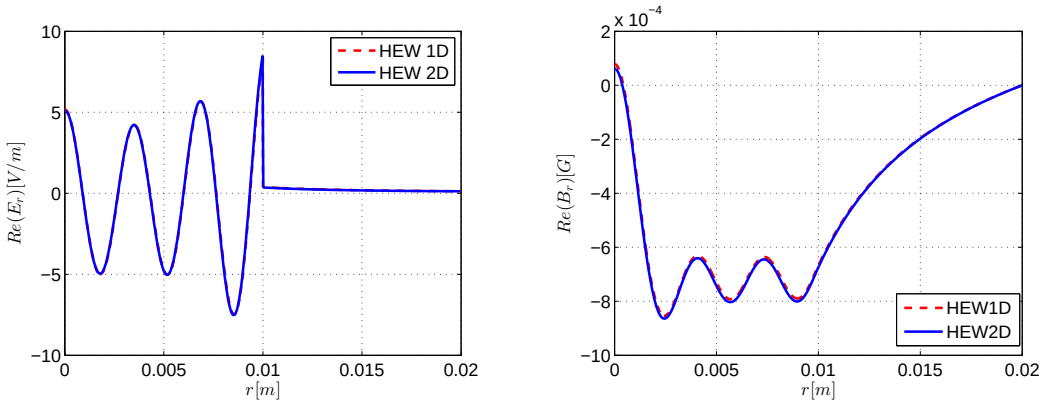

(a) $Im(E_r)$ (b) $Re(B_r)$

FIGURE 6.7: Comparison between HELWAVE1D and HELWAVE2D of wave field profiles in the uniform plasma case at $z = L/3$, $\theta = 0$ and $(l, m) = (2, 1)$. The magnetic field B_0 is $150G$. Fig a and b are $Re(E_r)$ and $Re(B_r)$, respectively.

Comparing the 2D plot in Fig. 6.8, the harmonic behavior is not only in the radial direction, but also in the axial direction. Both codes agree. The reason of this phenomenon is due to the eigenmode forming in the ideally conducting chamber.

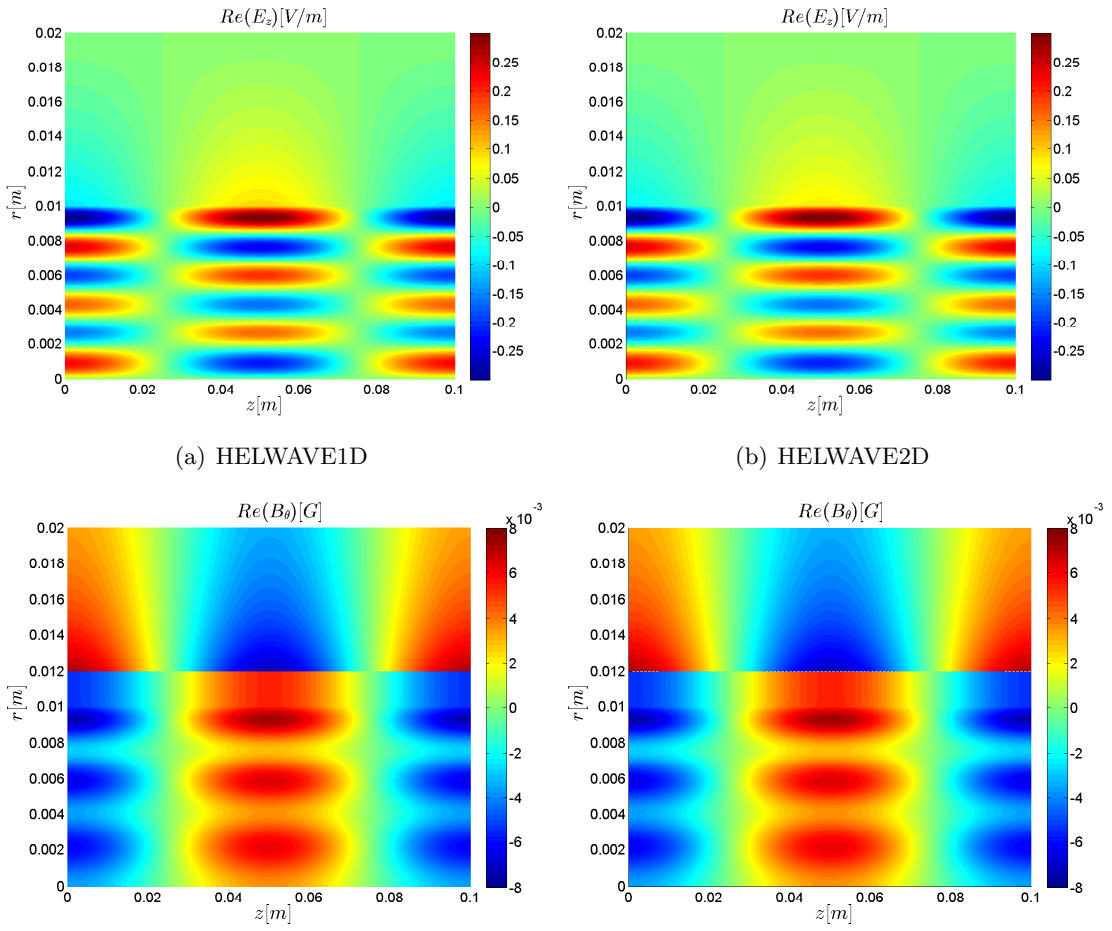

(a) HELWAVE1D (b) HELWAVE2D

(c) HELWAVE1D (d) HELWAVE2D

FIGURE 6.8: Comparison in the uniform plasma case of 2D wave fields in both r and z direction between HELWAVE1D and HELWAVE2D code at $\theta = 0$ and $(l, m) = (2, 1)$. The magnetic field B_0 is $150G$.

In order to confirm the consistency between two codes in more detail, the power deposition in plasmas is compared. The distribution of power absorption in the radial direction is given in Fig. 6.9, showing great agreement. The total power absorbed by plasmas and the plasma resistance is shown in Tab. 6.3. It further proves that the HELWAVE2D has a good accuracy and the error is less than 1% compared to the 1D code.

	Total power (W)	Resistance (Ω)
HELWAVE 1D	1.192×10^{-4}	2.384×10^{-4}
HELWAVE 2D	1.197×10^{-4}	2.394×10^{-4}

TABLE 6.3: Comparison of Total power and resistance.

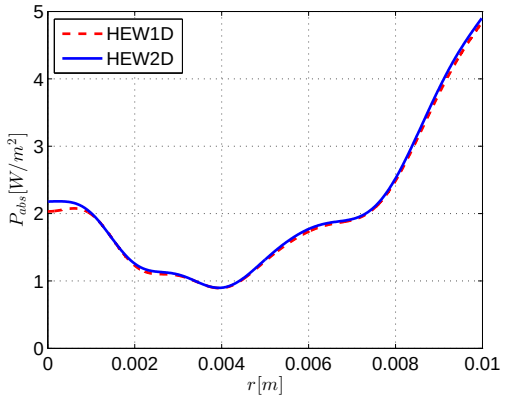

FIGURE 6.9: Comparison of the distribution of power absorption in r direction between HELWAVE1D and HELWAVE2D code in the uniform plasma case at $(l, m) = (2, 1)$. The magnetic field B_0 is $150G$.

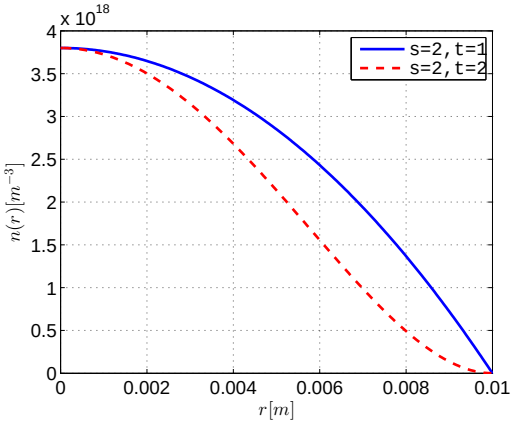

FIGURE 6.10: The density profiles.

6.3.2.3. Comparison in the radially non-uniform plasma case

Generally, the plasma density is not uniform in the HPT. Therefore, the non-uniform plasma case must be investigated. Due to the limitation of 1D code, only radially non-uniform plasma density is taken into account. The radially density profile is assumed to be given by [71]

$$n(r) = n_0 \left[1 - \left(\frac{r}{r_p}\right)^s\right]^t \tag{6.32}$$

Here, $(s, t) = (2, 1)$ and $(s, t) = (2, 2)$ is employed to form density profiles. It is shown in Fig. 6.10.

Similarly, the radial profile of wave fields and 2D plot is applied to validate the 2D code. Fig. 6.11 and 6.12 are the results for $(s, t) = (2, 1)$ and Fig. 6.13 and 6.14 for $(s, t) = (2, 2)$. For these two different density profiles, the results from HELWAVE2D are well consistent with ones from HELWAVE1D. It shows that the HELWAVE2D code

is suitable for calculating complex situations. The density profile strongly influences the wave propagation in the r direction. The harmonic behavior is stronger for the smooth density profile.

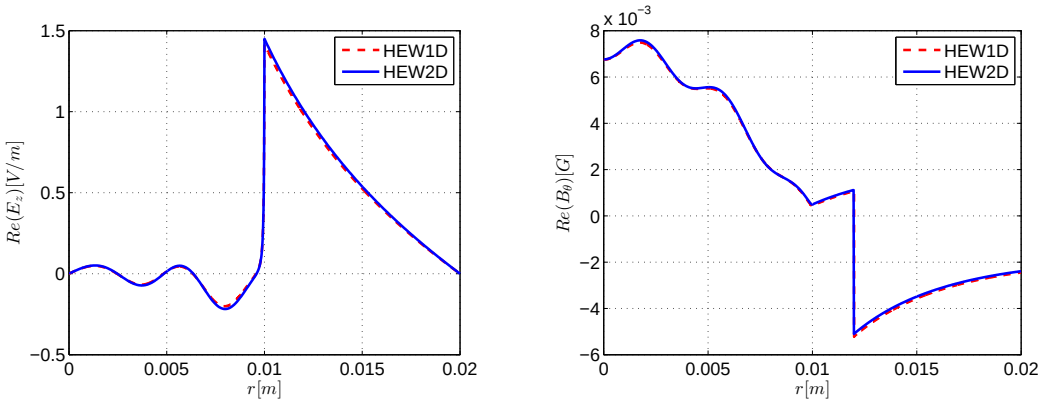

(a) $Re(E_z)$ (b) $Re(B_\theta)$

FIGURE 6.11: Comparison between HELWAVE1D and HELWAVE2D of wave field profiles in the non-uniform plasma case at $z = L/3$, $\theta = 0$ and $(s,t) = (2,1)$, $(l,m) = (2,1)$. The magnetic field B_0 is $150G$. Fig a and b are $Re(E_z)$ and $Re(B_\theta)$, respectively.

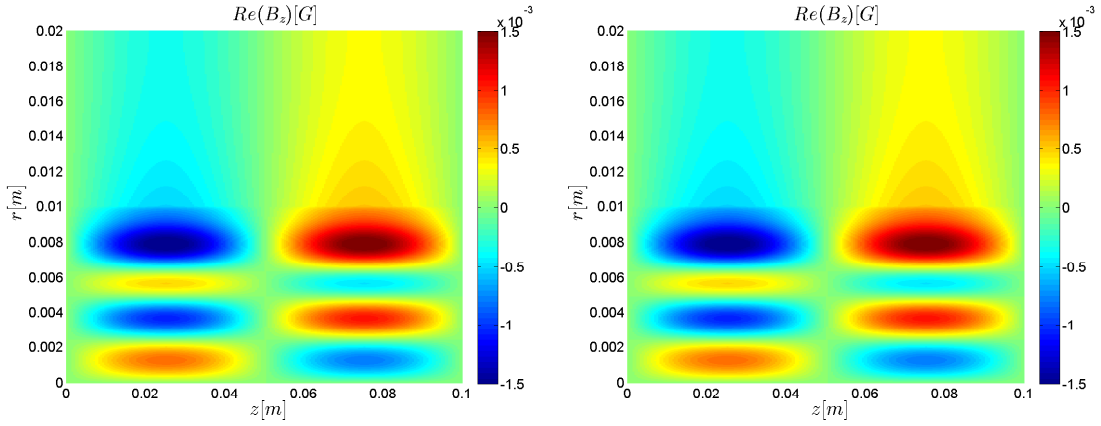

(a) HELWAVE1D (b) HELWAVE2D

FIGURE 6.12: Comparison in the non-uniform plasma case of 2D wave fields in both r and z direction between HELWAVE1D and HELWAVE2D code at $(s,t) = (2,1)$,$(l,m) = (2,1)$ and $\theta = 0$. The magnetic field B_0 is $150G$.

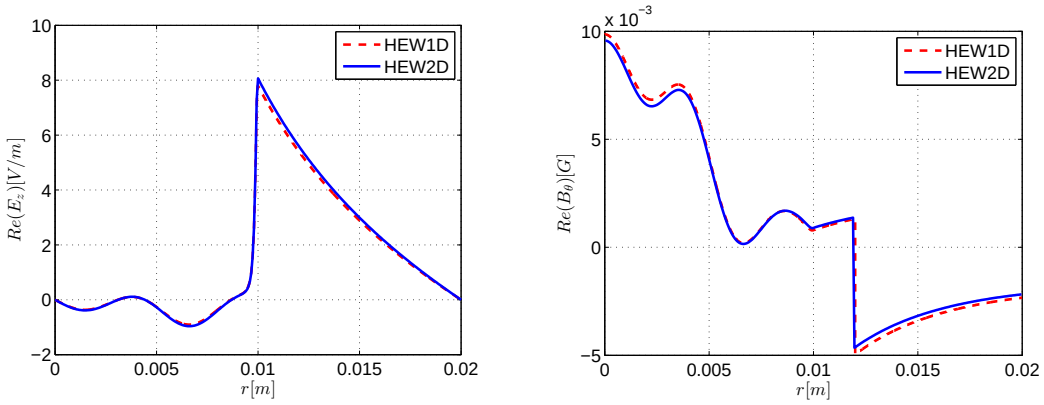

(a) $Re(E_z)$ (b) $Re(B_\theta)$

FIGURE 6.13: Comparison between HELWAVE1D and HELWAVE2D of wave field profiles in the non-uniform plasma case at $z = L/3$, $\theta = 0$ and $(s,t) = (2,2)$, $(l,m) = (2,1)$. The magnetic field B_0 is $150G$. Fig a and b are $Re(E_z)$ and $Re(B_\theta)$, respectively.

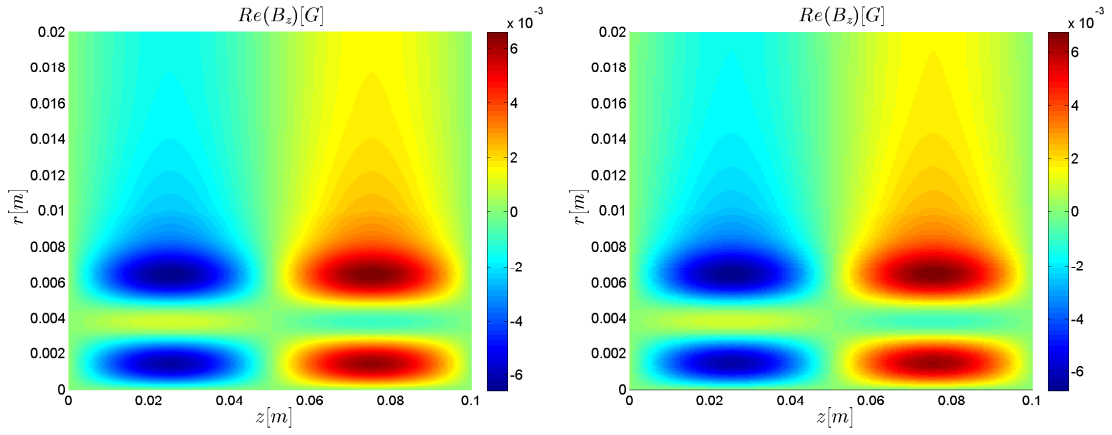

(a) HELWAVE1D (b) HELWAVE2D

FIGURE 6.14: Comparison in the non-uniform plasma case of 2D wave fields in both r and z direction between HELWAVE1D and HELWAVE2D code at $(s,t) = (2,2)$,$(l,m) = (2,1)$ and $\theta = 0$. The magnetic field B_0 is $150G$.

The distribution of power absorption for two different density profiles in the radial direction is shown in Fig. 6.15. The power absorption concentrates near the boundary and few power deposits in the central region. Therefore, it is noted that the density profile has significant influence on the power deposition. The profile $(s,t) = (2,2)$ absorbs more power than $(s,t) = (2,1)$. Tab. 6.4 gives the total power and plasma resistance for these two profiles. The error between 1D and 2D code is again less than 1%.

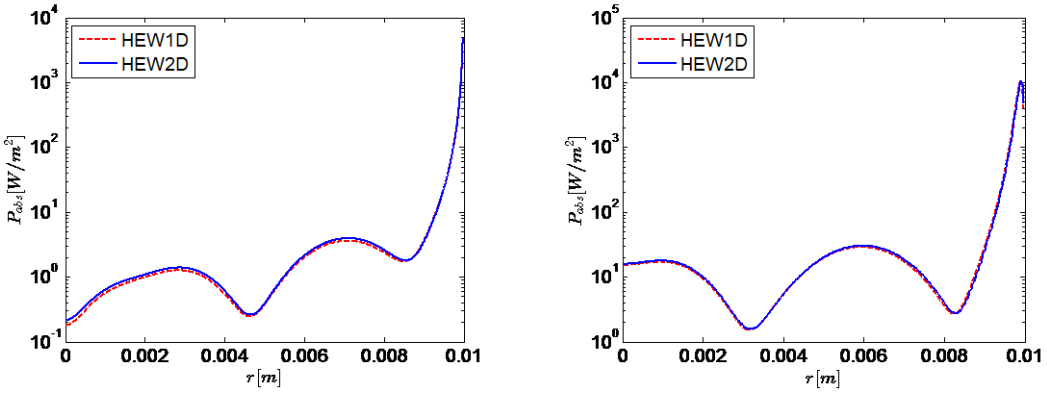

(a) $(s,t) = (2,1)$ (b) $(s,t) = (2,2)$

FIGURE 6.15: Comparison of the distribution of power absorption in r direction between HELWAVE1D and HELWAVE2D code in the non-uniform plasma case for $(l,m) = (2,1)$. The magnetic field B_0 is $150G$. Fig a is $(s,t) = (2,1)$ and Fig b is $(s,t) = (2,2)$.

Code type	$(s,t) = (2,1)$		$(s,t) = (2,2)$	
	Total power(W)	Resistance(Ω)	Total power(W)	Resistance(Ω)
HEW 1D	3.709×10^{-3}	7.418×10^{-3}	0.0204	0.0408
HEW 2D	3.712×10^{-3}	7.424×10^{-3}	0.0205	0.0410

TABLE 6.4: Comparison of Total power and resistance.

6.4. Wave propagation in the presence of a plasma plume

In order to investigate the influence of the plasma plume on the wave propagation and power absorption and the influence of plasma and magnetic field non-uniformity, a typical HPT structure in the vacuum chamber is presented here [44]. Fig. 6.16 shows the schematic structure of a HPT in the vacuum chamber.

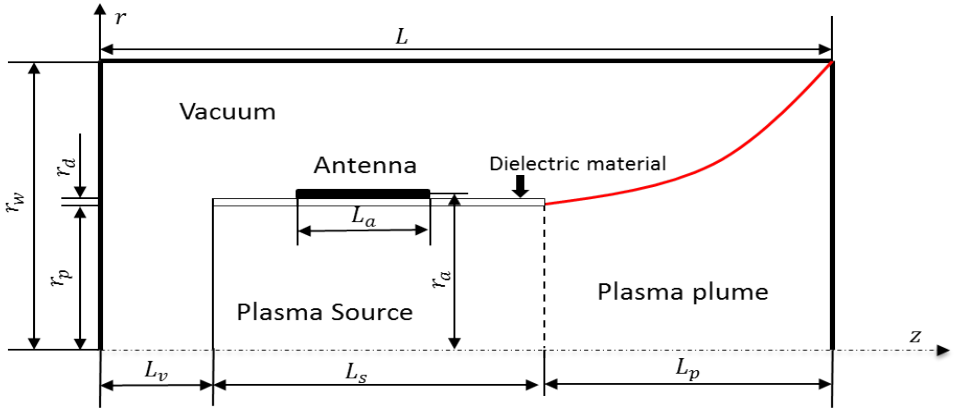

FIGURE 6.16: The structure of simulation

The cylindrical plasma source of a HPT of length $L_s = 0.05$ m and radius $r_p = 0.01$ m is located in the middle of chamber. The plasma plume expands to the vacuum from the exit. To maintain the computational complexity of the problem at an manageable level, only the near region of the plasma plume is taken into account. The length of the plume part is set to $L_p = 0.05$ m. It is assumed that the plasma plume contacts the conducting wall directly in the downstream region. Because the chamber with length $L = 0.15$ m and radius $r_w = 0.02$ m is treated as a perfect conductor, the wave reflection due to the conducting wall influences the wave propagation in the plasma plume. A small vacuum space with length $L_v = 0.05$ m is left on the backside of the plasma source. The Nagoya III antenna with length $L_a = 0.025$ m is located in the vacuum space at $r_a = 0.012$ m and the thickness of antenna wire is assumed to be 0.002 m.

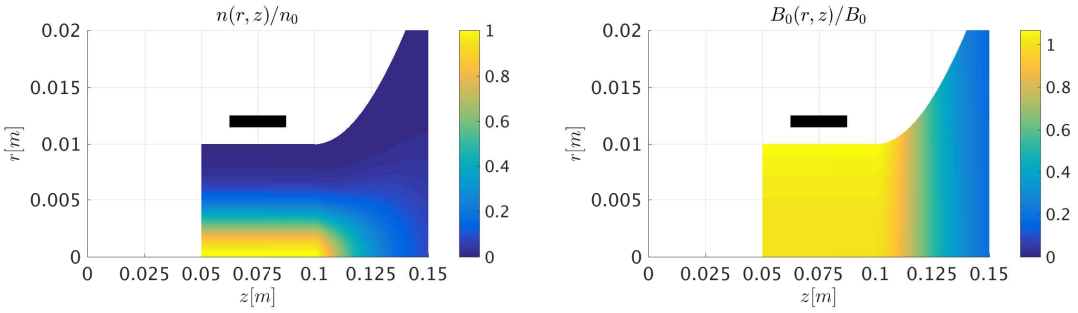

(a) Plasma density

(b) Magnetic field

FIGURE 6.17: The 2D distribution of non-dimensional plasma density and magnetic field. The black box represents the RF antenna

Furthermore, the antenna frequency is set to be 13.56 MHz which is commonly used in helicon research. A normalized antenna current of $I_a = 1$ A is applied. For a short helicon source, we assume that the plasma density is radially non-uniform but axially uniform in the source part and fully inhomogeneous in the plume part. In addition, a Gaussian profile of plasma density is used. The magnetic field in the source part is assumed to be purely axial. In the plasma plume, a divergent magnetic field is taken into account and calculated in terms of a single-loop magnetic coil. The plasma density and magnetic field profiles in the plasma plume are obtained from the 2D magnetic nozzle code DIMAGNO [138]. The contours of the non- dimensional plasma density and magnetic field are shown in Fig. 6.17. An enhanced effective collision frequency is used to enhance the convergence of the code with a limited amount of grid nodes. After observing convergence problems at lower frequencies, an effective electron frequency of 0.1ω is selected as the nominal value for the whole region.

In the following, the simulation results and discussions are presented. The influence of the azimuthal modes m, the magnitude of magnetic field, the effective collision frequency and the influence of plasma plume are investigated in detail.

6.4.1. The azimuthal modes

The antenna impedance versus m for different magnitudes of magnetic fields is given in Fig. 6.18. The plasma density applied here is $n_0 = 3.8 \times 10^8 m^{-3}$. It is found that the resistance and reactance decrease rapidly with increasing $|m|$ for each magnetic field value. Moreover, the resistance of the $m = +1$ mode is much larger than for other modes. At $B_0 = 150$ G, the resistance of $m = +1$ is up to 98% of all modes. Hence, it shows that $m = +1$ mode is the main mode excited by the antenna and dominates the power absorption. This conclusion has been obtained in the regular helicon source case [75, 89]. The consistency implies that the wave propagation in the plasma plume still satisfies the main assumptions of cylindrical plasmas. Additionally, in contrast with the resistance, the symmetric profiles are obtained for the reactance with different m modes. The reactance is less affected by the sign of m.

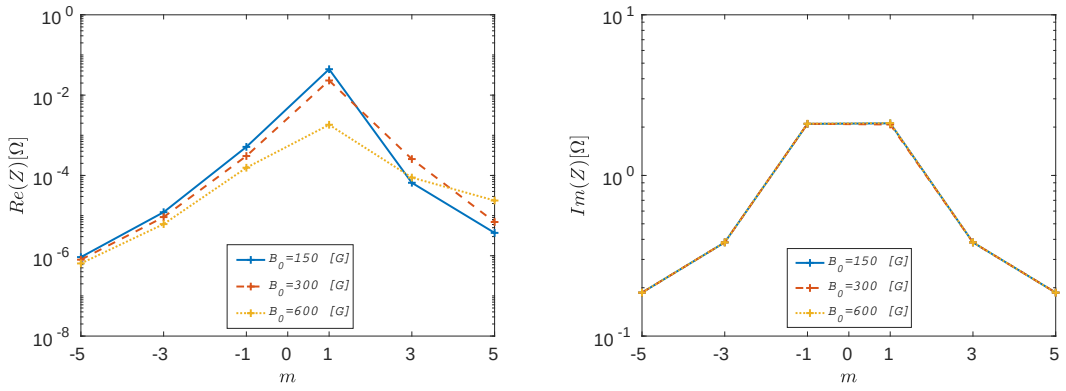

(a) Resistance (b) Reactance

FIGURE 6.18: The impedance varying with m modes for different magnitudes of magnetic fields. The centered plasma density applied here is $n_0 = 3.8 \times 10^8\ m^{-3}$. Fig. a and b represent the resistance and reactance, respectively.

The 2D contour plots of power density for different azimuthal modes at $B_0 = 150$ G are shown in Fig. 6.19. Observe that the radial and axial scales in the plots are different. It is concluded that the power absorption of negative modes is very small and concentrates in the region near the antenna. For the positive m modes, the quasi-periodically local peaks are observed in the bulk of the plasma along the axial direction. The similar phenomenon has been observed in the cylindrical helicon source case [74]. To the contrary, the local peaks of power absorption in the plasma plume tend to follow

the flow of plume along the magnetic lines. According to the cylindrical helicon wave theory, the axial eigenmodes due to the conducting wall of the chamber are the reason to explain the periodically local peaks [73, 74]. It is also confirmed that the positive $m = +1$ mode dominates the power absorption and is strongly coupled to plasmas. This conclusion is consistent with experimental measurements [90, 97] and numerical results [70, 89] for the helicon source.

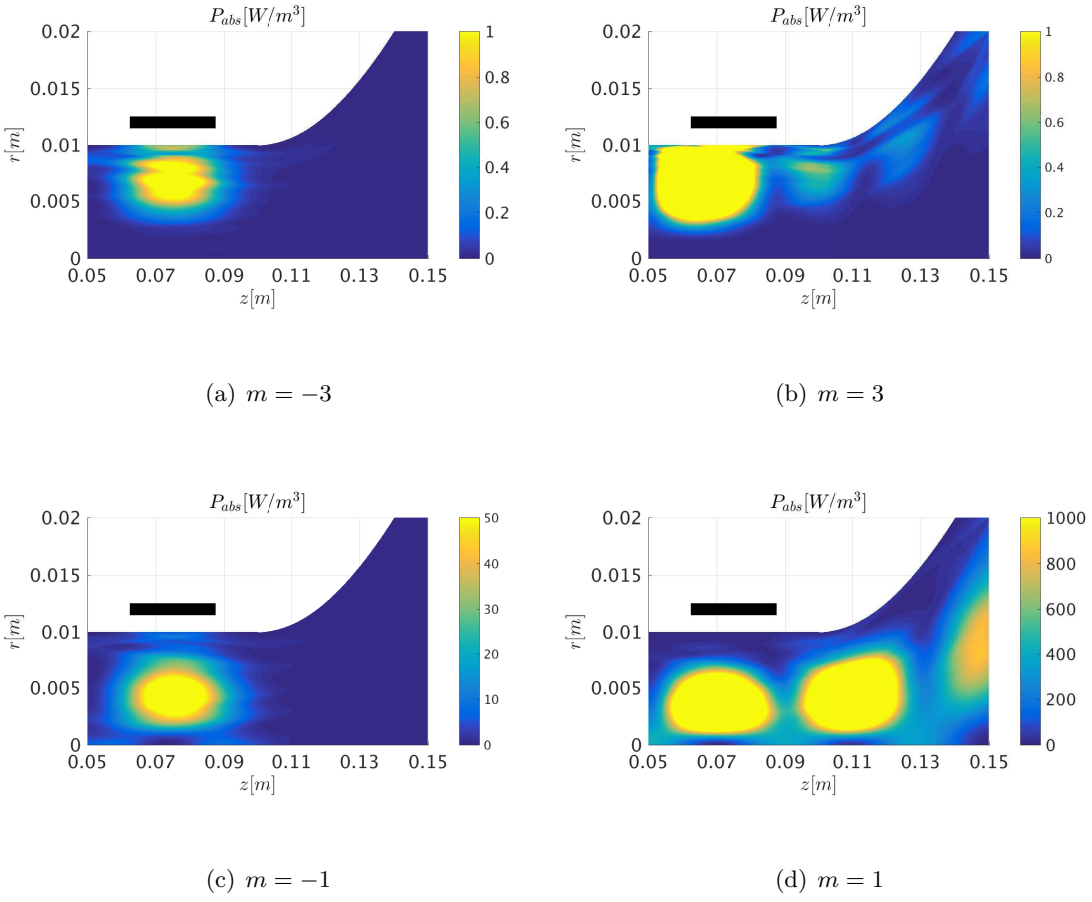

(a) $m = -3$

(b) $m = 3$

(c) $m = -1$

(d) $m = 1$

FIGURE 6.19: The 2D distribution of power absorption for different m modes when $B_0 = 150$ G. The centered plasma density apllied here is $n_0 = 3.8 \times 10^8\ m^{-3}$. The black box represents the RF antenna.

In summary, the $m = +1$ mode is the main mode excited by the antenna and makes the main contribution to the power absorption. Therefore, the other azimuthal modes can be neglected in simulations, and in the following discussion only the $m = +1$ mode is taken into account.

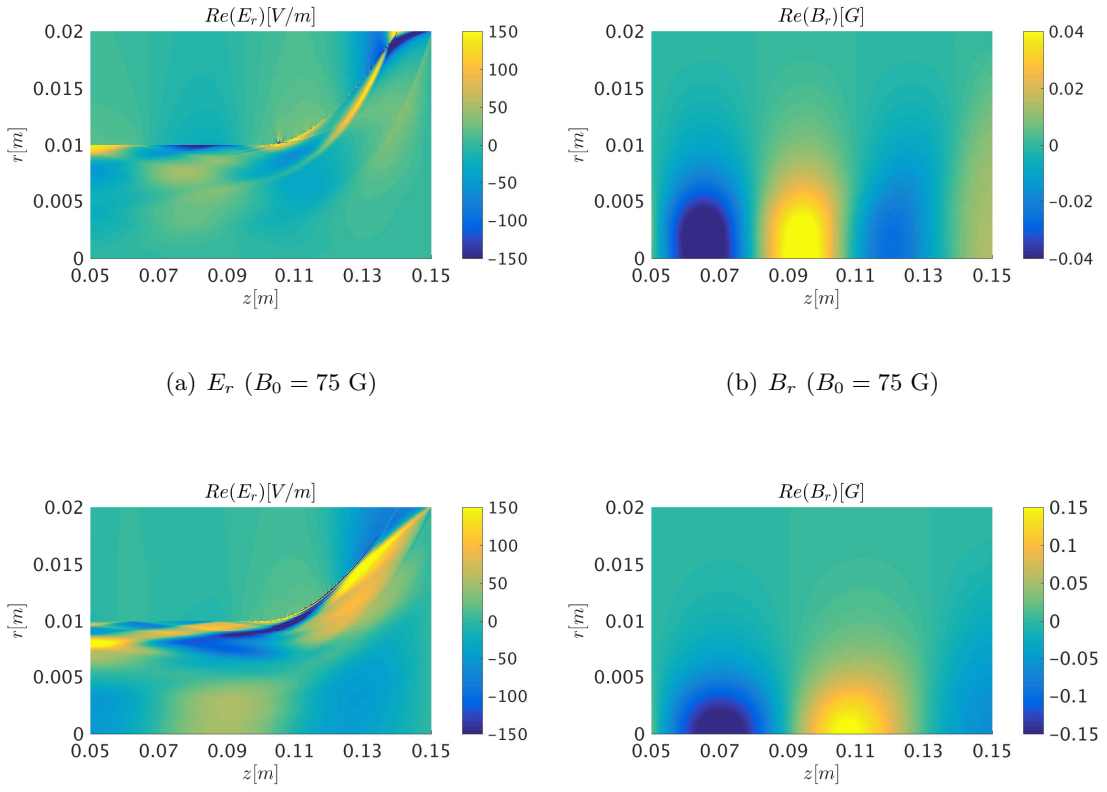

(a) E_r ($B_0 = 75$ G)

(b) B_r ($B_0 = 75$ G)

(c) E_r ($B_0 = 150$ G)

(d) B_r ($B_0 = 150$ G)

FIGURE 6.20: The 2D contour of electromagnetic field for $B0 = 75$ G and $B0 = 150$ G: a, c and b, d present the real part of E_r and the real part of B_r, respectively. The applied central plasma density is $n_0 = 3.8 \times 10^8\ m^{-3}$ and the azimuthal mode is $m = +1$.

6.4.2. The magnitude of the magnetic field

The background magnetic field is one of most important parameters to influence the wave propagation and the performance of HPT. The effects of magnitude of B_0 for cylindrically homogeneous plasmas has been studied in Chapter 5. It is necessary to investigate the characteristics of wave propagation when the non-uniformity and plasma plume are taken into account. In our simulation case, the magnetic field in the source part is purely axial but non-uniform in the radial direction. In the plume part, B_0 is a function of (r, z) and diverges downstream.

Fig. 6.20 and 6.21 shows the 2D plots of wave fields for different magnetic fields. It is found that the wave propagation tends to follow the magnetic lines in terms of the divergence of B_0 in the downstream. This relation has been explained theoretically in Chapter 3. From the E_r fields in Fig. 6.20 and 6.20, the TG mode which has a short wavelength dominates the region near the boundary between plasmas and vacuum. The

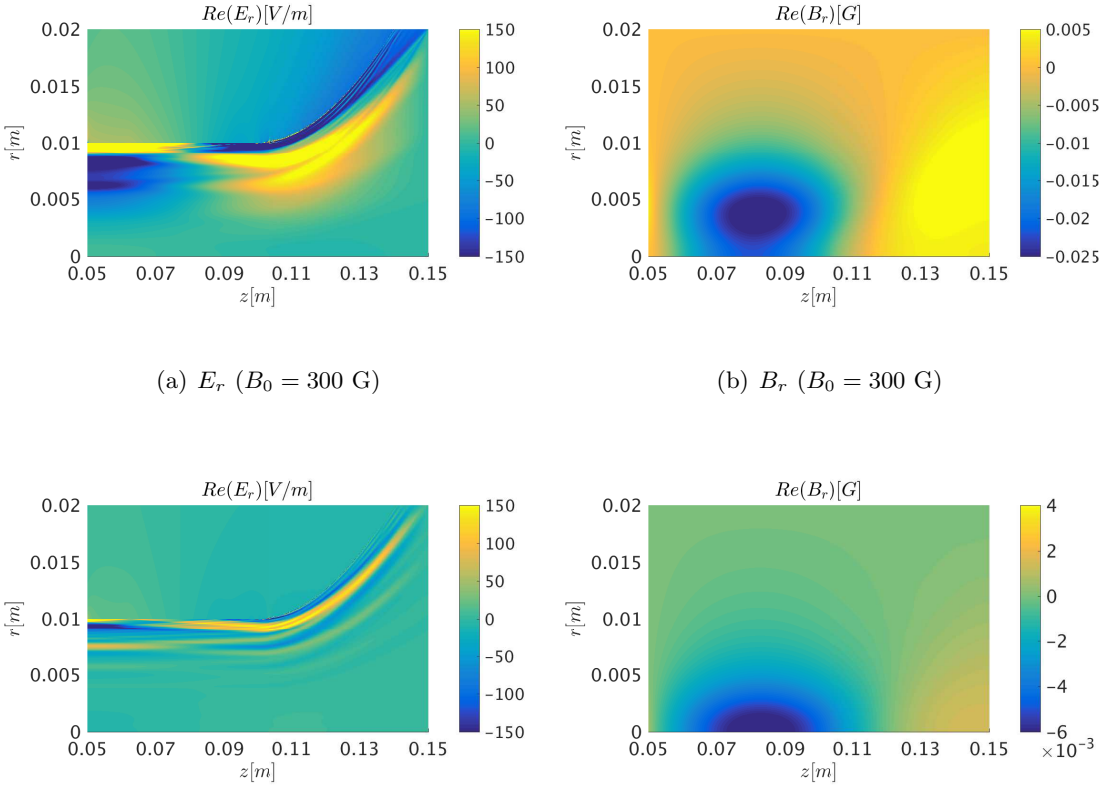

(a) E_r ($B_0 = 300$ G)

(b) B_r ($B_0 = 300$ G)

(c) E_r ($B_0 = 600$ G)

(d) B_r ($B_0 = 600$ G)

FIGURE 6.21: The 2D contour of electromagnetic field for different magnetic field: a and c are the real part of E_r, b and d are the real part of B_r. The applied central plasma density is $n_0 = 3.8 \times 10^8\ m^{-3}$ and the azimuthal mode is $m = +1$.

long wavelength helicon mode mainly propagates in the bulk of the plasma. In addition, the local peaks in the axial direction are visible in the B_r field. With increasing the magnetic field, less and wider local peaks are obtained. At $B_0 = 75$ G, four local peaks are observed and only two can be seen at $B_0 = 600$ G. This phenomenon is related to the parallel wavenumber $k_{\|}$ of the eigenmodes. According to the dispersion relation of axially uniform plasmas, $k_{\|}^2$ is inversely proportional to the ratio ω_{ce}/ω [73]. Therefore, the larger magnetic field leads to a smaller parallel wavenumber and longer parallel wavelength is obtained.

The corresponding power density of Fig. 6.20 and 6.21 are given in Fig. 6.22. The quasi-periodically local peaks related to the $k_{\|}$ are shown clearly in figures. The 'hot' regions which have a high value of power density is consistent with the results we obtained in Fig. 6.20 and 6.21. The power absorption in this case is mainly concentrated in the bulk region of the plasma due to the collisional damping of electrons. It is suggested that the TG mode makes small contribution in this case. From the simulated cases, $B_0 = 150$ G

provides the maximum power deposition.

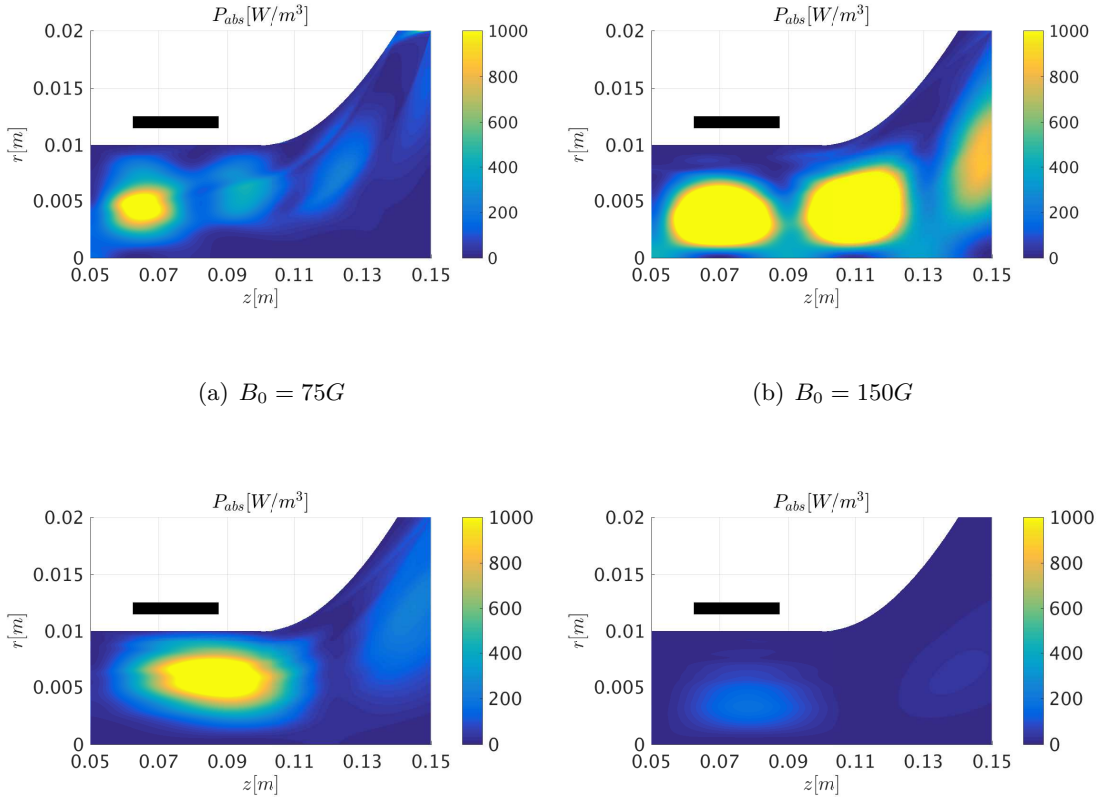

(a) $B_0 = 75G$ (b) $B_0 = 150G$

(c) $B_0 = 300G$ (d) $B_0 = 600G$

FIGURE 6.22: The distribution of power density for different magnetic field. The black box represents the RF antenna. The applied central plasma density is $n_0 = 3.8 \times 10^8\ m^{-3}$ and the azimuthal mode is $m = +1$.

Tab. 6.5 gives the comparison of plasma resistance in different magnitudes of magnetic fields and the contribution of helicon source and plasma plume are presented. It is shown that the power absorption first increase and then decrease with the variation of magnetic fields and reaches the maximum at $B_0 = 150$ G. The contribution of helicon source and plasma plume are comparable though the magnitude of power density in the plasma plume is lower than the helicon source due to the reduction of plasma density and magnetic field. This is because the plume part has a larger volume than helicon source. It is concluded that the wave propagation and power deposition in the near region of plasma plume can not be neglected, and indeed is comparable to the absorption in the source. This observation has strong implications in the power balance (and in the efficiency) of HPT devices.

Magnetic field B_0	Plasma resistance $Re(Z)$		
	Source	Plume	Total
$B_0 = 75$ G	0.0054 (41%)	0.0078 (59%)	0.0132
$B_0 = 150$ G	0.016 (36%)	0.029 (64%)	0.045
$B_0 = 300$ G	0.0144 (49%)	0.0148 (51%)	0.0292
$B_0 = 600$ G	0.0009 (50%)	0.0009 (50%)	0.0018

TABLE 6.5: Comparison of plasma resistance for different magnetic fields. The resistance contributed by the helicon source and plasma plume is presented respectively.

6.4.3. Influence of the collisional frequency

In this section, the effect of effective collision frequency is discussed. The variation of the antenna impedance with the collision frequency for different magnetic fields is shown in Fig. 6.23. It is concluded that the effective collision frequency mainly changes the antenna resistance which highly depends on the power absorption of plasmas and does not affect strongly the antenna reactance. For power absorption it has an optimal value which can provide high resistance. For different magnetic fields, the optimal value of ν_e is varied. The larger the applied magnetic field, the higher ν_e is required to obtain the maximum. However, comparing the value of resistance for different magnetic fields, the influence of B_0 dominates the power absorption when a fixed plasma density profile is taken into account. At $B_0 = 150$ G, the maximum antenna resistance $R = 0.072$ is obtained when $\nu_e/\omega = 0.02$.

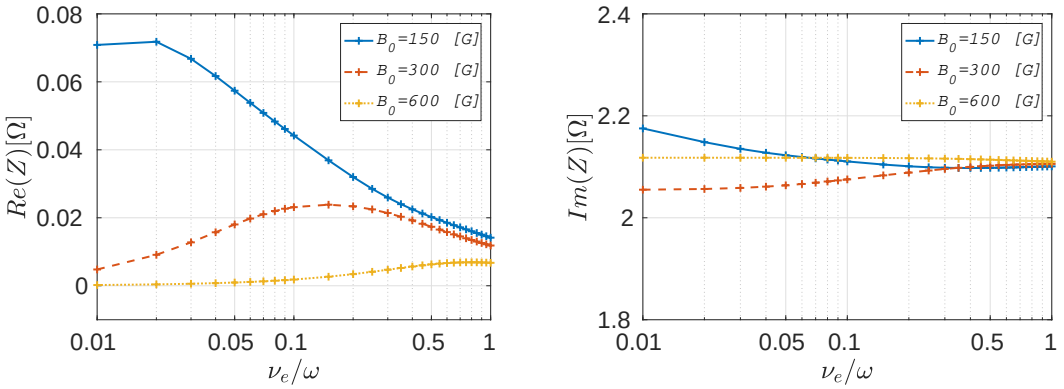

(a) Resistance (b) Reactance

FIGURE 6.23: The impedance varying with effective collision frequency for different magnitudes of magnetic fields. The centered plasma density apllied here is $n_0 = 3.8 \times 10^8\ m^{-3}$ and the azimuthal mode is $m = +1$. Fig. a and b represent the resistance and reactance, respectively.

The 2D plots of power density for different effective collision frequency at $B_0 = 150$ G are shown in Fig. 6.24. The power is mainly absorbed in the bulk region of plasmas due to the collisional damping of electrons. Several periodically local 'hot' regions are presented. At a lower ν_e, the higher magnitude of power density in 'hot' region is obtained. The 'hot' regions in downstream tend to become cooler when a larger ν_e is applied. This is consistent with the results of the trends of plasma resistance in Fig. 6.23. The higher collision frequency leads to less power deposition. It can be concluded that the power deposition cannot be improved by enhancing effective collision frequency when it is beyond the optimal value.

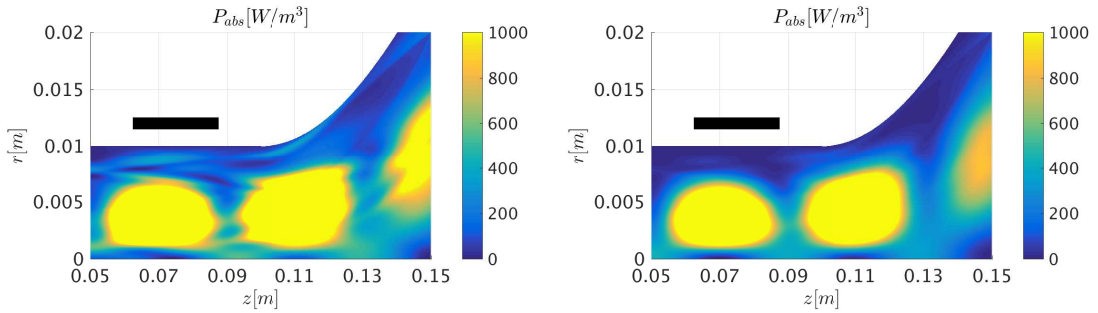

(a) $\nu_e/\omega = 0.05$

(b) $\nu_e/\omega = 0.1$

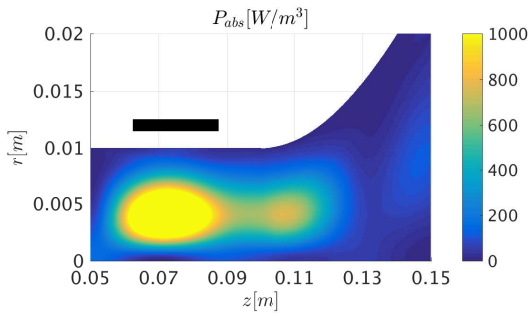

(c) $\nu_e/\omega = 0.5$

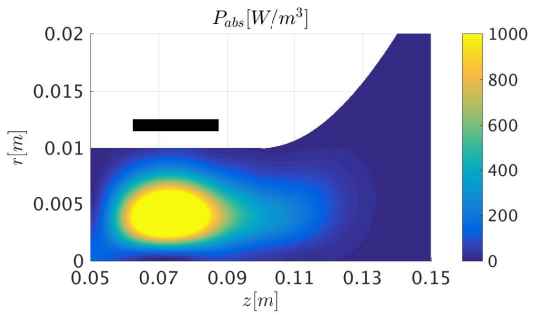

(d) $\nu_e/\omega = 1$

FIGURE 6.24: The distribution of power density for different collision frequency at $B_0 = 150$ G. The black box represents the RF antenna. The centered plasma density apllied here is $n_0 = 3.8 \times 10^8\ m^{-3}$ and the azimuthal mode is $m = +1$.

6.4.4. Comparison with no plume case

Due to previous results, it is suggested that the wave propagation in the plasma plume can be explained by the cylindrical helicon wave theory. It is necessary to study the source case to compare with the source-plume case in order to investigate the influence

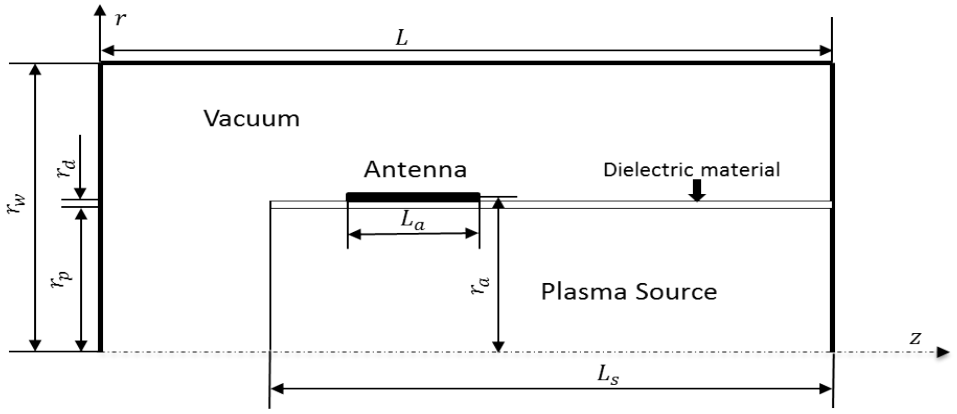

FIGURE 6.25: The source structure of simulation

of plasma plume on the wave propagation. The schematic structure of simulation is shown in Fig. 6.25. The plasma source is expanded to the downstream with the same length as the plasma plume. Therefore, the same plasma density and magnetic field shown in Fig. 6.26 are applied in the whole cylindrical plasma column.

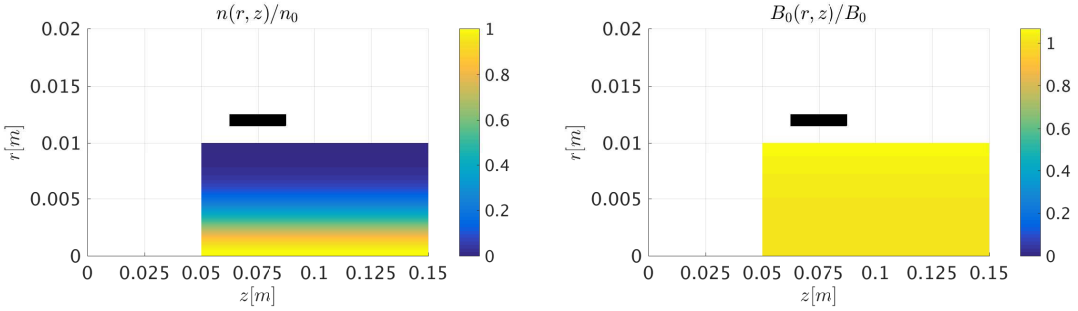

(a) Plasma density

(b) Magnetic field

FIGURE 6.26: The 2D distribution of non-dimensional plasma density and magnetic field in the source case. The black box represents the RF antenna.

The comparison of wave fields between the source case and plume case at $B_0 = 150$ G and $B_0 = 600$ G are shown in Fig. 6.27 and 6.28, respectively. At $B_0 = 150$ G, the harmonic waves in the axial direction are visible. The periodically local peaks are clearly observed in the longitudinal axis in both case. It can be explained by the dispersion relation of helicon waves in a axially uniform plasmas [73, 74]. The short wavelength wave (TG mode) is mainly damped in a narrow layer near the boundary between plasmas and vacuum. Due to the divergence of magnetic fields in the source-plume case, the wave propagates along the magnetic lines and the strength of fields tends to become weaker than the source case in the bulk region in terms of the decrease of n_0 and B_0 in the plasma plume. For $B_0 = 600$ G, the wave propagation is still consistent in both

cases. However, the TG mode dominates the wave propagation. The highly oscillations are observed near the boundary and hardly propagates inside the bulk of plasmas. In addition, the influence of wave reflection due to the conduction wall become small in the source-plume case because of the divergence of magnetic fields.

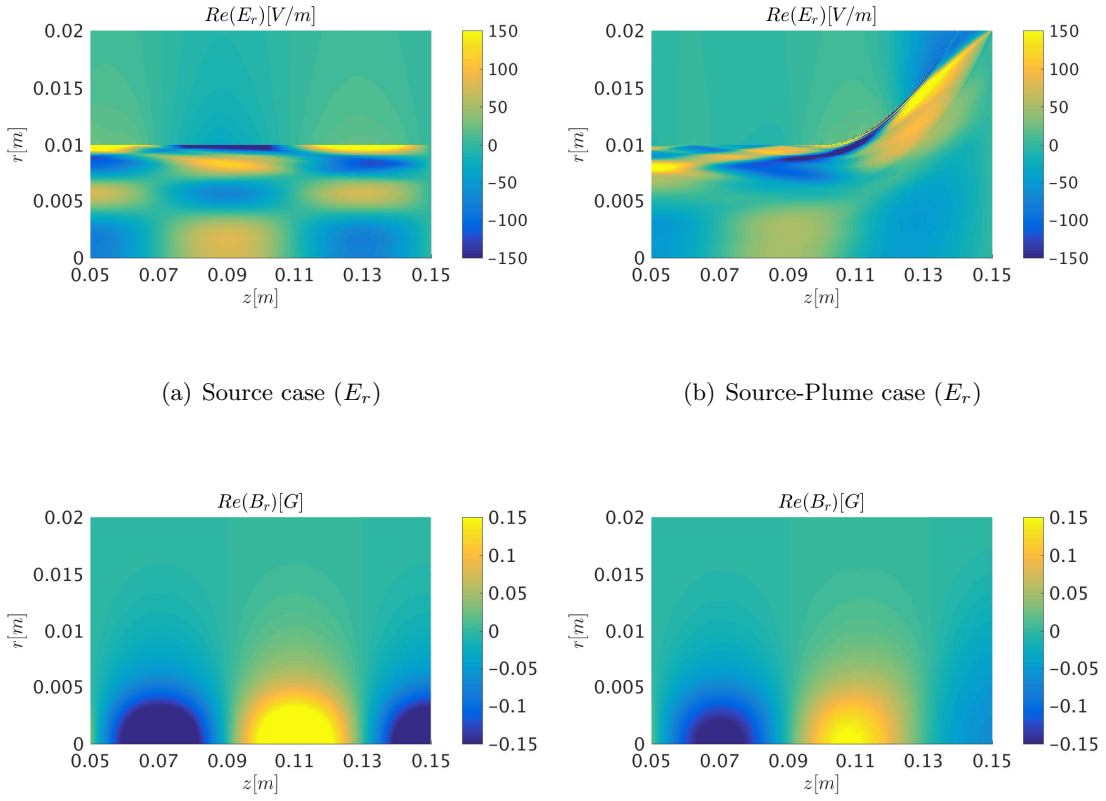

(a) Source case (E_r)

(b) Source-Plume case (E_r)

(c) Source case (B_r)

(d) Source-Plume case (B_r)

FIGURE 6.27: The 2D contour of electromagnetic field for the source case and plume case at $B_0 = 150$ G. Fig. a, b and c, d are the comparison of E_r and B_r, respectively. The applied central plasma density is $n_0 = 3.8 \times 10^8\ m^{-3}$ and the azimuthal mode is $m = +1$.

The comparison of power absorption is shown in Fig. 6.29. The periodically local 'hot' regions inside plasmas due to the eigenmode of metal chamber are visible. With the increment of B_0, the distance between two local peaks are expanded due to the inversely proportional relation of $k_{\parallel}^2$ and ω_{ce}/ω. It is shown that the phenomenon in the source-plume case is consistent with the regular source case. The theory and principle applied in cylindrical helicon sources still can be applicable in the source-plume case. In addition, the decrease of plasma density and magnetic field in the plasma plume take responsibility for the reduction of power absorption. Tab. 6.6 describing the antenna impedance of Fig. 6.29 illustrates this phenomenon.

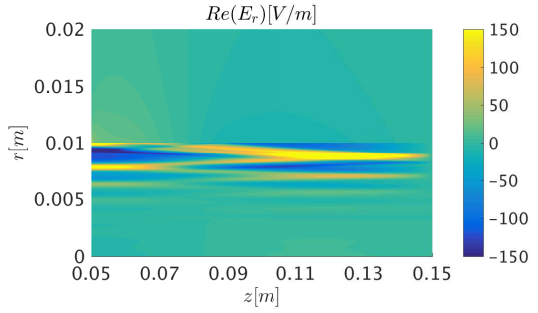

(a) Source case (E_r)

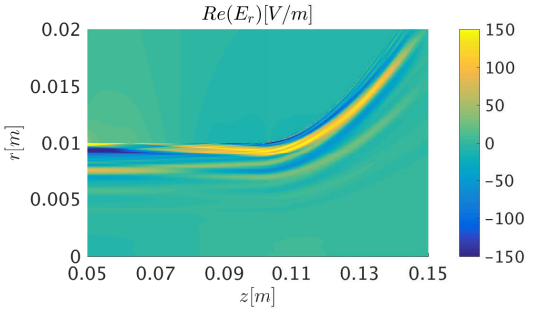

(b) Source-Plume case (E_r)

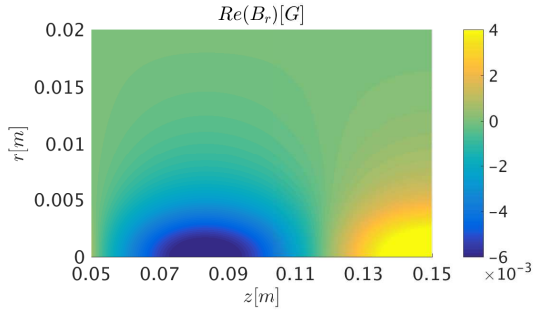

(c) Source case (B_r)

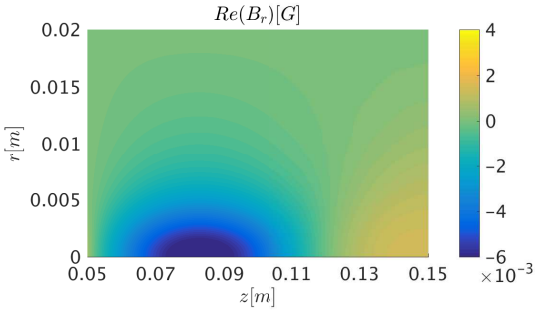

(d) Source-Plume case (B_r)

FIGURE 6.28: The 2D contour of electromagnetic field for the source case and plume case at $B_0 = 150$ G. Fig. a, b and c, d are the comparison of E_r and B_r, respectively. The applied central plasma density is $n_0 = 3.8 \times 10^8\ m^{-3}$ and the azimuthal mode is $m = +1$.

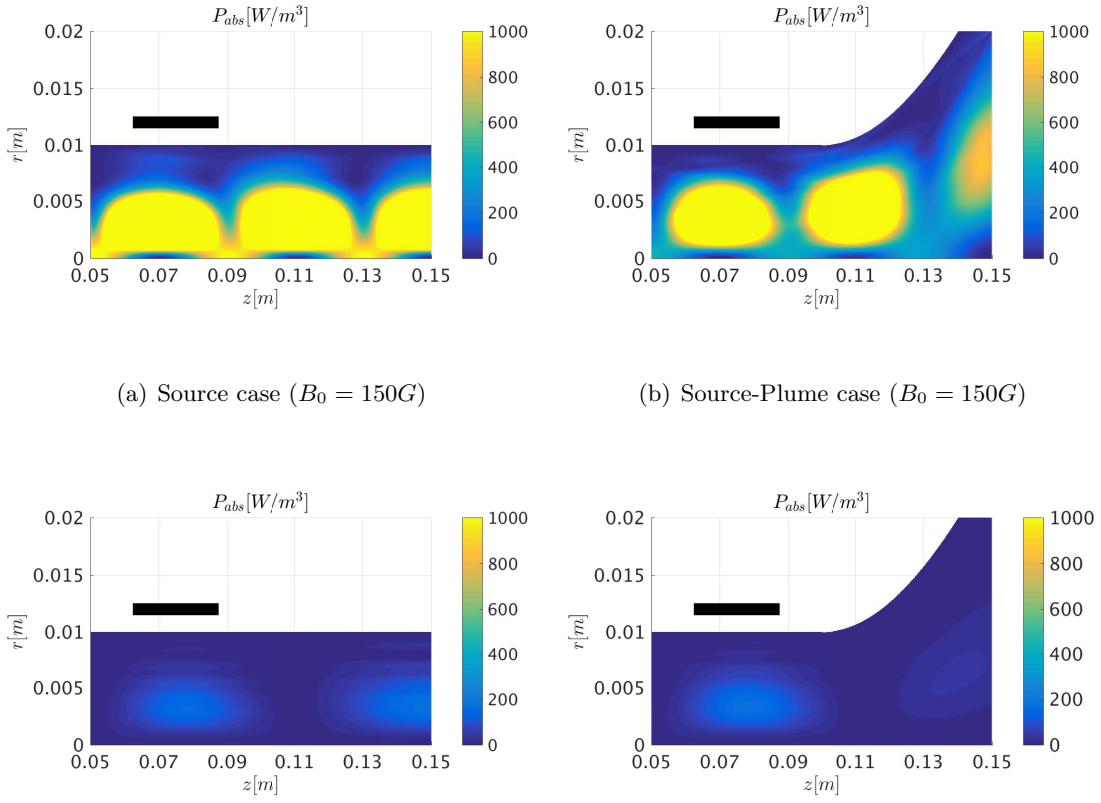

(a) Source case ($B_0 = 150G$)

(b) Source-Plume case ($B_0 = 150G$)

(c) Source case ($B_0 = 600G$)

(d) Source-Plume case ($B_0 = 600G$)

FIGURE 6.29: The distribution of power absorption comparing between source case and plume case for different magnetic fields. The applied central plasma density is $n_0 = 3.8 \times 10^8\ m^{-3}$ and the azimuthal mode is $m = +1$.

Magnetic field B_0	Source case		Source-Plume case	
	$Re(Z)$	$Im(Z)$	$Re(Z)$	$Im(Z)$
$B_0 = 150$ G	0.052	2.12	0.045	2.11
$B_0 = 600$ G	0.0018	2.13	0.0018	2.12

TABLE 6.6: The comparison of antenna impedance for different magnetic fields in both source case and source-Plume case. The resistance and reactance are presented respectively.

6.5. Summary

The 2D plasma-wave interaction model has been described and the corresponding 2D calculation code HELWAVE2D based on the finite difference method has been developed to investigate the influence of the inhomogeneity and the plasma plume on the wave

propagation and power deposition. The staggered grid structure are applied in the code to discretize the EM fields and the ideally conducting boundary condition in the cage wall are considered to close the set of linear equation system.

In order to validate the 2D code, the convergence and the comparison with 1D code which has been previously proved are carried out. It has been concluded that the characteristics of convergence depends on the wavelength in plasmas. The general law is that the cell size which is used in the simulation must be smaller than the local wavelength so that it can capture all the information of waves. In addition, the comparison between 1D and 2D code has been implemented in three general situations including the pure vacuum case, the uniform density case and the radially non-uniform density case. It is confirmed that the 2D code has a good consistency with 1D code and can be applied in different parametric situations.

Then, the 2D simulation of plasma-wave interaction including the source and plume region are implemented. It is proved that the $m = +1$ mode is mainly excited by the antenna and dominates the power absorption. The periodically local peaks of wave fields and power density in the axial direction due to the eigenmode of conducting wall are observed. With increasing the magnetic field, the distance of local peaks become larger. It is because the inversely proportional relation between the $k_{\parallel}^2$ and ω_{ce}/ω according to the dispersion relation in axially uniform helicon plasmas. In addition, the resistance of the source part and the plume part are comparable. It means that the power absorption does not mainly concentrate in the plasma source and it is not very beneficial for the propulsion. To investigate the effective collision frequency, it is concluded that it has an optimal collision frequency that provide the maximum power absorption. For different magnetic fields, the larger magnetic field is applied, the larger collision frequency is needed to obtain the maximum. The comparisons between the regular source case and source-plume case are carried out in order to evaluate the influence of the plasma plume. It is shown that the cylindrical helicon plasma theory still satisfies in the plasma plume. The waves tend to propagate along the magnetic lines due to the divergence of the magnetic field in the plasma plume. The reduction of magnitude of the plasma density and magnetic fields take the responsibility to the decrease of power deposition in the plume part.

Chapter 7

Conclusions

This Thesis has performed an extensive literature review of the state of the art in wave-plasma modelling and the present understanding of the physical mechanisms involved in it, and it has then developed and validated a plasma-wave interaction code and used it to characterize the power deposition and the impedance of a helicon plasma thruster.

In order to improve the performance of helicon plasma thrusters and guide their design, it is necessary to understand the physical process of plasma-wave interaction which plays a significant role in HPT. To this end, the literature review in the first part of the thesis helped define the starting point for the modelling contribution of this Thesis, taking into account the existing progress in the theoretical, experimental and numerical research of helicon plasma sources and thrusters.

A general wave model in cold magnetized plasmas was then described to give a general frame to analyse the Helicon and companion waves, discussing the different parametric regimes for wave propagation and characterization. Based on this discussion, the two-dimensional (2D) wave model and one-dimensional (1D) wave model suitable for practical HPT configurations were derived with a clear set of assumptions and boundary conditions.

Based on the 0D dispersion relation and 1D wave model, an analysis was conducted on the influence following parameters: (a) magnetic field strength, (b) excitation frequency, (c) plasma column length and density (and ion type), (d) shape of the exciting antenna, (e) axial location and length of the antenna, and (f) relative radius of the antenna and the relative radius of the external conducting cage.

Two families of antenna shapes, the double-saddle family and the helical family were explored. The Nagoya III antenna is the common case connecting the two families. For the double saddle family, plasma resistance increases with the angle of the antenna arcs.

With the goal of maximizing the resistance of the equivalent circuit, the Nagoya III antenna is the best choice within that family. A central location and an antenna length of about half of the plasma column yield the highest values of plasma resistance. The behaviour of the helical family is more complex. Starting from the Nagoya III antenna, plasma resistance tends to increase with the number of turns of the helical segments but it requires using longer antenna lengths. The analysis points out that optimal helical antennas would have between 1 and 2 turns and would have axial lengths larger than one-half of the plasma column.

Plasma resistance is highest when the antenna radius is close to the plasma radius. Also, the resistance increases when the radius of the external cage increases, revealing an important role of the size of the resonance cavity, reaching an asymptotic behaviour for cage radius above 1.5 times the antenna radius.

The combined influence of the antenna frequency, the plasma column length, the magnetic field strength, and the plasma density depends on two dimensionless parameters. The first one is the ratio between the RF ω and the electron-cyclotron frequency (the latter being proportional to the magnetic field). The second parameter involves the chamber length (that is the maximum axial wavelength that can be accommodated in the plasma column) and the plasma density. These two dimensionless parameters define three distinct parametric regions in the CMA diagram: the inductively-coupled regime, for weak enough magnetic fields; the double wave regime, when both the helicon and the TG modes propagate through the plasma column; and the single wave regime, for large magnetic fields or small plasma densities, when only the TG mode propagates next to the plasma edge.

Plasma resistance is found to be highest within the double-wave regime (which would correspond to the nominal helicon or 'blue mode' in the literature). Furthermore, approximate scaling laws among the above parameters have been defined for achieving optimal resistance. These laws establish a proportional dependence between optimal plasma resistance and any of the parameters: antenna frequency, magnetic field, and density. Since plasma resistance presents multiple peaks when these parameters are varied, an important design requirement is to set the nominal condition in a parametric interval where resistance peaks are not very narrow. This applies mainly to plasma density, which is the less controllable parameter.

A change of wave regime takes place when the antenna frequency equals the lower hybrid frequency, which introduces the influence of the propellant type through the ion-to-electron mass ratio. High peaks of resistance are found when the RF is below the lower hybrid frequency, but these peaks are quite narrow and the wave does not propagate deep inside the plasma column. Hence, and although more research would be

required for this lesser-known regime, keeping the RF above the lower hybrid frequency is deemed advisable.

The successful cross-validation between 1D and 2D codes provides confidence in the correctness of both integrators. The 2D wave model with its Yee's finite difference scheme has enabled investigating the influence of having inhomogeneous plasma properties in the source, and of the presence of an expanding plasma plume outside of it.

Regarding the former, it has been observed that the radial profile of the plasma density has a profound effect on wave propagation and absorption, potentially blocking the propagation of the wave into the central part of the plasma column. Thus, a large dependency on power absorption and resistance depends on this otherwise secondary factor.

Regarding the latter, the comparison between the source-only case and source- and-plume case showed that the cylindrical helicon plasma theory is still satisfied in the plasma plume. However, the waves propagate along the magnetic lines due to the divergence of the magnetic field into the plasma plume. This is enabled by the comparable drop of magnetic field strength and plasma density in the region of the plume. Noticeable absorption and takes place in the plume region for this reason, which is undesirable for propulsion, where power should be absorbed upstream to maximize the efficiency of the device. Also, this hints at the possibility of a fraction of the wave power escaping downstream and out of the plasma, with the consequent additional efficiency loss. A clever magnetic field design that creates a constriction at the magnetic throat to better control the drop of plasma density could potentially improve this situation, but that analysis is left for future work. It has been shown that the $m = 1$ mode is main one excited by the antenna and dominates the power absorption. Periodic local peaks of electric field and power absorption in the axial direction due to the dominant eigenmode in the resonant cavity are observed. With increasing the magnetic field, the distance between local peaks becomes larger. This is due to the inversely proportional relation between the $k_{\parallel}^2$ and ω_{ce}/ω according to the dispersion relation in axially uniform helicon plasmas. Regarding the effect of the collision frequency, it is concluded that it has an optimal collision frequency that provide the maximum power absorption. Also, it is observed that the larger the magnetic field, the larger the collision frequency is needed to obtain the maximum.

Lastly, the following lines of future work have been identified:

1. Investigate the propagation of the plasma wave in an open space with the implementation of absorbing boundary conditions. While the case covered in the

present Thesis is relevant for the operation of a helicon plasma source in the vacuum tank of a laboratory, the operation in space will introduce the possibility of losing a fraction of the wave as radiation into empty space. This improvement in the code capabilities will allow the quantification of this fraction, and the study of countermeasures to minimize it (e.g. a Faraday cage around the thruster).

2. Improve the implementation of the 2D code with a compiled programming language for speed and memory efficiency, like Fortran.

3. Couple the plasma-wave model with a plasma-dynamic code to iteratively find the self-consistent solution of the plasma density, electron temperature, and power absorption. This effort is planned for future implementation, with the combination of the 2D wave code with other existing codes in the EP2 research group (Hyphen code).

4. Extend the analysis to other frequency domains, such as the neighborhood of the electron-cyclotron resonance (ECR). This is relevant for the analysis of other propulsive devices that are recently being developed, in particular for ECR thrusters which has a similar geometrical configuration to the helicon plasma thruster but operates in the several GHz range with magnetic fields in the order of 900 G.

5. Explore the importance of electron thermal effects and non-linear effects on the propagation and absorption of the wave. This line of development will go beyond the linear, cold-plasma-tensor model employed in the present analysis. However, while non-linear absorption mechanisms are expected to be important in other devices like the ECR thruster, helicon wave absorption is deemed be well-represented by linear models.

Bibliography

[1] Malcolm Macdonald and Viorel Badescu. *The international handbook of space technology*. Springer, 2014.

[2] Robert G Jahn. *Physics of electric propulsion*. New York : McGraw-Hill, 1968.

[3] Eduardo Ahedo. Plasmas for space propulsion. *Plasma Physics and Controlled Fusion*, 53(12):124037, 2011.

[4] Dan M Goebel and Ira Katz. *Fundamentals of electric propulsion: ion and Hall thrusters*, volume 1. John Wiley & Sons, 2008.

[5] Be-4 rocket engine. http://spacenews.com/wp-content/uploads/2015/01/BE4_BlueOrigin.jpg.

[6] Pps1350-e plasma thruster. http://teqbrief.com/media/Space/pps1350-E-350-opt.jpg.

[7] R. G. Jahn and E. Y. Choueiri. Electric propulsion. *Encyclopedia of Physical Science and Technology*, 3, 2002.

[8] Electric propulsion versus chemical propulsion. http://sci.esa.int/smart-1/34201-electric-spacecraft-propulsion/?fbodylongid=1534.

[9] Edgar Y Choueiri. A critical history of electric propulsion: The first 50 years (1906-1956). *Journal of Propulsion and Power*, 20(2):193–203, 2004.

[10] RH Goddard. The green notebooks, vol. 1. *The Dr. Robert H. Goddard Collection at Clark University Archives, Clark University, Worceseter, MA*, 1610, 1906.

[11] Ernst Stuhlinger. *Ion propulsion for space flight*. McGraw-Hill New York, 1964.

[12] M Martinez-Sanchez and James E Pollard. Spacecraft electric propulsion-an overview. *Journal of Propulsion and Power*, 14(5):688–699, 1998.

[13] F Cannat, T Lafleur, J Jarrige, P Chabert, P-Q Elias, and D Packan. Optimization of a coaxial electron cyclotron resonance plasma thruster with an analytical model. *Physics of Plasmas (1994-present)*, 22(5):053503, 2015.

[14] Michael D West, Christine Charles, and Rod W Boswell. Testing a helicon double layer thruster immersed in a space-simulation chamber. *Journal of Propulsion and Power*, 24(1):134–141, 2008.

[15] Eduardo Ahedo and Jaume Navarro-Cavallé. Helicon thruster plasma modeling: Two-dimensional fluid-dynamics and propulsive performances. *Physics of Plasmas (1994-present)*, 20(4):043512, 2013.

[16] Sabrina Pottinger, Vaios Lappas, Christine Charles, and Rod Boswell. Performance characterization of a helicon double layer thruster using direct thrust measurements. *Journal of Physics D: Applied Physics*, 44(23):235201, 2011.

[17] Timothy Ziemba, John Carscadden, John Slough, James Prager, and Robert Winglee. High power helicon thruster. In *41st AIAA/ASME/SAE/ASEE Joint Propulsion Conference & Exhibit*, page 4119, 2005.

[18] Francis F Chen. Helicon discharges and sources: a review. *Plasma Sources Science and Technology*, 24(1):014001, 2015.

[19] Jaume Navarro, M Merino, and Eduardo Ahedo. A fluiddynamic performance model of a helicon thruster. In *48th AIAA/ASME/SAE/ASEE Joint Propulsion Conference & Exhibit*, page 3955, 2012.

[20] E Ahedo and M Merino. Two-dimensional supersonic plasma acceleration in a magnetic nozzle. *Physics of Plasmas (1994-present)*, 17(7):073501, 2010.

[21] Eduardo Ahedo. Plasma dynamics in a helicon thruster. In *Progress in Propulsion Physics*, volume 4, pages 337–354. EDP Sciences, 2013.

[22] Jaume Navarro Cavalle. *Plasma Simulation In Space Propulsion: The Helicon Plasma Thruster*. PhD thesis, Universidad Politecnica de Madrid, 2016.

[23] C Charles, RW Boswell, and MA Lieberman. Xenon ion beam characterization in a helicon double layer thruster. *Applied physics letters*, 89(26):261503, 2006.

[24] Kazunori Takahashi, Trevor Lafleur, Christine Charles, Peter Alexander, and Rod W Boswell. Electron diamagnetic effect on axial force in an expanding plasma: experiments and theory. *Physical review letters*, 107(23):235001, 2011.

[25] Oleg V Batishchev. Minihelicon plasma thruster. *IEEE Transactions on plasma science*, 37(8):1563–1571, 2009.

[26] Timothy Ziemba, John Slough, Robert Winglee, Mohamed S El-Genk, and Mary J Bragg. High power helicon propulsion experiments. In *AIP Conference Proceedings*, volume 746, pages 965–975. AIP, 2005.

[27] Francis F Chen and Rod W Boswell. Helicons-the past decade. *Plasma Science, IEEE Transactions on*, 25(6):1245–1257, 1997.

[28] RW Boswell. Plasma production using a standing helicon wave. *Physics Letters A*, 33(7):457–458, 1970.

[29] RW Boswell. Very efficient plasma generation by whistler waves near the lower hybrid frequency. *Plasma Physics and Controlled Fusion*, 26(10):1147, 1984.

[30] Trevor Alain Lafleur. *Helicon Wave Propagation in Low Diverging Magnetic Fields.* PhD thesis, 2011.

[31] P Aigrain. Les helicons dans les semiconducteurs. In *In Proceedings: International Conference on Semiconductor Physics*, page 224, 1960.

[32] Darryn A. Schneider. *Helicon Waves in High Density Plasmas.* PhD thesis, Australian National University, 1998.

[33] Charles Rudolf Legendy, C.ndy. Macroscopic theory of helicons. *Physical Review*, 135(6A):A1713, 1964.

[34] CR Legendy. Existence of proper modes of helicon oscillations. *Journal of Mathematical Physics*, 6(1):153–157, 1965.

[35] JP Klozenberg, B McNamara, and PC Thonemann. The dispersion and attenuation of helicon waves in a uniform cylindrical plasma. *Journal of Fluid Mechanics*, 21(03):545–563, 1965.

[36] HA Blevin and PJ Christiansen. Propagation of helicon waves in a non-uniform plasma. *Aust. J. Phys*, 19(501), 1966.

[37] HA Blevin, PJ Christiansen, and B Davies. Effect of electron cyclotron resonance on helicon waves. *Physics Letters A*, 28(3):230–231, 1968.

[38] HA Blevin and PJ Christiansen. Helicon waves in a non-uniform plasma. *Plasma Physics*, 10(8):799, 1968.

[39] JA Lehane and PC Thonemann. An experimental study of helicon wave propagation in a gaseous plasma. *Proceedings of the Physical Society*, 85(2):301, 1965.

[40] Francis F Chen. Plasma ionization by helicon waves. *Plasma Physics and Controlled Fusion*, 33(4):339, 1991.

[41] Francis F Chen, M Johannes Hsieh, and Max Light. Helicon waves in a non-uniform plasma. *Plasma Sources Science and Technology*, 3(1):49, 1994.

[42] AW Degeling, CO Jung, RW Boswell, and AR Ellingboe. Plasma production from helicon waves. *Physics of Plasmas (1994-present)*, 3(7):2788–2796, 1996.

[43] AR Ellingboe and RW Boswell. Capacitive, inductive and helicon-wave modes of operation of a helicon plasma source. *Physics of Plasmas (1994-present)*, 3(7): 2797–2804, 1996.

[44] Bin Tian, E Ahedo, and J Navarro-Cavalle. Investigation of plasma-wave interaction in helicon antenna thrusters. In *50th AIAA/ASME/SAE/ASEE Joint Propulsion Conference & Exhibit*, page 3475, 2014.

[45] Rod W Boswell and Francis F Chen. Helicons-the early years. *Plasma Science, IEEE Transactions on*, 25(6):1229–1244, 1997.

[46] Francis F Chen. Experiments on helicon plasma sources. *Journal of Vacuum Science & Technology A*, 10(4):1389–1401, 1992.

[47] Taihyeop Lho, Noah Hershkowitz, J Miller, W Steer, and Gon-Ho Kim. Azimuthally symmetric pseudosurface and helicon wave propagation in an inductively coupled plasma at low magnetic field. *Physics of Plasmas*, 5(9):3135–3142, 1998.

[48] C Carter and J Khachan. Downstream plasma characteristics from a single loop antenna in a helicon processing reactor. *Plasma Sources Science and Technology*, 8(3):432, 1999.

[49] Suwon Cho. The resistance peak of helicon plasmas at low magnetic fields. *Physics of Plasmas (1994-present)*, 13(3):033504, 2006.

[50] G Sato, W Oohara, and R Hatakeyama. Experimental characterization of a density peak at low magnetic fields in a helicon plasma source. *Plasma Sources Science and Technology*, 16(4):734, 2007.

[51] T Lafleur, C Charles, and RW Boswell. Characterization of a helicon plasma source in low diverging magnetic fields. *Journal of Physics D: Applied Physics*, 44 (5):055202, 2011.

[52] Seok-Min Yun, Jung-Hyung Kim, and Hong-Young Chang. Frequency dependence of helicon wave plasmas near lower hybrid resonance frequency. *Journal of Vacuum Science & Technology A*, 15(3):673–677, 1997.

[53] Suwon Cho. The role of the lower hybrid resonance in helicon plasmas. *Physics of Plasmas (1994-present)*, 7(1):417–423, 2000.

[54] JG Kwak, SK Kim, and Suwon Cho. Upper limit to the monotonic increasing dependence of the plasma density on the magnetic field in helicon discharges. *Physics Letters A*, 267(5):384–388, 2000.

[55] KP Shamrai and VB Taranov. Resonance wave discharge and collisional energy absorption in helicon plasma source. *Plasma Physics and Controlled Fusion*, 36 (11):1719, 1994.

[56] Donald Arnush. The role of trivelpiece–gould waves in antenna coupling to helicon waves. *Physics of Plasmas (1994-present)*, 7(7):3042–3050, 2000.

[57] Suwon Cho. Propagation and absorption of electromagnetic waves in inhomogeneous helicon plasmas with a lower hybrid resonance layer. *Journal of the Korean Physical Society*, 58(3):461–466, 2011.

[58] GG Borg and RW Boswell. Power coupling to helicon and trivelpiece–gould modes in helicon sources. *Physics of Plasmas (1994-present)*, 5(3):564–571, 1998.

[59] Suwon Cho. The field and power absorption profiles in helicon plasma resonators. *Physics of Plasmas (1994-present)*, 3(11):4268–4275, 1996.

[60] RW Boswell. Dependence of helicon wave radial structure on electron inertia. *Australian Journal of Physics*, 25(4):403–408, 1972.

[61] Francis F Chen and Schweickhard E Von Goeler. *Introduction to plasma physics and controlled fusion volume 1: Plasma physics*, volume 38. 1985.

[62] Konstantin P Shamrai and Vladimir B Taranov. Volume and surface rf power absorption in a helicon plasma source. *Plasma Sources Science and Technology*, 5 (3):474, 1996.

[63] Francis F Chen and Donald Arnush. Generalized theory of helicon waves. i. normal modes. *Physics of Plasmas (1994-present)*, 4(9):3411–3421, 1997.

[64] KP Shamrai and VB Taranov. Resonances and anti-resonances of a plasma column in a helicon plasma source. *Physics Letters A*, 204(2):139–145, 1995.

[65] Konstantin P Shamrai. Stable modes and abrupt density jumps in a helicon plasma source. *Plasma Sources Science and Technology*, 7(4):499, 1998.

[66] KP Shamrai, VP Pavlenko, and VB Taranov. Excitation, conversion and damping of waves in a helicon plasma source driven by an m= 0 antenna. *Plasma physics and controlled fusion*, 39(3):505, 1997.

[67] DD Blackwell, TG Madziwa, D Arnush, and FF Chen. Evidence for trivelpiece-gould modes in a helicon discharge. *Physical review letters*, 88(14):145002, 2002.

[68] Shunjiro Shinohara and Konstantin P Shamrai. Effect of electrostatic waves on a rf field penetration into highly collisional helicon plasmas. *Thin solid films*, 407 (1):215–220, 2002.

[69] Isaac D Sudit and Francis F Chen. A non-singular helicon wave equation for a non-uniform plasma. *Plasma Sources Science and Technology*, 3(4):602, 1994.

[70] Donald Arnush and Francis F Chen. Generalized theory of helicon waves. ii. excitation and absorption. *Physics of Plasmas (1994-present)*, 5(5):1239–1254, 1998.

[71] Suwon Cho and Jong-Gu Kwak. The effects of the density profile on the power absorption and the equilibrium density in helicon plasmas. *Physics of Plasmas (1994-present)*, 4(11):4167–4172, 1997.

[72] M Krämer. Propagation and damping of m=+ 1 and m=- 1 helicon modes in an inhomogeneous plasma column. *Physics of Plasmas*, 6(4):1052–1058, 1999.

[73] Boris N Breizman and Alexey V Arefiev. Radially localized helicon modes in nonuniform plasma. *Physical review letters*, 84(17):3863, 2000.

[74] Guangye Chen, Alexey V Arefiev, Roger D Bengtson, Boris N Breizman, Charles A Lee, and Laxminarayan L Raja. Resonant power absorption in helicon plasma sources. *Physics of Plasmas (1994-present)*, 13(12):123507, 2006.

[75] Charles A Lee, Guangye Chen, Alexey V Arefiev, Roger D Bengtson, and Boris N Breizman. Measurements and modeling of radio frequency field structures in a helicon plasma. *Physics of Plasmas (1994-present)*, 18(1):013501, 2011.

[76] L Chang, MJ Hole, JF Caneses, G Chen, BD Blackwell, and CS Corr. Wave modeling in a cylindrical non-uniform helicon discharge. *Physics of Plasmas (1994-present)*, 19(8):083511, 2012.

[77] Nicholas A Krall and Paulett C Liewer. Low-frequency instabilities in magnetic pulses. *Physical Review A*, 4(5):2094, 1971.

[78] JD Huba and CS Wu. Effects of a magnetic field gradient on the lower hydrid drift instability. *The Physics of Fluids*, 19(7):988–994, 1976.

[79] Cecilia Norgren. Lower hybrid drift wave properties in space plasma. mathesis, 2011.

[80] Peiyuan Zhu and RW Boswell. Ar i i laser generated by landau damping of whistler waves at the lower hybrid frequency. *Physical review letters*, 63(26):2805, 1989.

[81] Suwon Cho and DG Swanson. Dispersion relations for the lower hybrid frequency range. *The Physics of fluids*, 31(5):1123–1129, 1988.

[82] Matthew M Balkey, Robert Boivin, John L Kline, and Earl E Scime. Ion heating and density production in helicon sources near the lower hybrid frequency. *Plasma Sources Science and Technology*, 10(2):284, 2001.

[83] Yoshitaka Mori, Hieki Nakashima, Frederick W Baity, Richard H Goulding, Mark D Carter, and Dennis O Sparks. High density hydrogen helicon plasma in a non-uniform magnetic field. *Plasma Sources Science and Technology*, 13(3): 424, 2004.

[84] Seok-Min Yun and Hong-Young Chang. Radial density profile change near lower hybrid frequency in m= 0 helicon wave plasmas. *Physics Letters A*, 248(5):400–404, 1998.

[85] Peiyuan Zhu and RW Boswell. Observation of nonthermal electron tails in an rf excited argon magnetoplasma. *Physics of Fluids B: Plasma Physics*, 3(4):869–874, 1991.

[86] PK Loewenhardt, BD Blackwell, RW Boswell, GD Conway, and SM Hamberger. Plasma production in a toroidal heliac by helicon waves. *Physical review letters*, 67(20):2792, 1991.

[87] AR Ellingboe, RW Boswell, JP Booth, and N Sadeghi. Electron beam pulses produced by helicon-wave excitation. *Physics of Plasmas*, 2(6):1807–1809, 1995.

[88] Francis F Chen and David D Blackwell. Upper limit to landau damping in helicon discharges. *Physical review letters*, 82(13):2677, 1999.

[89] IV Kamenski and GG Borg. An evaluation of different antenna designs for helicon wave excitation in a cylindrical plasma source. *Physics of Plasmas (1994-present)*, 3(12):4396–4409, 1996.

[90] Max Light and Francis F Chen. Helicon wave excitation with helical antennas. *Physics of Plasmas (1994-present)*, 2(4):1084–1093, 1995.

[91] T Shoji, Y Sakawa, S Nakazawa, K Kadota, and T Sato. Plasma production by helicon waves. *Plasma Sources Science and Technology*, 2(1):5, 1993.

[92] Y Sakawa, N Koshikawa, and T Shoji. A higher-order radial mode of helicon waves. *Plasma Sources Science and Technology*, 6(1):96, 1997.

[93] Shunjiro Shinohara and Kenji Yonekura. Discharge modes and wave structures using loop antennae in a helicon plasma source. *Plasma physics and controlled fusion*, 42(1):41, 2000.

[94] Yiannis Mouzouris and John E Scharer. Modeling of profile effects for inductive helicon plasma sources. *Plasma Science, IEEE Transactions on*, 24(1):152–160, 1996.

[95] T Watari, T Hatori, R Kumazawa, S Hidekuma, T Aoki, T Kawamoto, M Inutake, S Hiroe, A Nishizawa, K Adati, et al. Radio-frequency plugging of a high density plasma. *The Physics of Fluids*, 21(11):2076–2081, 1978.

[96] A Komori, T Shoji, K Miyamoto, J Kawai, and Y Kawai. Helicon waves and efficient plasma production. *Physics of Fluids B: Plasma Physics*, 3(4):893–898, 1991.

[97] Isaac D Sudit and Francis F Chen. Discharge equilibrium of a helicon plasma. *Plasma Sources Science and Technology*, 5(1):43, 1996.

[98] M Krämer, B Lorenz, and B Clarenbach. Helicon sources with m= 1 and m= 2 helical antenna coupling. *Plasma Sources Science and Technology*, 11(3A):A120, 2002.

[99] L Porte, SM Yun, D Arnush, and FF Chen. Superiority of half-wavelength helicon antennae. *Plasma Sources Science and Technology*, 12(2):287, 2003.

[100] BH Park, NS Yoon, and Duk-In Choi. Calculation of reactor impedance for helicon discharge. *Plasma Science, IEEE Transactions on*, 29(3):502–511, 2001.

[101] D Melazzi, V Lancellotti, P De Carlo, Marco Manente, and Daniele Pavarin. Optimization of antenna-plasma interaction in a helicon plasma thruster. In *Antennas and Propagation (EuCAP), 2014 8th European Conference on*, pages 1321–1324. IEEE, 2014.

[102] Michael A Lieberman and Alan J Lichtenberg. *Principles of plasma discharges and materials processing*. John Wiley & Sons, 2005.

[103] IV Kamenski and GG Borg. A 1d cylindrical kinetic wave code for helicon plasma sources. *Computer physics communications*, 113(1):10–32, 1998.

[104] B Fischer, M Kramer, and Th Enk. Helicon wave coupling to a finite plasma column. *Plasma physics and controlled fusion*, 36(12):2003, 1994.

[105] Suwon Cho and MA Lieberman. Self-consistent discharge characteristics of collisional helicon plasmas. *Physics of Plasmas (1994-present)*, 10(3):882–890, 2003.

[106] B.D. McVey. Icrf antenna coupling theory for a cylindrical stratified plasma. Technical report, Plasma Fusion Center, MIT, 1984.

[107] D Melazzi, D Curreli, M Manente, J Carlsson, and D Pavarin. Spires: A finite-difference frequency-domain electromagnetic solver for inhomogeneous magnetized plasma cylinders. *Computer Physics Communications*, 183(6):1182–1191, 2012.

[108] Bin Tian, E Ahedo, and J Navarro-Cavalle. Analysis of plasma impedance in helicon antenna thrusters. In *In 34th International Electric Propulsion Conference*, number IEPC-2015-326. Electric Rocket Propulsion Society, 2015.

[109] D Melazzi and Vito Lancellotti. Adamant: A surface and volume integral-equation solver for the analysis and design of helicon plasma sources. *Computer Physics Communications*, 185(7):1914–1925, 2014.

[110] Seiji Takechi and Shunjiro Shinohara. Rf wave propagation in bounded plasma under divergent and convergent magnetic field configurations. *Japanese journal of applied physics*, 38(11A):L1278, 1999.

[111] Yiannis Mouzouris and John E Scharer. Wave propagation and absorption simulations for helicon sources. *Physics of Plasmas (1994-present)*, 5(12):4253–4261, 1998.

[112] Ronald L Kinder and Mark J Kushner. Noncollisional heating and electron energy distributions in magnetically enhanced inductively coupled and helicon plasma sources. *Journal of Applied Physics*, 90(8):3699–3712, 2001.

[113] Ronald L Kinder, AR Ellingboe, and Mark J Kushner. H-to w-mode transitions and properties of a multimode helicon plasma reactor. *Plasma Sources Science and Technology*, 13(1):187, 2004.

[114] Ronald L Kinder and Mark J Kushner. Wave propagation and power deposition in magnetically enhanced inductively coupled and helicon plasma sources. *Journal of Vacuum Science & Technology A: Vacuum, Surfaces, and Films*, 19(1):76–86, 2001.

[115] Deepak Bose, TR Govindan, and M Meyyappan. Modelling of magnetic field profile effects in a helicon source. *Plasma Sources Science and Technology*, 13(4): 553, 2004.

[116] Kane S Yee et al. Numerical solution of initial boundary value problems involving maxwells equations in isotropic media. *IEEE Trans. Antennas Propag*, 14(3): 302–307, 1966.

[117] Peiyuan Zhu and RW Boswell. A new argon-ion laser based on an electrodeless plasma. *Journal of applied Physics*, 68(5):1981–1984, 1990.

[118] Magpie helionc source. https://physics.anu.edu.au/prl/projects/project.php?ProjectID=225.

[119] Gaétan Chevalier and Francis F Chen. Experimental modeling of inductive discharges. *Journal of Vacuum Science & Technology A: Vacuum, Surfaces, and Films*, 11(4):1165–1171, 1993.

[120] David D Blackwell and Francis F Chen. Two-dimensional imaging of a helicon discharge. *Plasma Sources Science and Technology*, 6(4):569, 1997.

[121] Xin M Guo, J Scharer, Yiannis Mouzouris, and L Louis. Helicon experiments and simulations in nonuniform magnetic field configurations. *Physics of Plasmas (1994-present)*, 6(8):3400–3407, 1999.

[122] Martin I Panevsky and Roger D Bengtson. Characterization of the resonant electromagnetic mode in helicon discharges. *Physics of plasmas*, 11(9):4196–4205, 2004.

[123] He-l helionc source. http://www.ruhr-uni-bochum.de/ep2/english/research/topics-helicon2.htm.

[124] M Krämer, Yu M Aliev, AB Altukhov, AD Gurchenko, EZ Gusakov, and K Niemi. Anomalous helicon wave absorption and parametric excitation of electrostatic fluctuations in a helicon-produced plasma. *Plasma Physics and Controlled Fusion*, 49 (5A):A167, 2007.

[125] Christian M Franck, Olaf Grulke, Albrecht Stark, Thomas Klinger, Earl E Scime, and Gérard Bonhomme. Measurements of spatial structures of different discharge modes in a helicon source. *Plasma Sources Science and Technology*, 14(2):226, 2005.

[126] Vineta helionc source. http://www.ipp.mpg.de/1059101/vineta.

[127] S Shinohara, T Motomura, K Tanaka, T Tanikawa, and KP Shamrai. Large-area high-density helicon plasma sources. *Plasma Sources Science and Technology*, 19 (3):034018, 2010.

[128] Shunjiro Shinohara and Takao Tanikawa. Development of very large helicon plasma source. *Review of scientific instruments*, 75(6):1941–1946, 2004.

[129] Donald Gary Swanson. *Plasma waves*. Elsevier, 2012.

[130] Thomas H Stix. *Waves in plasmas*. Springer Science & Business Media, 1992.

[131] Marco Brambilla. *Kinetic theory of plasma waves: homogeneous plasmas*. Number 96. Oxford University Press, 1998.

[132] Eduardo Ahedo. Magnetic confinement of a high-density cylindrical plasma. *Physics of Plasmas (1994-present)*, 18(10):103506, 2011.

[133] Navarro Cavalle Jaume. Helicon plasma thrusters: prototypes and advances on modeling. In *The 33rd International Electric Propulsion Conference*, number IEPC-2013-285, Washington D.C., USA, 2013.

[134] Sophocles J Orfanidis. *Electromagnetic waves and antennas*. Rutgers University New Brunswick, NJ, 2002.

[135] D Martinez and E Ahedo. Plasma-wave interaction in a helicon thruster. In *In 32th International Electric Propulsion Conference*, number IEPC-2011-047. Electric Rocket Propulsion Society, 2011.

[136] John David Jackson. *Classical Electrodynamics*. Wiley, 1999.

[137] Hans J Weber and George B Arfken. *Essential Mathematical Methods for Physicists, ISE*. Academic Press, 2003.

[138] Eduardo Ahedo and Mario Merino. Two-dimensional plasma expansion in a magnetic nozzle: Separation due to electron inertia. *Physics of Plasmas*, 19(8):083501, 2012.